

ADAM MICKIEWICZ UNIVERSITY POZNAŃ
FACULTY OF PHYSICS
ASTRONOMICAL OBSERVATORY INSTITUTE

author:
Aleksandra Leśniewska

The Interstellar Medium.
What it can tell us about stars that form it
and evolve within it.

PhD thesis based on original publications

Supervisor:
DR HAB. MICHAŁ JERZY MICHAŁOWSKI
Auxiliary Supervisor:
DR JAKUB NADOLNY



Poznań, 2024

Acknowledgements

I owe my deepest gratitude to my supervisor, Michał Michałowski, who became my guide through the Universe. Over the years of collaboration, he consistently exemplified the qualities of an outstanding scientist, a kind person, and a commendable mentor. I extend sincere appreciation to Jakub Nadolny for accompanying me on this journey. His indispensable contributions and insightful perspective enriched our discussions significantly. I could not have asked for better supervisors.

Thanks to my DARK colleagues who provided me with my dream work environment. All those I collaborated with helped me recognize that despite varying opinions, we collectively pursue a shared goal.

During my journey, I was accompanied by a Portuguese girl whom I met unexpectedly. Sandra, you stood by me through my highs and lows. I am deeply indebted to you for bringing much joy into my life.

To my parents for always being there for me.

I received my first financial support from Adam Mickiewicz University in Poznań, Faculty of Physics, through grant POWR.03.01.00-00-S157/17 (funding from The National Centre for Research and Development), just before the official start of my PhD studies. Part of this thesis was performed with financial support from The National Science Centre (NCN) through the PRELUDIUM grant (2021/41/N/ST9/02662) and the SONATA BIS grant (2018/30/E/ST9/00208). The Leon Rosenfeld Foundation (Denmark) and Adam Mickiewicz University in Poznań (Poland, via program Uniwersytet Jutra II, POWR.03.05.00-00-Z303/18) funded my research visits to the Dark Cosmology Centre in Copenhagen. I have also received support from a VILLUM FONDEN Investigator grant (Denmark, project number 16599 and VIL54489).

Streszczenie

Cała otaczająca nas dzisiaj materia jest produktem ewolucji Wszechświata. Cele niniejszej pracy skupiają się nad zbadaniem procesów odpowiedzialnych za produkcję pyłu we wczesnym Wszechświecie, identyfikacją dominujących mechanizmów prowadzących do usuwania materii z ośrodka międzygwiazdowego z galaktyk wczesnego typu, oraz zbadaniem środowiska w którym doszło do długiego rozbłysku gamma, któremu nie towarzyszyła eksplozja supernowej.

Jednym z zagadnień, które jest wciąż przedmiotem analizy, jest produkcja pyłu we wczesnym Wszechświecie. Zrozumienie tego zjawiska pomaga w scharakteryzowaniu warunków środowiskowych tamtej epoki i ma znaczenie przy porównywaniu ich z lokalnym Wszechświatem. Produkcję pyłu we wczesnym Wszechświecie opisuje się poprzez badanie galaktyk, w których wykryto emisję pyłu. Moja analiza galaktyk z detekcją pyłu ukazuje, że gwiazdy asymptotycznej gałęzi olbrzymów nie są wystarczająco skuteczne w wytwarzaniu pyłu. Z kolei supernowe wydają się bardziej obiecujące, zakładając ich maksymalną wydajność i braku zniszczenia pyłu. Wyniki analizy sugerują, że za wytwarzanie pyłu odpowiedzialny jest głównie niegwiazdowy mechanizm, prawdopodobnie wzrost ziaren pyłu w ośrodku międzygwiazdowym.

Zrozumienie procesu, w wyniku którego galaktyki wstrzymują produkcję nowych gwiazd i usuwają ośrodek międzygwiazdowy, pozostaje zagadką. Badanie próbki kilku tysięcy zapylnych galaktyk eliptycznych może rzucić światło na te mechanizmy. Badając korelację pomiędzy parametrami fizycznymi tych galaktyk wyznaczyłam skalę czasową usuwania pyłu. Bliskość innych galaktyk nie wpływa na usuwanie pyłu, ponieważ interakcje są mało prawdopodobne ze względu na odległości między galaktykami. Również masa galaktyki, ani jej przesunięcie ku czerwieni nie wpływają na szybkość tego procesu. Warto zauważyć, że istnieje odejście od oczekiwanej relacji tempa powstawania gwiazd i masy pyłu, co prawdopodobnie jest wynikiem wygaszenia morfologicznego produkcji nowych gwiazd. To wygaszanie, w połączeniu z jonizacją lub wpływami wywołanymi przez starsze populacje gwiazd, jest w zgodzie z danymi obserwacyjnymi i może przyczyniać się do utraty pyłu z tych zapylnych galaktyk eliptycznych.

Długie błyski gamma, jedne z najbardziej energetycznych eksplozji we Wszechświecie, są zwykle powiązane z eksplozjami masywnych gwiazd, chociaż w trzech przypadkach emisja supernowych pozostała niewykryta pomimo szeroko zakrojonych obserwacji. Aby uzyskać wgląd w te zagadkowe zdarzenia, wykorzystałam nowe dane linii H α i archiwalne optyczne dane spektroskopowe do zbadania ośrodka międzygwiazdowego galaktyki macierzystej jednego z takich zdarzeń, GRB 111005A. Moja analiza ukazała w ogólności gładki rozkład gazu atomowego, kontinuum radiowe i prędkości rotacji w całej galaktyce, co wskazuje na brak niedawnych wpływów i wypływów gazu. Ponadto w pobliżu GRB 111005A nie było zauważalnej koncentracji gazu. Obserwacje te sugerują, że ośrodek międzygwiazdowy w tej konkretnej galaktyce różni się od ośrodka obserwowanego w galaktykach macierzystych innych długich rozbłysków gamma. Wskazuje to, że rozbłysk mógł nie być wynikiem eksplozji bardzo masywnej gwiazdy, ale raczej połączenia zwartych obiektów.

Abstract

All the matter surrounding us today is a product of the Universe's evolution. The objectives of this thesis are to investigate the processes responsible for dust production in the early Universe, to identify the predominant mechanisms driving the removal of the interstellar medium from early-type galaxies, and to explore the environment of the supernova-less long gamma-ray burst host galaxy.

One issue that is still under analysis is the production of dust in the early Universe. Understanding this phenomenon aids in characterising the environmental conditions of that epoch and holds relevance for comparing them with the local Universe. Dust production in the early Universe is elucidated by studying galaxies in which dust emissions have been detected. My analysis of these galaxies reveals that asymptotic giant branch stars are not sufficiently effective in producing dust. Supernovae, on the other hand, appear more promising, though under the assumption of their maximal efficiency, assuming no dust destruction. The collective findings suggest that a non-stellar mechanism is predominantly responsible for dust production, likely involving grain growth in the interstellar medium.

Understanding the process by which galaxies cease star formation and remove their interstellar medium remains a puzzle. Investigating a broad sample of dusty elliptical galaxies holds promise for shedding light on these mechanisms. I examined the correlation between the physical characteristic parameters of these galaxies, leading to the determination of the dust removal timescale. Proximity to other galaxies does not impact dust removal, as interactions are improbable due to the distance between galaxies. Neither the galaxy's mass nor its redshift affects the rate of this process. Notably, there is a departure from the expected star formation rate vs. dust mass relation, likely a result of a morphological quenching. This quenching, coupled with ionisation or outflows triggered by older stellar populations, aligns well with observational data and may contribute to dust loss from these dusty elliptical galaxies.

One of the most energetic events in the Universe, long gamma-ray bursts are typically linked to the explosions of massive stars, although in three instances, supernova emission has remained undetected despite extensive observations. To gain insights into these enigmatic events, new HI line data, and archival optical integral field spectroscopy were utilised to examine the interstellar medium of the host galaxy of one such event, GRB 111005A. My analysis revealed a generally smooth distribution of atomic gas, radio continuum, and rotational patterns across the galaxy, indicating the absence of recent gas inflows or outflows. Additionally, there was no discernible concentration of gas around the location of the GRB. These observations suggest that the interstellar medium in this particular galaxy differs from that observed in hosts of other long gamma-ray bursts. This indicates that the progenitor of GRB 111005A may not have been the result of the explosion of a very massive star but rather a compact object merger.

Publications

Chapters 2, 3, 4 have been published as:

- **Aleksandra Leśniewska**, Michał Jerzy Michałowski.

Dust production scenarios in galaxies at $z \sim 6-8.3$, 2019, *A&A*, 624, L13.

IF (2019) = 5.636, MEiN points = 140.

- **Aleksandra Leśniewska**, Michał Jerzy Michałowski, Christa Gall, Jens Hjorth, Jakub Nadolny, Oleh Ryzhov, Martin Solar.

The Fate of the Interstellar Medium in Early-type Galaxies. II. Observational Evidence for Morphological Quenching, 2023, *ApJ*, 953, 27.

IF (2021) = 5.521, MEiN points = 140.

- **Aleksandra Leśniewska**, Michałowski, M. J., Kamphuis, P., Dziadura, K., Baes, M., Castro Cerón, J. M., Gentile, G., Hjorth, J., Hunt, L. K., Jespersen, C. K., Koprowski, M. P., Le Floch, E., Miraghaei, H., Nicuesa Guelbenzu, A., Oszkiewicz, D., Palazzi, E., Polińska, M., Rasmussen, J., Schady, P., Watson, D.

The interstellar medium in the environment of the supernova-less long-duration GRB 111005A, 2022, *ApJS*, 259, 67.

IF (2021) = 9.200, MEiN points = 200.

List of Figures

1.1	The lifecycle of the ISM	1
1.2	Dust particle	3
1.3	Dusty SED	7
1.4	Sérsic index relation with stellar mass and galaxy's colour	14
1.5	Dust mass vs. SFR in star-forming galaxies	16
1.6	Dust-to-stellar mass ratio as a function of luminosity-weighted stellar age of Herschel-detected ETGs	17
1.7	Types of gamma-ray bursts	20
1.8	Gamma-ray burst	22
2.1	Dust yield per star	32
3.1	Main sequence galaxies vs. below-MS galaxies	41
3.2	Dust-to-stellar mass vs. stellar age	42
3.3	Medians	43
4.1	The GRB 111005A host HI maps	53
4.2	Profiles of the HI atomic gas	54
4.3	GMRT interferometric spectrum	55
4.4	Rotation curves from the tilted ring modeling	55
4.5	1.4 GHz continuum emission of the GRB 111005A host	57
4.6	1.4 GHz continuum emission profiles of the GRB 111005A host	58
4.7	Atomic gas emission of the GRB 111005A host from GMRT overlaid on maps of physical properties derived from MUSE observations	59
4.8	Profiles of properties derived using the MUSE data as a function of the distance from the galaxy centre	68
4.9	Color-scale images of the GRB 111005A host	73
4.10	Positions of regions analysed in CO	74

List of Tables

2.1	List of physical properties of dusty high redshift galaxies	30
3.1	Dust removal timescale	46
3.2	Selected physical properties of ETGs	47
4.1	Properties of regions in the GRB 111005A host	56
4.2	Properties of two parts in the GRB 111005A host	69
4.3	Properties of the host galaxy of GRB 111005A determined from HI cubes	70

Contents

1	Introduction	1
1.1	Cosmic dust	2
1.1.1	Dust detection and dust mass	4
1.1.2	Stellar and non-stellar dust sources	7
1.1.3	Dust removal mechanisms	11
1.1.4	Early-type galaxies	13
1.2	Cosmic gas and its atomic, molecular, and ionised state	16
1.2.1	Gas detection and gas mass calculation	18
1.3	Gamma-ray bursts	19
1.3.1	Long GRB environment	22
1.3.2	Long GRBs with no SN detection	24
1.4	The aims of this thesis	25
2	Dust production in the first billion years of the Universe	26
2.1	Introduction	26
2.2	Sample	27
2.3	Method	29
2.4	Results and discussion	31
2.5	Conclusions	34
2.6	PhD candidate contribution	34
3	Observational evidence for morphological quenching in early-type galaxies	35
3.1	Introduction	35
3.2	Data and Sample	37
3.2.1	GAMA Catalog	37
3.2.2	Sample	37
3.3	Results	38
3.3.1	Main Sequence	38
3.3.2	Dust Removal Timescale	38
3.3.3	Dust Masses vs Star Formation Rates	39
3.3.4	Central Surface Luminosity	40
3.3.5	Quenching	40
3.3.6	Sample Evaluation	40
3.4	Discussion	44
3.5	Conclusions	45
3.6	PhD candidate contribution	45

4	A long-duration GRB and its uncommon environment	48
4.1	Introduction	49
4.2	GRB 111005A and its host	50
4.3	Data	51
	4.3.1 GMRT observations	51
	4.3.2 MUSE data	52
4.4	Tilted ring modelling	52
4.5	Results	58
	4.5.1 Residual scaling correction	60
	4.5.2 Atomic and molecular gas	60
	4.5.3 Kinematic modelling	62
	4.5.4 Radio continuum	62
	4.5.5 Stars, ionised gas and dust	63
	4.5.6 Large-scale environment	64
4.6	Discussion	64
4.7	Conclusions	67
4.8	PhD candidate contribution	71
5	Summary and conclusion	75
5.1	Dust production scenarios in galaxies at $z \sim 6-8.3$	75
5.2	The fate of the interstellar medium in early-type galaxies. II. Observational evidence for morphological quenching	76
5.3	The interstellar medium in the environment of the supernova-less long-duration GRB 111005A	77
	Bibliography	81
	Co-author statements	97

Chapter 1

Introduction

Every star, planet, and asteroid was created from matter accumulating in dusty gas clouds. All gaseous and dusty matter, as well as cosmic rays and magnetic fields, are part of the so-called interstellar medium (ISM), which constitutes an important component of all galaxies. The Universe constantly recycles this material due to stellar evolution. Figure 1.1 presents the lifecycle of matter in galaxies.

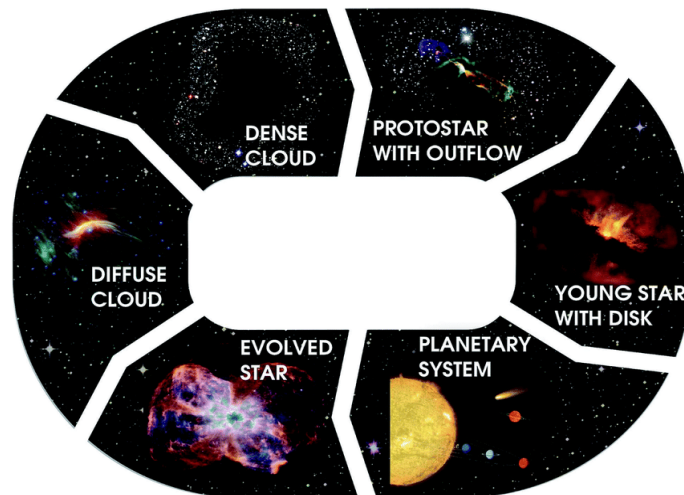


Figure 1.1: The lifecycle of gas, dust, and ice in interstellar and circumstellar clouds. Credit: M. Persson, NASA/ESA/ESO/ALMA.

Diffuse clouds are characterised by a density of about 10^3 atoms/cm³ and temperatures ≤ 100 K. Inside such diffuse clouds, dense molecular clouds are found, which have higher density and lower temperature. Eventually, the dense molecular cores of clouds collapse due to gravity and form protostars. From the leftover gas and dust, planetary systems come into existence. At this stage, the protostar transitions into a main sequence star and reaches core temperatures that are sufficiently high to initiate the process of hydrogen fusion into helium. Throughout its lifetime, a star releases some of its primary and newly produced material to the environment around it. The last stages of a star's life can be the most violent and spectacular. Depending on the initial mass of the star, there may be strong ejections of matter, stellar winds, and explosions. The interstellar space is then enriched with new components created during such events. In

this way, a new enriched dust and gaseous cloud can form another population of stars and planetary systems.

1.1 Cosmic dust

The issue of dust origin and evolution is one of the most important regarding extragalactic astrophysics. Dust is a key component of the interstellar medium even though it comprises only 1% of the total baryonic mass in the Universe. It is a solid-state component composed of micron-sized grain particles (see Fig.1.2), mostly made of carbon (C) and silicates (Mg/Fe-based) (Mathis et al. 1977). Its surface provides favourable conditions for the formation of molecules, for example, molecular hydrogen (H_2), which is the most abundant molecule in the Universe (Gould & Salpeter 1963; Cazaux & Tielens 2002; Wakelam et al. 2017). Some atoms would rarely interact and form molecules if not at the dust grain surface. Thus, the existence of dust particles contributes to the increase of the molecular formation process. The rate of molecular formation is two orders of magnitude higher in the presence of dust particles than without them (Hollenbach & McKee 1979). Apart from the silicate/carbon core and the grain surface, there is also a mantle made of ices, e.g. CO_2 , H_2O , CH_4 . Refractory elements such as Mg, Fe, Al, Ti, and Ca precipitate onto the grains from the gas phase (Micelotta et al. 2018). More complex carbonous particles in which we observe a honeycomb configuration of C atoms arranged in aromatic rings are called polycyclic aromatic hydrocarbons (PAHs, Leger & Puget (1984a); Allamandola et al. (1985)). These dust grains, made of dozens of C atoms, with a size of a few nanometers, are uncharged and non-polar, and all of the atoms lie in the same plane. The presence of dust also contributes to the cooling of the ISM, which may lead to the star formation process (e.g. Omukai et al. 2005).

Although the mass of dust grains is relatively low, it can absorb up to 30% of the ultraviolet to infrared (UV, IR) light (Hauser & Dwek 2001), and then re-radiates this absorbed light in the far infrared (FIR) part of the spectrum. Some objects are indeed heavily obscured by the dust in the optical wavelengths. Absorption and scattering on dust grains are evident in the UV to IR range as extinction/attenuation of starlight. Dust can scatter the light coming from a star, changing the direction in which the photon moves. By analysing extinction we are unable to say anything about the temperature of the dust particles. An absorbed photon is re-emitted by the dust particle, but at a longer wavelength than the original one. Both absorption and scattering mechanisms provide a way to estimate the dust grain sizes since a different size will subject photons to different changes. Due to their irregularity, elongated dust grains can align with the magnetic field; their spin axes follow the field lines, and photon absorption takes place on the longer axis. As a result of this mechanism scattered light becomes polarized (Hall 1949; Hiltner 1949a,b).

The distribution of sizes of dust grains is described by a power-law and can be inferred from an observed extinction curve (Mathis et al. 1977). The size of dust grains is influenced by the chemical composition of the particles that make up the grain. For example, the size of graphite dust grains can vary between 0.005 up to $1\mu m$ (Mathis

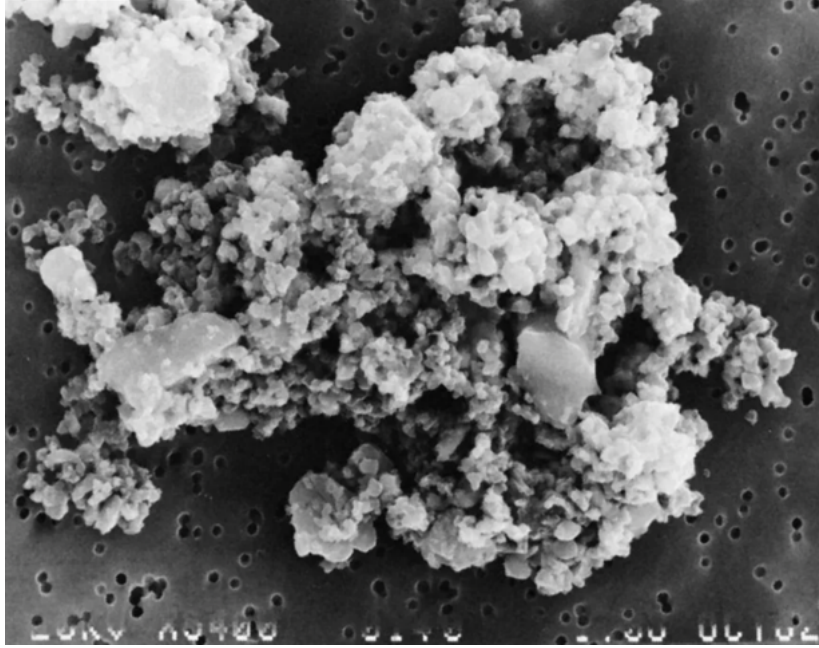


Figure 1.2: A microscope image of an interplanetary dust particle. Credit: Courtesy of D. Brownlee, University of Washington; photograph, M. Wheelock.

et al. 1977). This distribution implies size-dependent absorption or scattering seen at different wavelengths.

Dust serves as a temperature regulator within the ISM. Considering temperature regulation by dust grains, we can divide this ISM component into two groups. The first group is the ISM comprised of large grains with radii $\gtrsim 0.03\mu\text{m}$ that are in thermal equilibrium with the radiation field. The total energy of these grains does not change noticeably due to photon absorption or emission. When the power radiated by the dust grain equals the heating rate a steady-state temperature is observed (Draine 2011). The second group contains smaller dust grains which are much more susceptible to temperature fluctuations. One photon can cause a temperature jump of several hundred Kelvins when the energy input from a discrete heating event equals or surpasses the average heat content of the grain (Draine & Anderson 1985). Small grains are consequently not in thermal equilibrium. Dust facilitates the formation of molecules on its surface and shields them from the intense interstellar radiation field. The fundamental characteristics of dust grains, such as their size and composition, are intricately tied to the specific conditions of the environment in which they originate.

Today’s knowledge about the evolution of galaxies and the ISM is based not only on observations but also on simulations. Some models necessitate the incorporation of numerous parameters, and due to the unknown microphysics of grains, these parameters are frequently set to values that lack observational constraints. Consequently, the model output may simply mirror the input. Some cosmological simulations are based on simplified models of dust evolution, where for example constant dust yields are assumed regardless of a star formation episode (Baugh et al. 2005; Somerville et al. 2012; Croton et al. 2016). So-called “closed-box” models, presented by Dwek (1998); Zhukovska et al. (2008); Valiante et al. (2009); Asano et al. (2013) can describe the

formation and destruction of dust in more detail, but again, these models are not without imperfections, because they do not take outflows and inflows into consideration. In recent years, much more complex models have been developed. These often take into consideration more complicated dust evolution processes. There are two prevalent methods used to simulate galaxy formation: semi-analytical models (SAMs) and hydrodynamic simulations. Croton et al. (2016) presented a codebase designed for modelling galaxy formation within a cosmological framework called “Semi-Analytic Galaxy Evolution” (SAGE). This model includes e.g. gas cooling and active galactic nucleus heating of halo gas, ejected gas reincorporation. Subsequent SAGE updates included more mechanisms occurring during galaxy evolution. Triani et al. (2020) implemented mechanisms contributing to changes taking place within the ISM: dust condensation in the ejecta of SNe type II and AGB stars, grain growth in the dense molecular clouds, destruction by SN shocks, and dust removal from the ISM by star formation, reheating, inflows, and outflows. Recent SAM presented in Parente et al. (2022) tracks separately the abundances of large and small silicate grains, as well as large and small carbonaceous grains. For this purpose, a detailed description of dust evolution using two-size approximation by Hirashita (2015) has been included together with distinguishing between carbonaceous and silicate grains based on their chemical composition. This two-size approximation includes radius $a < 0.03 \mu\text{m}$ small grains and $a > 0.03 \mu\text{m}$ large grains. This model incorporates various processes such as dust supply from stellar ejecta, SN shock dust destruction, dust growth through accretion, grain growth via coagulation, and grain disruption by shattering. The results of their analysis demonstrated that this straightforward framework effectively replicates the primary characteristics observed in comprehensive calculations of grain size distributions. Hydrodynamic cosmological simulations have been developed recently implementing the dust production, destruction, and growth evolution in it (e.g. McKinnon et al. 2017; Aoyama et al. 2018).

Over the past few decades, many theoretical considerations have been carried out on dust evolution, formation, and destruction. Some of the first research dealing with this issue is Dwek & Scalo (1980). They analysed and modeled processes in the solar neighborhood. Hirashita (1999) described the dust-to-gas ratio of nearby star-forming galaxies with models of Lisenfeld & Ferrara (1998) and Dwek (1998). These models are based on four processes occurring in spiral galaxies: dust formation from heavy elements ejected by stellar mass loss, dust destruction in supernova remnants, dust destruction in star-forming regions, and accretion of heavy elements onto preexisting dust grains.

By observing the dust, we can also learn something about stars within the dusty cocoons. Ultraviolet and optical waves emitted by the stars are re-emitted at the infrared part of the spectrum by dust and this is why dust is often used as a tracer of star formation in galaxies (Kennicutt & Evans 2012).

1.1.1 Dust detection and dust mass

Photon absorption can heat dust grains, causing them to emit radiation, which allows for their direct detection. Dust grains absorb incoming radiation from the sur-

roundings, spanning from UV to IR, leading to the excitation of electrons. Afterward, the heated dust grains emit thermal radiation according to Planck’s law, which results in continuous emission across longer wavelengths. The degree to which dust grains emit thermal radiation in comparison to an idealized black-body radiator at a specific temperature is called dust emissivity. This parameter is strongly dependent on wavelength (Whittet 2003). The spectrum of emitted black-body from dust grains changes with temperature; cooler grains predominantly emit in the FIR, while warmer ones emit in the mid-infrared (MIR). Collisions with other grains, gas particles, electrons, or cosmic rays may also increase the dust grain temperature with kinetic energy transfer.

As described by Kennicutt & Evans (2012), emission in the 5-20 μm range contains molecular lines emitted by PAHs. A change in the vibrational mode in the molecule causes this emission. In the case of PAHs, when a hydrogen atom is added to the edge of the C-ring structure, this mechanism occurs. This means that emissions of specific wavelengths can be observed. Well-known PAH features are found at 3.3, 6.2, 7.7, 8.6, and 11.3 μm (Leger & Puget 1984b; Allamandola et al. 1985, 1999). These emission lines are observed in ionised regions of reflection nebulae. As presented by Peeters et al. (2004), PAHs can trace star formation activity, and in particular B stars. PAH excitation is only possible if the molecules are sufficiently small. Only then a single-photon absorption may cause a temperature increase up to 250 K (Draine 2011). Thermal continuum emission is visible above 20 μm due to the main dust grain population. The continuum and the PAH emission are caused by small dust grains, whereas the emission at a wavelength longer than 60 μm is dominated by large grains (Kennicutt & Evans 2012). The dust emission peak can shift from shorter (close to PAHs) to longer wavelengths as the dust grains become colder. The dust temperature ranges between a dozen and several hundred Kelvin and depends on the grain size, the strength and distance from a radiation source, and the Cosmic Microwave Background (CMB) at high- z ($T_{CMB} = T_0(1 + z)$ K), where $T_0 = 2.725$ K is the CMB temperature measured at the current epoch, Fixsen (2009).

There are a few powerful ground- and space-based instruments that allow us to investigate dust in the local and high redshift Universe. Interferometers such as the Atacama Large Millimeter/submillimeter Array (ALMA), Giant Metrewave Radio Telescope (GMRT), and Northern Extended Millimeter Array (NOEMA) are ideal instruments for conducting a comprehensive and accurate analysis of interstellar matter in individual galaxies. Submillimeter observations made with ALMA provide information about the cold and distant Universe and are perfect for detecting dusty galaxies in the early Universe. For these, the peak of the dust emission falls in the (sub-)millimetre wavelengths due to the redshift effect. Over the last several decades, IR space observatories have detected many dusty objects in the Universe. One of the pioneering telescopes was *Spitzer Space Telescope*, equipped with two detectors IRAC and MIPS which for about 16 years provided information about the infrared Universe. Observatories such as the *Herschel Space Observatory*, with its two instruments PACS and SPIRE, have been able to provide deep infrared observations of hundreds of square degrees. Its large field of view, $4' \times 8'$, and high sensitivity in a short time led to the detection of dust in millions of galaxies. With the newest instruments like *James Webb Space Telescope (JWST)*, we expect to see even more of the infrared Universe. An ex-

ample of a spectral energy distribution (SED) changing with a redshift is presented in Fig. 1.3. Additionally, some observational bands of *Spitzer*, *Herschel*, ALMA, *JWST* have been marked.

The expanding Universe shifts the observed spectrum of galaxies to longer wavelengths than those originally emitted. The observer then needs to deal with redshifted measurements. For galaxies in particular, it is worth mentioning the K -correction (Humason et al. 1956; Oke & Sandage 1968; Hogg et al. 2002; Blanton & Roweis 2007), a transformation between observed and rest-frame magnitudes or fluxes. Galaxies at a given redshift emit the light at a given wavelength (λ_e). However, the observer must take into account the fact of shifting this emission ($\lambda_o = \lambda_e (1+z)$) in their calculations due to redshift. To apply the K -correction, assumptions must be made about the shape of the true SED of the examined galaxy, e.g. assumptions about stellar population or dust attenuation contribution. Typically, corrections rely on fitting templates to observed SEDs which requires multi-colour photometry data. Optical and radio fluxes of galaxies decrease with increasing redshift due to increasing distance not compensated by probing brighter part of the SED (Blain et al. 2002), which is called a positive K -correction. As shown in Fig. 1.3 IRAC, *JWST*, or MIPS detectors cover wavelength ranges at which galaxies at different redshifts have significantly different fluxes. It should be emphasised that at submillimeter wavelengths, fluxes remain constant, or increase. This is a negative K -correction and means that the measured sub-mm fluxes are less affected by redshift, as shown in Fig. 1.3. At these wavelengths, SEDs of galaxies are dominated by the thermal dust emission with a peak at rest-frame wavelengths $\sim 100\mu\text{m}$. As a result, within this wavelength range, we are capable of detecting galaxies at high redshifts with comparable efficiency to those at low redshifts.

ALMA, renowned for its proficiency in detecting (sub-)millimeter emission, stands out as one of the most important instruments in this field. It plays a crucial role in pinpointing the dust continuum emission peaks of high-redshift galaxies, as illustrated in Fig. 1.3. Since its inauguration in 2011, ALMA has operated as a sophisticated interferometer, boasting a configuration of 66 antennas, which facilitates the investigation of galaxies with angular resolutions ranging from a few arcseconds to ~ 10 milli-arcseconds, depending on the antenna configuration. This corresponds to a physical scale of a couple of hundred parsecs for an unlensed galaxy at $z \sim 2$ (see Fig. 2 in Hodge & da Cunha 2020). Prior to the ALMA era, observations were constrained to the brightest high-redshift galaxies, star-forming, commonly referred to as "submillimeter galaxies" (e.g., Blain et al. 2002). Before ALMA's advent, single-dish telescopes provided insights into galactic matter on scales exceeding 100 kiloparsecs at redshifts around $z \sim 2$, corresponding to a resolution of approximately 15-30" (Hodge & da Cunha 2020). The redshift milestone for a normal galaxy was held by a UV-selected galaxy at $z \sim 3.21$, meticulously analyzed by Magdis et al. (2012). In their study to uncover the most redshifted galaxies detected by *Herschel*, Riechers et al. (2013) identified an exceedingly massive and vigorously star-forming galaxy, exhibiting a $\text{SFR} \geq 2,000 M_{\odot} \text{ yr}^{-1}$. Through the discernment of numerous spectral lines, encompassing both absorption and emission features, they derived a redshift of 6.34. ALMA observations have extended the redshift frontier for typical star-forming galaxies.

The formula below (Taylor et al. 2005 method based on Hildebrand 1983) shows a

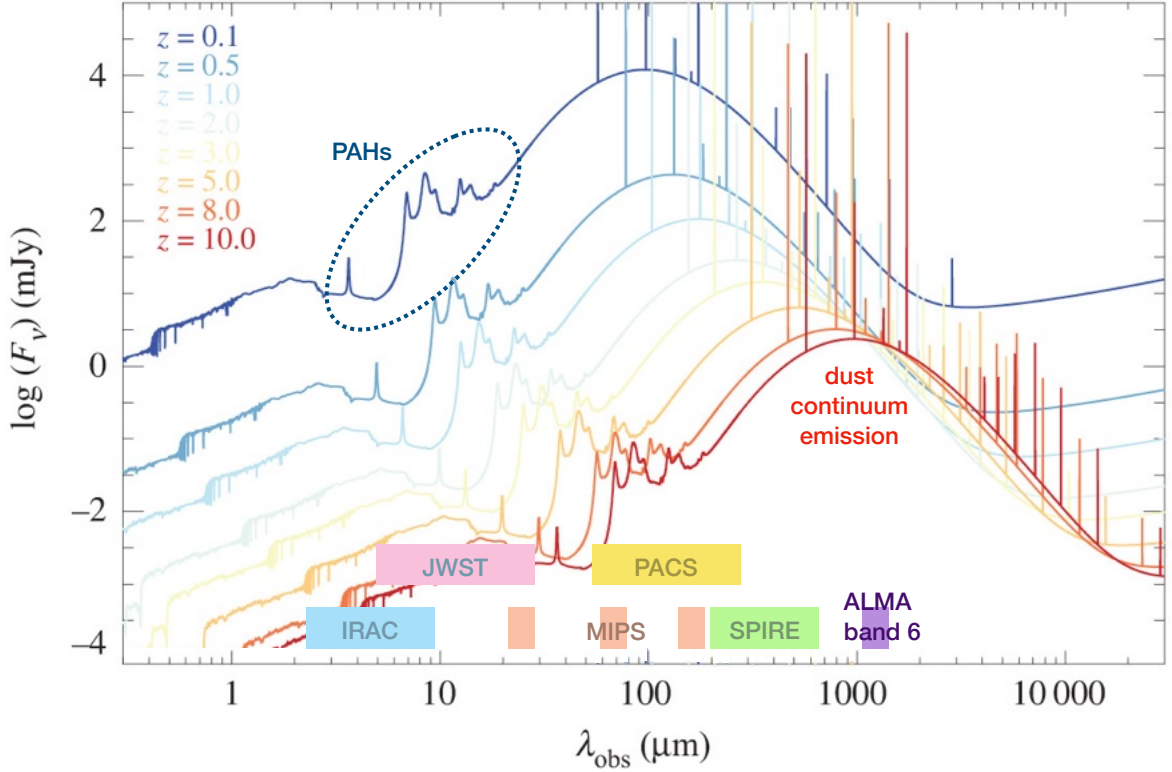


Figure 1.3: The spectral energy distribution of a galaxy at different redshifts (solid lines). Additionally, the observation bands of selected telescopes have been marked as well as PAHs and dust continuum emission. Adapted from Fig. 1a in Hodge & da Cunha (2020).

simple relationship between dust mass M_d in a galaxy at redshift z , flux density F_ν , and temperature. In this way, the FIR SED can be described by the modified black-body dust distribution and a single average dust temperature, T_{dust} , for a given galaxy:

$$M_d = \frac{F_\nu D_L^2}{(1+z)\kappa_\nu B_\nu(T_{dust})}, \quad (1.1)$$

where D_L is a luminosity distance, $B_\nu(T_{dust})$ is the Planck function, κ_ν is the mass absorption coefficient of dust at rest frequency ν .

1.1.2 Stellar and non-stellar dust sources

It is known that dust is not only relevant in the context of the ISM but is also one of the main factors defining the evolution of stars and entire galaxies. Formation of dust grains takes place in rapidly-cooling gas of stellar outflows (Yamamoto & Hasegawa 1977) since it requires an environment of gas densities $> 10^{13} \text{ cm}^{-3}$ (Sarangi et al. 2018), and a relatively low temperature. A temperature lower than 2000 K is assumed as the maximum temperature for grains to be formed and this temperature depends on the environment. The nucleation and condensation processes are responsible for

the transition between the molecular gas phase to the solid dust state, forming dust nuclei and clusters (Cherchneff & Dwek 2009; Sarangi & Cherchneff 2013). Molecules lose their kinetic energy with decreasing temperature and combine to form a cluster of molecules and finally to form a dust grain. In a carbon-rich environment, the temperature of the formation of amorphous carbon or silicates oscillates around 1700 K (Duley & Williams 1981; Sharp & Wasserburg 1995; Lodders & Fegley 1995; Jäger et al. 1998; Mutschke et al. 1999; Pascoli & Polleux 2000; Dartois et al. 2004; Jäger et al. 2009; Jones & Nuth 2011), while for graphite and PAHs it is less than 1700 K. (Draine & Lee 1984; Cherchneff et al. 1991; Sharp & Wasserburg 1995; Cherchneff 2011). In the case of an oxygen-rich environment, the temperature distribution is more diverse. Corundum grains condense at the temperature of ~ 1700 K (Gail 2010; Koike et al. 1995). Olivines and pyroxenes form at approximately 1300 K (Koike et al. 1993, 2000; Gail 2010; Zeidler et al. 2011) while the lowest temperature, reaching only 800 K, characterises magnetite, calcite, and dolomite formation environment (Koike et al. 1981; Posch et al. 2007; Gail 2010).

The stellar outflows arise during the last stellar evolutionary phases. Stellar evolution varies significantly with the initial mass of a star. Stars of stellar mass (M_{stellar}) about one solar mass ($1M_{\odot}$) evolve slowly toward the giant stage at the end of their relatively long life (10 Gyrs). However, a star with an initial mass of $\sim 40 M_{\odot}$ evolves in a shorter timespan (in a few Myrs) to the supergiant phase.

There are two stellar sources that produce dust. Asymptotic giant branch stars (AGBs) are characterised by an initial mass in the range of $0.8\text{--}8 M_{\odot}$, and quite strong winds. The winds are responsible for increased mass-loss rates (Schöier & Olofsson 2001). Dust is produced in their cooling dense ejecta (Valiante et al. 2009). The theoretical dust yield per one AGB star (how much dust one star can produce) is less than $4 \times 10^{-2} M_{\odot}$ (Morgan & Edmunds 2003; Ferrarotti & Gail 2006; Ventura et al. 2012; Nanni et al. 2013, 2014; Schneider et al. 2014). Due to the relatively low initial masses, AGB stars need a few hundred of Myr up to ten Gyr to start producing dust (Valiante et al. 2009). In their recent studies on dust formation Marini et al. (2023) concluded that the dust production mechanism continues with high efficiency until the very final AGB phases, resulting in dust yields of $0.012 - 0.025 M_{\odot}$.

The second stellar phenomenon that results in dust production is a supernova (SN) explosion. This event marks the end of the lifetime of a massive star ($8 < M_{\text{stellar}}/M_{\odot} < 40$). The dust production takes place in their expanding ejecta (Hoyle & Wickramasinghe 1970), a few hundred or thousand days after a SN explosion. SNe type II (core-collapse SNe) are the main SN dust sources in the Universe (Cherchneff 2010). SNe type II are the most common SN type (Schulze et al. 2021) and are mainly observed in spiral arms of galaxies where new stars are still forming. There are also some theoretical studies on dust production by SNe type Ia, thermonuclear explosions in binary systems composed of a donor and a white dwarf. Nozawa et al. (2011) showed that the dust produced in the expanding ejecta is not able to survive in the system due to the so-called reverse shock. This shock can sweep up the matter and destroy the dust that has just been created and can travel much faster through the system environment (compared to reverse shock in SNe type II) due to the lack of a hydrogen envelope, which acts as a shield that slows down the reverse shock. High gas density in the ejecta

causes very effective dust grain erosion by gaseous ions (Schneider & Maiolino 2023). This indicates that SNe Ia are not effective in the dust production process. Dust produced by this type of SNe has not been detected so far. There are also superluminous SNe, 10-100 times brighter than traditional core-collapse SNe (Quimby et al. 2011; Gal-Yam 2019; Inserra 2019). However, these objects are ineffective in creating dust, resulting in $5 \times 10^{-4} - 10^{-2} M_{\odot}$ of dust (Chen et al. 2021). Their small contribution to the mass of dust in the Universe is additionally determined by the low frequency of occurrence (Schulze et al. 2021).

In the Local Group, the majority of observed dust mass is formed by AGB stars and SNe (Gall et al. 2011b). SN 1987A observed in the Large Magellanic Cloud has become the most known dust production event (Lucy et al. 1989). The dust production process took place a few hundred days after the explosion. Shortly after that, the progenitor was identified, which unexpectedly turned out to be a blue supergiant. In 2011, based on Herschel data, Matsuura et al. (2011) reported 0.4 - 0.7 M_{\odot} of dust in SN 1987A remnant.

Another well-studied case of SN dust production is Cassiopeia A located in our Galaxy. De Looze et al. (2017) in their multiwavelength analysis obtained 0.4 – 0.6 M_{\odot} of cold (~ 30 K) dust, assuming that it is composed of silicate-type grains and carbonaceous grains in equal proportion. The majority of Cas A cold SN dust is concentrated inside the reverse shock, which may suggest that the recently formed dust has been destroyed by this shock. The decrease in dust mass beyond the reverse shock indicates that approximately 70 % of the dust mass is destroyed as it travels through the reverse shock. Shahbandeh et al. (2023) reported the *JWST* Mid-Infrared Instrument (*JWST* MIRI) dust detection of two low- z supernova remnants, 18 and 5 years after the SN explosion. The outcome of their SED fitting provided estimates of the dust mass lower limits of $M_{dust} > 0.014 M_{\odot}$ for the older object and $M_{dust} > 4 \times 10^{-4} M_{\odot}$ for the younger one.

Stellar production of dust in the galaxies of the early Universe places one requirement on stars; they must be mature enough in a short time to start dust production, which constrains the initial mass to be relatively high. At redshift $z > 6$, only stars with the minimum stellar mass of about $3 M_{\odot}$ are considered as potential dust producers (Gall et al. 2011c) because only these stars could evolve to the late outflow phases. SNe are considered to be one of the primary stellar dust producers in the early Universe due to their short lifetimes. Maiolino et al. (2004) presented the first direct evidence for dust production by SNe in quasar at $z = 6.42$. Theoretical dust yields per SN of population III stars (which are a theoretical population of very massive stars existing in the early Universe) is less than $1.32 M_{\odot}$ (Nozawa et al. 2003) but only less than $0.1 M_{\odot}$ survives the reverse shocks phase.

There is yet another, non-stellar mechanism contributing to the growth of dust observed at low and high redshift (Draine & Salpeter 1979; Dwek & Scalo 1980; Draine 2009; Michałowski et al. 2010a). Interstellar cold clouds are suitable regions for dust grains to grow due to the accretion of gas-phase metals (Inoue 2003; Draine 2009; Asano et al. 2013). Dense environments, characterised by a number density of hydrogen molecules of $\sim 10^3 \text{ cm}^{-3}$ (Dwek & Scalo 1980; Hirashita 2000), have ideal conditions for effective growth, where an ice mantle is created on a dust grain surface. Gas accretion is

also accompanied by grain coagulation, joining of particles over low-velocity collisions, and these two mechanisms together can have a significant impact on the grain growth in the ISM. Recent studies of the mass of dust detected in SN 1987A resulted in the hypothesis of accretion and coagulation of the dust grains in this system over the last twenty years (Wesson et al. 2015; Bevan & Barlow 2016). Research presented by Ferrara et al. (2016) on the dust grain growth in high-redshift galaxies, via gas accretion in the diffuse ISM, showed that this process can face some difficulties. The accretion may occur too slowly which is related to too low density of the medium. The dust temperatures could be too high, so Si and O atoms cannot stick to the grain surface and within seconds these go back into the gas phase. Lastly, positively charged grains by strong UV radiation will repel ionised Si and C from each of their surfaces. Yet, far more favourable conditions are found in molecular clouds, characterized by lower temperatures and higher gas densities, facilitating shorter accretion and a buildup of the ice mantle around a grain in molecular clouds (e.g. Caselli & Ceccarelli 2012; Boogert et al. 2015). Ferrara et al. (2016) considered supernovae as the main dust producers.

Since the condensation of refractory elements on the surface of dust grains helps them to grow (Jones & Nuth 2011), the evolution of dust is closely related to metallicity (Hirashita 2013, e.g.). Massive stars create metals when they die, which is why this predicts a constant dust-to-metal ratio (Franco & Cox 1986). In their work on the dust production and the dust evolution extensions in the semi-analytic model, Parente et al. (2023) reproduced the observed correlation between dust-to-gas mass ratio and metallicity Rémy-Ruyer et al. (2014); De Vis et al. (2019); Popping & Péroux (2022). As metallicity increases, the dust-to-gas mass ratio also increases, and this is noticeable at every redshift bin tested (up to $z < 3$). Because M_{stellar} and SFR are dependent on metallicity, it follows that metallicity is the primary physical parameter of the galaxy that determines the observed dust-to-gas mass ratio values (Rémy-Ruyer et al. 2014).

The estimated amount of dust is influenced by the stellar initial mass function (IMF). This function describes the distribution of masses of individual stars formed during a star formation episode. If the galaxy is dominated by low-mass stars, possible dust production will begin much later - due to the time it takes a star to reach the AGB phase during which they lose mass - than in the case of massive stars that evolve over tens of millions of years. The shape of the IMF is difficult to infer because direct detection and counting of stars are possible only among the closest neighbours of our Galaxy and within it (Offner et al. 2014). The distribution of stellar masses can be described by different IMFs. A power law is used for estimates of the total number of massive stars (above $1 M_{\odot}$), as it was presented by Salpeter (1955). The IMF distribution becomes less obvious for less massive stars, where originally power-law was assumed, but more recent research indicates lognormal distribution Chabrier (2003a) or a sequence of power-laws (Kroupa 2001, 2002).

Ongoing research is exploring the possibility of dust formation in active galactic nuclei (AGN) accretion disc winds. Elvis et al. (2002) emphasised that favourable conditions may exist in broad-line outflows for dust formation, similar to AGB outflows, resulting in dust yield of $\sim 10^{-2} M_{\odot} \text{ yr}^{-1}$. In their theoretical studies, Sarangi et al. (2019) examined four regions affected by AGN outflows driven by a magnetic field.

Dust nucleation and condensation can occur near the accretion disc plane. This results in the formation of a dust torus surrounding the central engine. There are also regions of sublimation, characterised by high temperatures in which a transition from the solid state to the gaseous state occurs. Due to temperature, $T > 2000$ K, dust grains may be ionized or even destroyed. It is worth noting that grain growth is also possible via accretion and coagulation, but only further away from the centre. Dust formation and grain growth in AGN outflows are still under active investigation, and to accurately describe this phenomenon, observations with spatial resolution reaching several hundred parsecs are needed.

1.1.3 Dust removal mechanisms

Answering the question of how dust is removed faces some problems. The gas outflows, inflows from the intergalactic medium, and continuous dust production and destruction by SNe and AGB stars make the whole process a combination of several components. Each of these components and mechanisms operates on a different time scale. Most of today's constraints on this subject are based on simulations and theoretical predictions, which can describe this problem in detail, but depending on the adopted assumptions it is possible to get contradictory results (Jones & Nuth 2011). Processes that may contribute to dust loss are described in what follows.

Incorporation in newly formed stars (astration) occurs regardless of the source of dust (Gall & Hjorth 2018) and can be efficient in star-forming regions. Ferrara & Peroux (2021) studied dust density evolution in the last 8 Gyrs of the Universe evolution and found out that 11–49% of the dust mass is destroyed by astration. This fraction depends on the contribution of SN to dust destruction; the higher their efficiency, the lower the contribution of astration.

A SN explosion does not just create a shock wave travelling outwards. A reverse shock wave forms when a forward SN ejecta runs into an ambient medium, and only then bounces back or propagates an inward wave. Such reverse shock wave can destroy a considerable amount of newly formed dust (Temim et al. 2015; Bianchi & Schneider 2007; Cherchneff 2010; Gall et al. 2011c; Lakićević et al. 2015). The efficiency of this process is influenced by the size, chemical composition, and distribution of dust grains. Based on studies on the initial grain size distribution in SNR Cassiopeia A, Kirchschrager et al. (2019) revealed that about 30% of the carbon grains (~ 10 – 50 nm radii for high gas densities, or ~ 0.5 – 1.5 μm radii for low and medium gas densities) and 40% of silicate grains (~ 10 – 30 nm) are able to survive the reverse shock pass. A forward shock can be destructive at low velocities, destroying pre-existing dust. As presented by Bocchio et al. (2014) a forward shock can easily destroy the smallest carbonaceous grains moving only 50 km s^{-1} through ambient ISM. Core-collapse SNe are associated with a recent star formation epoch. The lifetime of the CC-SN progenitor is much shorter than that of a progenitor of SN Ia, which indicates different dust removal timescales in galaxies considering different SN types. It is not clear how much dust (new and pre-existing) is destroyed by SN shocks.

Another process is ionisation by planetary nebulae (PNe), during which heating of gas by the ejecta can lead to the destruction of dust (Conroy et al. 2015). Planetary

nebulae are systems composed of a low or intermediate-mass star in its post-AGB phase, surrounded by a previously ejected gas and dust envelope. A red giant star, known for its comparatively low temperature and large size, throws out its outer gaseous layers as its core contracts and emits radiation, transforming into a new source. After this ejection phase the exposed nucleus remains in the very centre, emitting UV radiation. The central object, usually a white dwarf, ionizes nearby medium for only about a few thousand years. This heating, done by the ejecta colliding with the gas surrounding the central object, produces ionised medium. In their recent work Dell’Agli et al. (2023) presents that up to $\sim 60\%$ of already existing dust can be destroyed during the PN ionisation phase.

Stellar winds driven by SN explosions, in highly star-forming galaxies like in M82 (Walter et al. 2002), may also contribute to dust loss in galaxies. Galactic outflows get rid of dust grains and this process can be very effective due to radiation pressure (Bianchi & Ferrara 2005). Dust grains are transported from the galactic disc to the halo by outflows and this process can increase metal abundances in the galaxy’s environment. Dust outflow depends on grain mass. The heaviest grains are unable to escape from the gravitational well, while the smallest experience collisions with atoms and ions resulting in the inability to escape from the disk (Draine & Salpeter 1979). In their analysis Slavin et al. (2015) focused on dust destruction by SNe, which resulted in a dust removal timescale of 2–3 Gyr of silicates and carbonaceous grains. However, the authors pointed out that a comprehensive description necessitates an understanding of the morphology of the interstellar medium. In the high redshift Universe, even at $z \sim 10$, outflows lead to removal of grains with radii $\sim 0.1 \mu\text{m}$ (Hirashita & Inoue 2019).

The dust has also been detected in small compact regions around AGNs (Ichikawa et al. 2017, 2019). Matter accretion onto the black hole located in the centre of the galaxy creates AGN-driven outflows (King & Pounds 2015). Recently, Tazaki & Ichikawa (2020) proposed a new dust destruction mechanism driven by the AGN radiation pressure. This accelerates dust grains, which are destroyed by kinetic sputtering. The smallest grains are quickly destroyed while larger ones are moved away from galaxy centres.

Hot gas present in galaxies can also cause erosion of dust particles by sputtering. The smallest grains are the most vulnerable to this mechanism (Bocchio et al. 2012). Micelotta et al. (2010) studied PAHs in a hot gas (10^3 – 10^8 K) and concluded that dust grains would be mainly destroyed by collisions with electrons rather than absorption of X-ray photons. Collisions would lead to quite a short destruction time of about 20 Myr.

Analytical models presented by Dwek et al. (2007) for the evolution of the ISM components in high redshift galaxies showed that the efficiency of the dust grain destruction is highly uncertain because it depends on the ISM morphology. Gall et al. (2011a) developed a numerical model of galactic chemical evolution and studied the effect of galaxy properties on the evolution of dust in starburst galaxies at high redshift. In their analysis, they noticed a strong dependency between the IMF and the total dust mass, which is additionally correlated with the mass of the galaxy. SNe are responsible for a majority of dust mass produced at early epochs. The mechanism considered to contribute to the dust destruction is SN shocks. Shocks have a significant

impact on dust removal considering top-heavy IMFs, when many more massive stars, SNe progenitors, are formed. Theoretical considerations on the dust removal timescale were carried out a few decades ago. Barlow (1978) studied sputtering of dust grains in regions of ionised hydrogen (H II regions), inter-cloud medium, cloud-cloud collisions shock waves, and SN remnants. Based on his studies he concluded that SN remnant shock waves lead to ice grains lifetime of about 2×10^8 yr.

1.1.4 Early-type galaxies

To begin research on the mechanisms by which dust is removed from galaxies, we must start by selecting a well-defined galaxy sample. The galaxies must be rich in dust to be detected. The Hubble visual morphological classification (Hubble 1926) can be advantageous, presenting a sequence that describes galaxies based on their optical appearance. Large amounts of dust are observed in spiral galaxies, so-called late-type galaxies. Spiral galaxies are distinguished by arms that spiral out from a central bulge or central bar composed mainly of old stars. Young stars, some planetary systems, and the ISM are located in the spiral arms. Young stars are still observed in these galaxies, so star formation is still ongoing. In the context of dust destruction, the presence of recent star formation may negatively impact the overall analysis because these new stars can create new dust. Therefore, galaxies that are retired (which have stopped forming stars) are a good choice for studying the mechanism of dust removal. These are passive galaxies with a low star formation rate (SFR) value. There are also late-type galaxies which are becoming passive. However, usually, passive galaxies have an ellipsoidal shape, featureless, and smooth brightness distribution highest in the centre, and decreasing with distance from the centre. These have been called early-type galaxies by Hubble. At that time Hubble thought that galaxies evolve from early to late-type, which according to our current knowledge is the opposite. However, we still use the original Hubble's original nomenclature.

How can the morphological type of a galaxy be determined? More precisely, how can the ellipsoidal shape be defined? One of the basic and first approaches to this topic is visual classification. As previously mentioned Edwin Hubble provided the first systematic morphological classification of galaxies (Hubble 1926) which was expanded in subsequent years by de Vaucouleurs (1959). Based on the appearance of the galaxy in optical imaging, we are able to determine its type. Galaxy Zoo (Lintott et al. 2008) is one of the unusual approaches to this topic. It is a platform where volunteer users assess the type of galaxy by visual inspection and based on the response statistics, a visual morphological type is assigned to the examined galaxies. The shape of galaxies is also reflected in their colour. Elliptical galaxies, mostly made up of old metal-rich stars, appear redder (Humason 1936; Hubble 1936). By brightness examination of a selected galaxy, using two filters u (UV range) and r (IR range), the difference between these two values determines the type of galaxy. As presented in Strateva et al. (2001) for galaxies at redshift up to 0.4, if $u - r$ is greater than 2.22 the examined galaxy most probably is an early-type object with elliptical morphology. Nadolny et al. (2021) showed that this value can be used even for galaxies up to $z \sim 2$.

The brightness distribution within the galaxy's boundaries depends on the shape

of the galaxy. Early-type galaxies have a smooth brightness distribution with a clear decline in intensity with radius, while the brightness in the case of late-type galaxies is more uneven. The Sérsic profile describes the galaxy’s intensity distribution as a function of radius (Sérsic 1963, 1968; Graham & Driver 2005) and is given by eq.1.2:

$$I(r) = I_e \exp \left[-b_n \left(\left(\frac{r}{r_e} \right)^{1/n} - 1 \right) \right], \quad (1.2)$$

where I_e corresponds to the intensity at the effective radius r_e , i.e. the half-light radius which contains 50% of the galaxy’s luminosity. The so-called Sérsic index (n) is a parameter that defines the degree of flattening of the Sérsic profile and indicates how the light is distributed in a galaxy. The Sérsic profile reduces to familiar distributions for certain values of n . For instance, $n = 0.5$ is a Gaussian profile, and $n = 1$ is an exponentially declining profile. Sérsic index $n = 4$ is a de Vacouleurs $r^{1/4}$ profile, which has been used successfully to describe elliptical early-type galaxies. The higher this parameter is, the more centrally concentrated the galaxy is (Trujillo et al. 2001), and its surface brightness gradually decreases with increasing radius. Parameter b_n is a function that depends on the value of the Sérsic index. A commonly used, and less conservative Sérsic index limit is at $n = 2.5$ (Vulcani et al. 2014; Lange et al. 2015; Nadolny et al. 2021), the limit below which we classify galaxies as late-type galaxies. Fig. 1.4 summarises the entire above methodology of distinguishing elliptical galaxies from spirals using colours and the Sérsic index. It is visible that for $n > 2.5$ the galaxies are redder and more massive, and these galaxies tend to be elliptical.

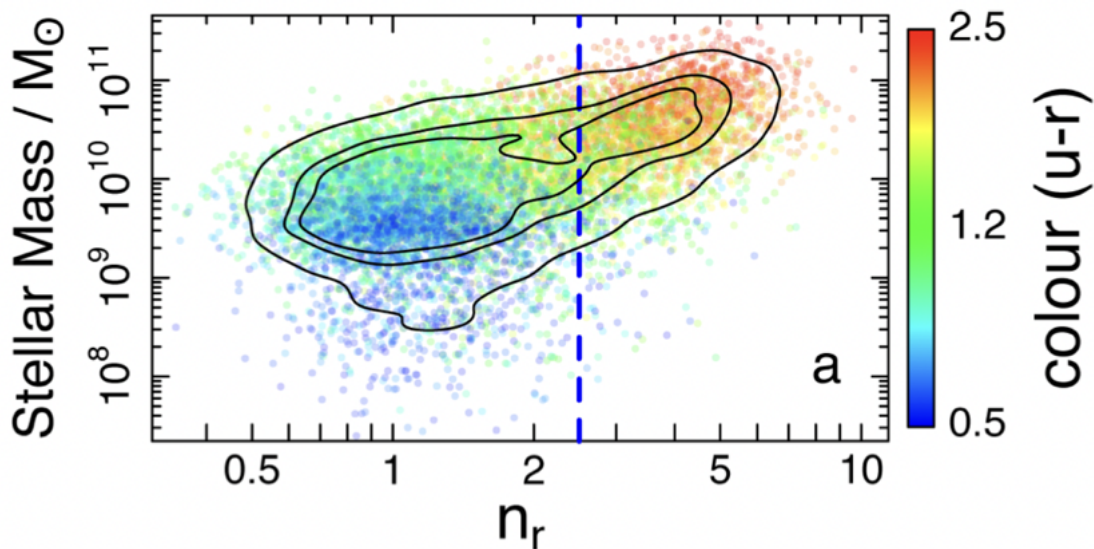


Figure 1.4: Stellar mass as a function of Sérsic index with $u - r$ colour bar. Figure 2(a) from Lange et al. (2015).

Analysing the dust destruction processes, we encounter a problem regarding the amount of observational data. The number of massive, early-type galaxies becoming passive is relatively low, so large-area surveys are needed to obtain significant samples. Instruments that are able to detect dust emission observe at infrared and submillimeter

wavelengths. Unfortunately, many existing telescopes with such detectors are not able to survey large areas of the sky. Due to their small fields of view, the largest and most sensitive interferometric instruments, such as ALMA, SMA, and NOEMA are not able to create large databases of thousands of objects that are required for the statistical analysis of dust loss in galaxies. This is why simulations and theoretical considerations are the main source of knowledge on dust destruction so far (e.g. Gall et al. 2011c; Croton et al. 2016; Parente et al. 2023).

Up to now, dust emission of only several dozen of dusty galaxies becoming passive has been analysed (Rowlands et al. 2012; Michałowski et al. 2019a). Rowlands et al. (2012) analysed dust in local early-type galaxies selected by their submillimetre emission. They selected 44 elliptical galaxies in which the high amounts of dust, expected for spiral galaxies, were observed. Rowlands et al. (2012) studied the relationship between the dust-to-stellar mass ratio and the specific SFR (sSFR, which is $\text{SFR}/M_{\text{stellar}}$) of the early-type galaxies compared to spiral galaxies. They noticed that the elliptical galaxies have lower dust-to-stellar mass ratios and sSFRs than spirals.

da Cunha et al. (2010) revealed a linear relationship between dust mass and SFR in low-redshift star-forming galaxies. As presented in Fig. 1.5 with increasing SFR, the amount of observed dust in star-forming galaxies increases linearly. Relatively high values of M_{dust} and SFR may indicate a recent merger event between two, or more, galaxies, while a departure from this linearity may indicate additional processes taking place in the galaxy, such as starburst, or quenching (Martig et al. 2009; Hjorth et al. 2014).

As shown by Michałowski et al. (2019a), there is evidence of an exponential decrease in the dust-to-stellar mass ratio with the mean stellar age for early-type galaxies (Fig. 1.6). This conclusion is based on 60 early-type galaxies observed by *Herschel*, up to $z < 0.32$. The sample size did not allow for studying the dependence of the dust decline as a function of other galaxy properties, thus larger sample is necessary to allow a deeper understanding of this process.

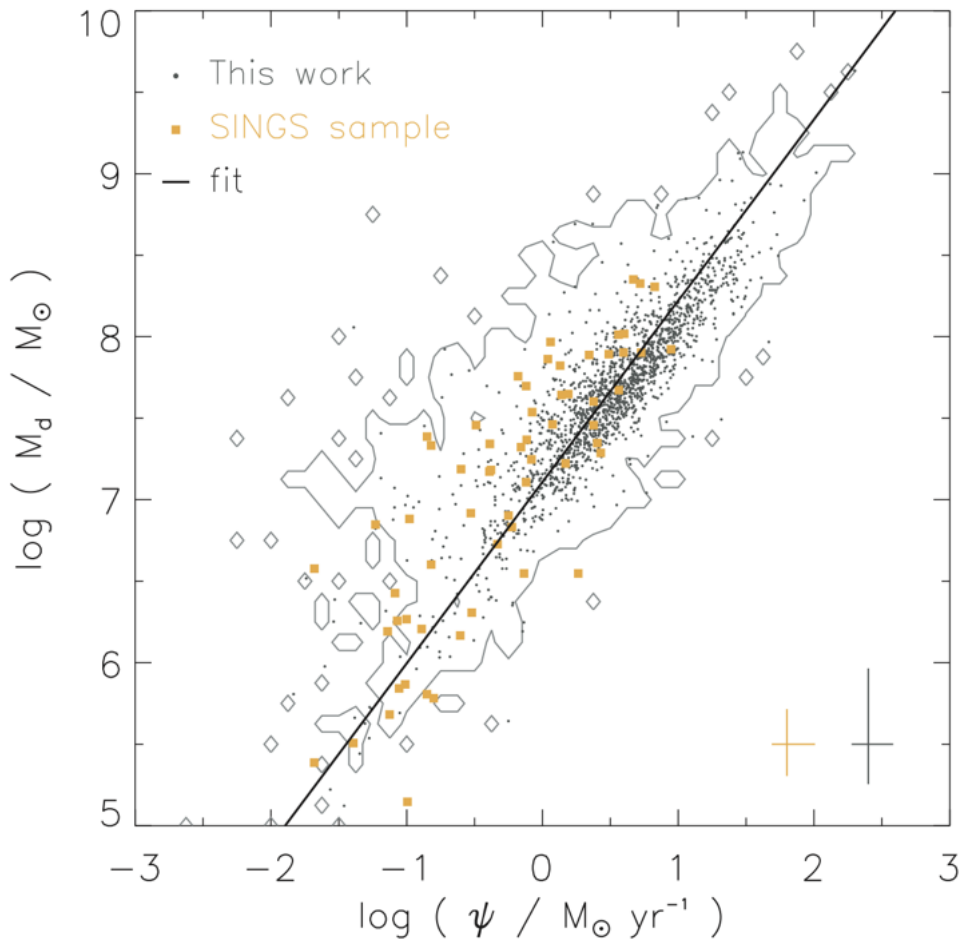


Figure 1.5: Dust mass as a function of star formation rate of star-forming galaxies. Figure 5 from da Cunha et al. (2010).

1.2 Cosmic gas and its atomic, molecular, and ionised state

Gas component dominates the total mass of the ISM in galaxies. About 75% of total ISM mass is made of hydrogen, in atomic (HI), molecular (H_2), and ionised (HII) form. All these states correspond to different physical conditions and processes that occur in these regions. Different techniques and wavelength ranges are needed to detect and analyse different gas phases.

Atomic hydrogen in the ground state (the lowest energy state) is composed of a proton and an electron and can experience a spontaneous electron spin-flip and emit a 21 cm photon (1420 MHz). The 21 cm line is used to trace hydrogen in its atomic form. Dust does not absorb this wavelength, which means that photons emitted during the spin-flip pass through dusty regions unchanged. Heintz et al. (2021) presented an alternative method for the atomic hydrogen mass estimation based on the [CII] line emission from star-forming galaxies, in which gamma-ray bursts appeared.

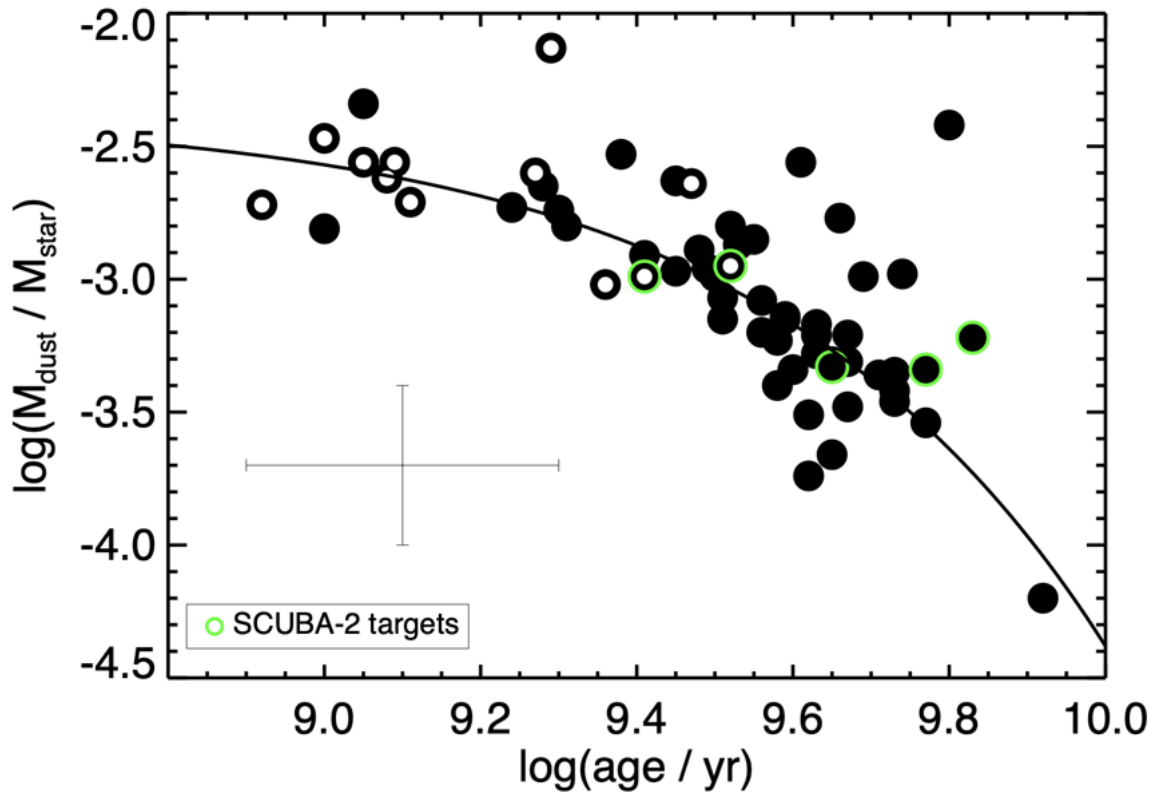


Figure 1.6: Dust-to-stellar mass ratio as a function of luminosity-weighted stellar age of Herschel-detected early-type galaxies from Rowlands et al. (2012) (black circles). The dust decline is detected. Figure 5 from Michałowski et al. (2019a).

As already mentioned, the surface of dust grains provides favourable conditions for the process of the formation of molecules. However, this process can also occur in the gas phase, where atoms or less complex molecules combine. Usually, the grain catalysis process (Gould & Salpeter 1963) takes place on the surface of a dust grain, when two hydrogen atoms are bounded, resulting in the formation of a symmetric hydrogen molecule. This is the reason why molecular clouds also contain significant amounts of dust. It is very important to emphasise the role of H_2 in star formation processes (Kennicutt & Evans 2012). For this process, cold molecular gas is one of the components involved. Dense molecular clouds, composed mostly of H_2 , are birthplaces for stars. Gas with a relatively low temperature, up to 20 K, is located in active stellar regions. Despite being the most abundant molecule in the Universe, the direct detection of molecular hydrogen is very limited (Inoue et al. 2020). H_2 is a diatomic molecule, which results in no permanent dipole moment. Therefore, H_2 is inefficient when it comes to radiation at temperatures of several dozen kelvins. The temperature required for moving to an excited state is at least several hundred Kelvin. Hence, its emission is weak and hard to detect. This is why we need another molecule as a proxy for H_2 to study the former in other galaxies, and especially to study high-redshift objects.

Not only hydrogen is used to describe physical conditions of the ISM in galaxies. CO is the second most abundant molecule in the Universe after H_2 . It is a polar molecule which results in the prospect of rotational transitions, with its most common transition

at 2.6 mm ($J=0$ to $J=1$). Excitation occurs already at ~ 5 K, and as a result, allows us to observe the cold gas component in star-forming galaxies. CO formation takes place in gas-phase. The CO line is commonly used as a proxy for molecular gas mass (Bolatto et al. 2013; Carilli & Walter 2013), however, this is not the only tracer. The neutral carbon line [CI] is also used for this purpose (Phillips & Huggins 1981; Papadopoulos et al. 2004; Jiao et al. 2017; Valentino et al. 2018). Nevertheless, using this tracer in environments characterised by high UV radiation and low metallicity might have limitations due to the ionisation of carbon under such conditions. In the case of late-type galaxies, we can detect molecular clouds in spiral structures. Measuring molecular gas with the help of CO can be problematic and underestimated in low-metallicity environments. In the case of a low-metallicity Universe, the [CII] line becomes useful as a total molecular gas tracer. Madden et al. (2020) showed that the total molecular gas mass is effectively traced by [CII], while CO fails to trace as much as 70-100% of the gas (H_2) in star-forming dwarf galaxies. In low-metallicity regions, UV photons can penetrate more deeply and photodissociate CO molecules. Subsequently, [CII] emitting layer is then formed around the remaining CO region (CO-dark gas, Papadopoulos et al. (2002); Röllig et al. (2006); Wolfire et al. (2010); Glover & Clark (2012)). Additionally, H_2 photodissociation occurs and, as a result, the molecular gas becomes optically thick. H_2 region is then located between the previously mentioned CO core and the outer layer of [CII]. All the above indicates that both tracers, CO and [CII], should be taken into account when determining total molecular gas mass. [CII] $158\mu\text{m}$ is considered one of the cooling lines for the neutral gas and a tracer of SFR (the brightest line from star-forming galaxies). Moreover, if this emission is spatially resolved, we can make measurements of the dynamical structures in galaxies. The [CII] line is also used to estimate the mass of H_2 in high- z galaxies (Zanella et al. 2018; Tacconi et al. 2020). Similarly, dynamical masses presented by Zavala et al. (2018) are determined based on the FWHM of [CII] emission and the size of the galaxy. [OIII] $88\mu\text{m}$ is also a cooling component and it significantly affects the ionised environment. Massive O-type stars are responsible for their presence.

H II regions in galaxies contain ionised hydrogen gas, wherein hydrogen atoms undergo electron loss owing to the intense UV radiation emitted by hot, massive stars. Hence, these regions originate predominantly in areas undergoing active star formation. The ionisation creates H II regions that emit characteristic recombination lines, such as $H\alpha$ (at a wavelength of 6563 \AA). The $H\alpha$ equivalent width serves as an excellent indicator of massive OB-type stars (e.g. Kennicutt et al. 1989; Lawton et al. 2010), effectively delineating recent star formation of the order of 10 Myr, corresponding to the lifespan of an OB star (Stasińska & Leitherer 1996; Fernandes et al. 2003; Kennicutt & Evans 2012; Haydon et al. 2020), therefore it can be used as an age proxy.

1.2.1 Gas detection and gas mass calculation

Similarly to dust, the gas is observed in the infrared and radio waves. However, gas emission does not take the form of a black body. Gas in galaxies consists mainly of atoms and ions. This gas emits radiation via specific atomic or molecular transitions, emission lines, rather than the thermal mechanisms typical of black body radiation.

The temperature of the gas within galaxies can exhibit significant variations based on its location, density, and the influence of nearby stars, galactic nuclei, or the CMB. Therefore it does not emit in the continuum, unlike dust.

HII regions are relatively straightforward to observe due to the recombination process that releases detectable photons. In contrast, HI regions emit spontaneously, but the extensive presence of neutral hydrogen atoms makes their emission widely observable. These regions are often observed at considerable distances from radiation sources.

In their research on dust and gas in spiral galaxies Devereux & Young (1990) presented total mass estimation of HI clouds. They showed a simple relationship between 21cm flux and the mass of an atomic region:

$$M_{HI} = 2.35 \times 10^5 D^2 f_{HI} [M_{\odot}], \quad (1.3)$$

where D in Mpc is a distance to the cloud, f_{HI} is a flux in Jy km s^{-1} .

Detecting H_2 directly poses challenges, necessitating the use of other molecules like CO or dusty regions as tracers. As reported by Togi & Smith (2016), H_2 can be detected solely in gas with temperatures surpassing approximately 80 K. Hence, the emission of other molecules has to be used to trace H_2 . Rotational transitions in CO are detectable at radio to sub-millimeter wavelengths. This mechanism allows us to estimate a total molecular mass component. Assuming a constant ratio between H_2 and CO, we can estimate the mass of molecular hydrogen. This, of course, carries some uncertainties due to the lack of a strict and specific value of this ratio, which varies significantly between different environments.

Equation 1.4 (Bolatto et al. 2013) presents conversion between the CO 1–0 luminosity ($L_{CO(1-0)}$) and the total molecular mass (M_{mol} including the helium contribution, $M_{mol} \sim 1.36 M_{H_2}$).

$$M_{mol} = \alpha_{CO} \times L_{CO(1-0)} [M_{\odot}]. \quad (1.4)$$

The CO-to- H_2 conversion factor α_{CO} may vary within galaxies and at different epochs (Genzel et al. 2012; Sandstrom et al. 2013). In the Milky Way and some nearby spiral galaxies $\alpha_{CO} \sim 4.4 M_{\odot} (\text{K km s}^{-1} \text{ km}^{-1} \text{ pc}^{-2})^{-1}$ has been obtained (Solomon et al. 1987; Strong & Mattox 1996; Abdo et al. 2010).

1.3 Gamma-ray bursts

Gamma-ray bursts (GRBs) are remarkably energetic and luminous transient events, observed in distant galaxies (Meegan et al. 1992) almost at all redshifts, with the furthest detected GRB 090423 at $z=8.2$ (Salvaterra et al. 2009; Tanvir et al. 2009). They are explosions emitting in the most energetic range of the electromagnetic spectrum, gamma rays. These events last from ten milliseconds to even several hours. GRBs have been detected for the first time by the Vela satellite in 1967, which original purpose was to control likely nuclear tests in space. Only several years later Klebesadel et al.

(1973) assigned a cosmic origin to GRBs. The distribution of observed GRBs in the sky is homogeneous without any obvious clustering. There is a clear bimodal division of GRBs according to the duration of their prompt emission (Dezalay et al. 1992; Kouveliotou et al. 1993) on short ($t < 2\text{s}$) and long GRBs ($t > 2\text{s}$). Fig. 1.7 presents the distribution of burst timescale where the bimodality can be observed.

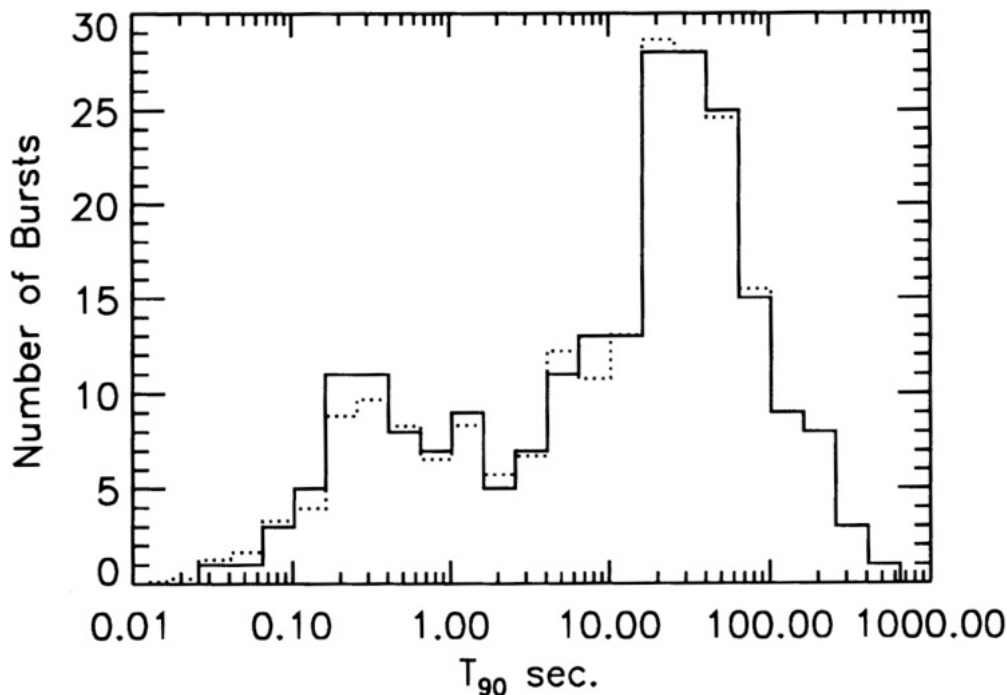


Figure 1.7: Burst timescale for the 222 GRBs from the first BATSE catalogue. Figure 1(a) from Kouveliotou et al. (1993).

The timescale differentiation visible in the observations is caused by the contrasting nature of the progenitors of the two types of GRBs. Collisions of two neutron stars or a neutron star-black hole pair are considered to be the sources of short GRBs (Hjorth et al. 2005; Villasenor et al. 2005; Abbott et al. 2017; Goldstein et al. 2017). As they emit gravitational waves, they lose their orbital energy, which results in merging and eventually collapsing into a black hole. That is why short GRBs seem to be ideal candidates for gravitational wave emitters (Abbott et al. 2017). On the other hand, very massive stars during their last stage of evolution collapse and explode as hypernovae (more energetic than a typical supernova) and eject their outer layers. In the next stage, the progenitor starts to emit strong gamma radiation that can last several seconds to hours (Hjorth et al. 2003; Stanek et al. 2003; Levan et al. 2016). Statistical studies show that the frequency of long GRBs is much higher than the short ones (Paciesas et al. 1999; Sakamoto et al. 2011).

Fig. 1.8 presents a GRB sketch from the moment of explosion up to the emission at longer wavelengths. An explosion or merger of the progenitor creates a beamed relativistic outflow, which kinetic energy is dissipated during the prompt emission. The uniqueness of GRBs is the so-called afterglow, an emission observed across longer wavelengths for a longer time than the prompt emission. GRB detection in the gamma range only leads to an estimate of the location in the sky, but detection at longer

wavelengths e.g. the visible range allows for identifying the host galaxy in which the explosion occurred. The primary explosion produces an external shock wave and, as it moves away from the source, it interacts with interstellar and circumstellar medium. Accelerated electrons in the magnetic field emit synchrotron emission which then can be observed in the entire spectrum, from gamma to radio. The expanding shock velocity is reduced by matter encountered along the way. This slowdown causes a loss of energy and, consequently, afterglow detection shifts towards longer wavelengths. Afterglow detections are difficult and may be disturbed by the environment in which the explosion occurs. Dusty molecular clouds, located close to GRB, could absorb most of the emission (Reichart & Price 2002). The first objects for which no afterglow was detected at the optical range were called "dark GRBs" (Fynbo et al. 2001). Since 1997 more than 2500 GRBs have been catalogued with defined locations, but only $\sim 37\%$ of them would have optical afterglow detections ¹. Jakobsson et al. (2004) presented a definition for dark GRBs, assuming that an optical-to-X-ray spectral index $\beta < 0.5$. Even deep follow-up observations would not reveal some bursts in the visible range. The timing of observations also plays a big role in the detection, because afterglows may decay as power laws. An afterglow spectrum in the visible range enables the estimation of the GRB redshift and sheds light on the progenitor nature. Absorption lines in the spectrum usually come from the host galaxy and are used to estimate the redshift.

Right after the explosion a prompt emission starts, i.e. emission at gamma waves, the detection of which depends on the axis of rotation of the progenitor. A relativistic jet radiates from the very centre of a collapsed massive star passing through the outer layers, following the magnetic field lines outwards, and spreading out into the surrounding gas and dust environment. Since long GRBs are products of dying massive stars we could expect to observe them at the same position in the sky as SN. In 1998, the first evidence of linking a GRB with SN appeared, when the coordinates of GRB 980425 and SN 1998bw coincided within uncertainties (Galama et al. 1998). The following years brought further detections with spectroscopic evidence of SNe (e.g. Hjorth et al. 2003; Stanek et al. 2003; Pian et al. 2006; Starling et al. 2011; Schulze et al. 2014). A SN bump is observed in optical and near-IR waves several to several dozen days after a GRB explosion. In some cases, both a long GRB and a SN were detected almost simultaneously at the same position. This lends credence to the hypothesis that both events are caused by the collapse of massive stars. However, if the jet arrangement is at an angle not towards the Earth or is obscured by surrounding GRB material, gamma emission would not be observed, unlike SN, which emission is symmetrical. Further confirmation of this GRB-SN correlation comes from the type of host galaxies in which long GRBs are detected. The vast majority of the long GRBs are associated with galaxies that are actively producing stars (Christensen et al. 2004; Castro Cerón et al. 2006, 2010; Michałowski et al. 2008; Hunt et al. 2014; Levesque 2014; Nadolny et al. 2023) unlike short GRBs, which are observed in both elliptical and spiral galaxies (Prochaska et al. 2006; Fong & Berger 2013).

Lyman et al. (2017) have analysed almost 40 long GRBs and their hosts at $z < 3$, which were observed by the Hubble Space Telescope. They reveal that most of the

¹<https://www.mpe.mpg.de/~jcg/grbgen.html>

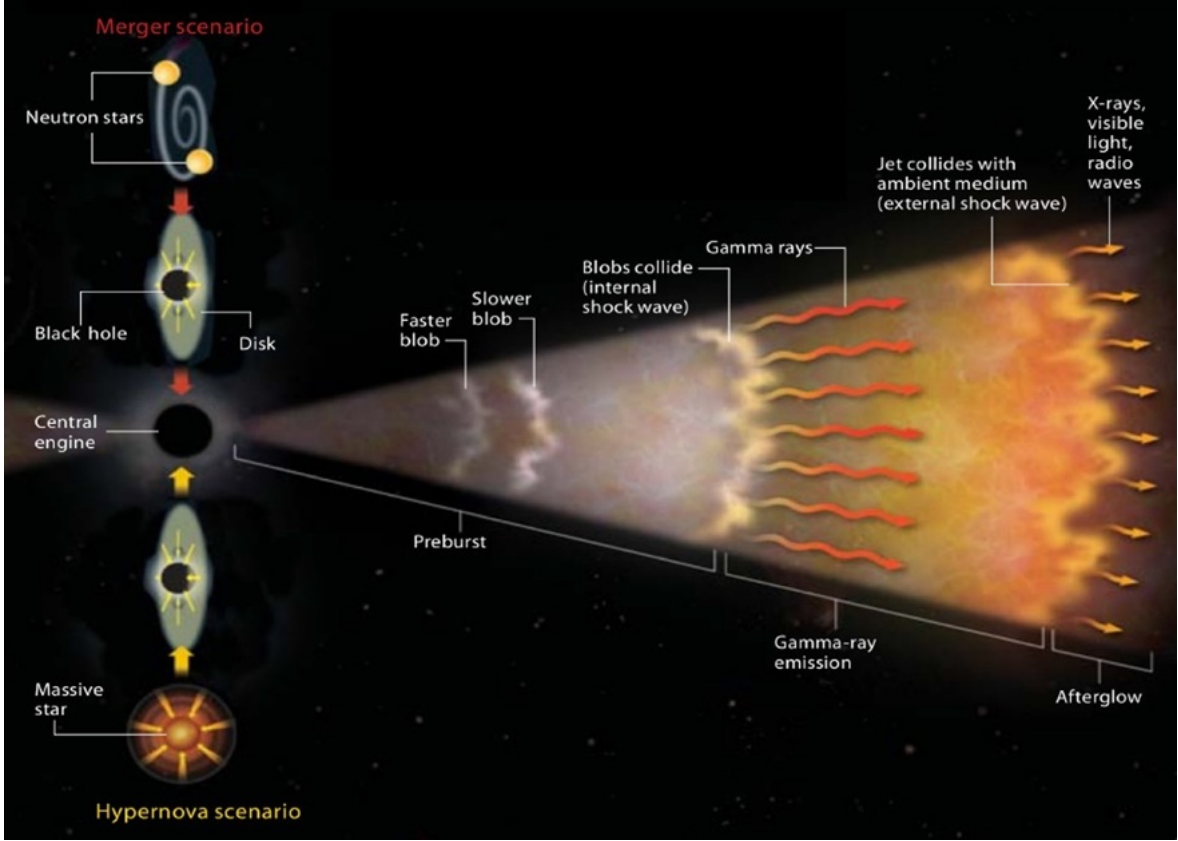


Figure 1.8: Illustration of the internal/external shock scenario for gamma-ray bursts. Figure 1 from Piron (2016).

galaxies' hosts are spiral-like or irregular galaxies which become less concentrated and more luminous with increasing redshift. The noteworthy result is that the analysed population of long GRB hosts seems much fainter than an SFR-weighted field galaxy population over the same redshift range. This suggests that long GRBs do not impartially trace the SFR. Schneider et al. (2022) investigated physical properties of 45 GRB hosts at $1 < z < 3.1$. GRB hosts at $z < 1$ are found to be smaller, with higher M_{stellar} and SFR surface densities compared to field galaxies at $1 < z < 2$, and above this redshift, these differences minimize. This observation suggests a potential evolution in the bias between GRB hosts and the general population of star-forming sources with redshift.

1.3.1 Long GRB environment

The characterisation of GRBs should not be based solely on studies of the moment of explosion and the flux evolution thereafter. We are unable to observe a GRB progenitor. This is why research conducted on the environment and the ISM distribution in which a given event took place is so crucial, improving our understanding of the physical conditions that support a GRB formation. Long GRBs, which are results of collapses of massive stars, are expected to be detected in blue host galaxies (Gorosabel et al. 2003; Le Floch et al. 2003; Fruchter et al. 2006), dense regions with high SFR (Christensen

et al. 2004; Castro Cerón et al. 2006; Ruiz-Velasco et al. 2007; Michałowski et al. 2014; Hunt et al. 2014). Within these galaxies, there reside young stars destined to culminate their existence as GRBs. This allows to use them as traces of regions of high ionisation (Fruchter et al. 2006; Blanchard et al. 2016; Lyman et al. 2017) but also of stellar evolution and starbursts in these galaxies. Nadolny et al. (2023) studied [CI] emission from GRB host galaxies at $z \sim 2$. The amount of molecular gas revealed to be comparable to that found in local ultraluminous infrared galaxies. The authors suggest that the galaxies under study represent merger systems captured during their transition from the main sequence galaxies to the starburst phase. Long GRBs demonstrate a tendency to locate in galaxies with low-metallicity (Stanek et al. 2007; Kewley et al. 2007; Perley et al. 2016; Palmerio et al. 2019).

Investigating the surroundings where a GRB explosion takes place also entails analysing the gas composition. As new stars emerge in the presence of molecular gas (e.g. Fumagalli et al. 2009; Carilli & Walter 2013; Rafelski et al. 2016), the inflow of gas into a galaxy from the intergalactic medium can stimulate a burst of star formation. Michałowski et al. (2018b) investigated and characterised new and archival molecular gas within 12 host galaxies of long GRBs. The examined sample exhibits molecular characteristics in line with those observed in other galaxies, e.g. SFR–CO luminosity relation, suggesting these host galaxies can serve as representative examples of star-forming galaxies.

Molecular gas is not the only gaseous component observed in or in the vicinity of galaxies hosting GRB explosions. Michałowski et al. (2015) analysed atomic hydrogen emission coming from galaxies that experienced GRBs. Extensive atomic gas reservoirs, coupled with minimal molecular gas mass in studied galaxies suggest that the star formation process may be initiated by the direct impact of atomic gas inflow from the intergalactic medium. Analysis of the spatial and velocity distribution of atomic emission from the GRB 980425 host galaxy, conducted by Arabsalmani et al. (2015), unveils a perturbed rotating gas disc. This indicates that the galaxy has experienced a recent minor merger, disrupting its rotational dynamics. It can be inferred that the merger likely contributed to the burst of star formation, in the place where this long GRB detection was made.

The study of the environment in which the GRB explosion occurred can be considered as the study of the matter from which the progenitor was created, during the short time of evolution of a massive star. Massive stars that shed their outer layers during the final phases of their lives are low-metallicity stars. The rate of mass loss depends on the metallicity ($\dot{M} \propto Z^{0.86}$, Vink & de Koter (2005)). By implementing the single progenitor model, it becomes apparent that to maintain the spinning cores essential for GRB formation, the metallicity must not exceed a few $\times 0.1 Z_{\odot}$ (e.g. Hirschi et al. 2005; Woosley & Heger 2006). Therefore, the metallicity of the environment, from which the progenitor of a long GRB originates, cannot be overlooked. In instances of higher metallicity, there is a risk of excessive angular momentum removal, making it difficult to form an accretion disk.

Synchrotron emission of galaxies occurs when electrons accelerated by core-collapse SN events are moving in a spiral motion around the magnetic field lines of the host galaxy (Condon 1992). This phenomenon manifests itself as detectable radio continuum

emission, serving as a convenient, unobscured, indicator of star formation activity in galaxies. Investigations into the detection of radio emissions in GRB host galaxies have yielded positive results (e.g. Perley et al. 2015, 2016; Klose et al. 2019). The SFR derived from radio typically yields significantly higher values compared to those obtained through UV/optical studies (Christensen et al. 2004; Michałowski et al. 2012).

1.3.2 Long GRBs with no SN detection

Nearly all long GRBs subjected to extensive spectroscopic observations are found to be accompanied by the SN type Ic with broad lines (Hjorth & Bloom 2012). In recent years, studies have been conducted on distinctive long GRBs in which no accompanying SN was observed. In 2006 two long GRBs were detected within about a month. GRB 060505 and 060614 (Fynbo et al. 2006; Della Valle et al. 2006; Gal-Yam et al. 2006) and were found to be located in two galaxies at low redshifts, $z = 0.089$ and $z = 0.125$ respectively, based on their optical afterglows. Both GRBs were located within galaxies undergoing active star formation. In the case of GRB 060505, only one detection in the optical was made, which was followed by deep upper limits. R-band magnitude analysis showed the difference between these two explosions and other recorded SNe accompanying long GRBs (SNe 1998bw, 2002ap, and 2006aj). SN components of GRB 060505 and 060614 would need to be at least 80 times fainter than a prototypical SN 1998bw. Galactic extinction also cannot be responsible for the lack of detection, since it amounts only to $E(B \sim V) = 0.02$ (Schlegel et al. 1998). All of the above leads to the conclusion that GRB 060505 and 060614 were not associated with significant SN emission.

Based on their multi-wavelength analysis, Michałowski et al. (2018c) described GRB 111005A as the third case of a SN-less long GRB and the second-closest GRB known to date. The GRB is located in a star-forming galaxy, ESO 580-49. Observations in the optical, NIR, and MIR failed to detect SN emission, implying that it would need to be at least 20 times fainter than SNe associated with other long GRBs. Moreover, the radio afterglow light curve displayed a plateau phase lasting a month, followed by a remarkably rapid decay. Such characteristics have not been observed previously in a GRB. The region of the explosion is characterised by 1–2 times solar metallicity, which is inconsistent with the core-collapse progenitor model.

GRB 060505, 060614, and 111005A have become an enigmatic subgroup of long GRBs. Further high-resolution observations of the environment in low- z host galaxies of these unique events may contribute to a more accurate description of the mechanisms leading to these explosions.

1.4 The aims of this thesis

The first aim of this dissertation is to explore the underlying mechanism behind the production of dust in galaxies of the early Universe. To investigate potential mechanisms, a sample of galaxies with redshifts exceeding 6 will be assembled. For all collected galaxies dust emission must be detected. The study will focus on two prominent sources of stellar dust production: AGB stars and SNe. Subsequently, dust yield calculations for selected galaxies will be conducted, using already published data on total stellar mass, gas mass, dust mass, and dynamical mass. This approach will enable the determination of the necessary dust mass production per AGB star or SN to account for the observed total dust mass in the examined galaxies. Results of this research are presented in Chapter 2.

The mechanism of dust removal from galaxies has not been completely understood yet. The enigma of how galaxies cease star formation and transition into passive ones continues to perplex scientists. The second aim of this thesis is to define the mechanisms involved in the removal of dust in ETGs and to explore how these mechanisms vary on physical and environmental factors. To address these puzzles and explore potential processes involved in depleting one of the cold ISM components in galaxies, a sample of dusty ETGs will be chosen. This sample will be significantly different from previous tests, containing several thousand detected objects. An analysis of the physical and observational parameters of the ETGs will allow the examination of possible dependencies between the dust evolution and parameters such as total stellar mass, SFR, total dust mass, the galactic environment, and redshift. Results of this research are presented in Chapter 3.

One of the most powerful phenomena in the Universe, long gamma-ray bursts are believed to result from the explosions of highly massive stars. However, recent observations of GRBs challenge this hypothesis. The final objective of this thesis is to conduct comprehensive environmental investigations of GRB 111005A. Previous studies indicate that this particular event deviates from its expected type and overall characteristics. Therefore, utilizing new HI data and previously published optical parameters for GRB 111005A, an analysis of its observed environment will be undertaken. Exploring the distribution of matter within the host galaxy concerning its centre will contribute to a better understanding of the prevailing conditions in the galaxy, and therefore, describe the possible mechanisms that led to this GRB explosion. Results of this research are presented in Chapter 4.

Chapter 2

Dust production in the first billion years of the Universe

The following Chapter published as Leńniewska and Michałowski 2019, *Dust production scenarios in galaxies at $z \sim 6-8.3$* , A&A, 624, L13.

Abstract

Context: The mechanism of dust formation in galaxies at high redshift is still unknown. Asymptotic giant branch (AGB) stars and explosions of supernovae (SNe) are possible dust producers, and non-stellar processes may substantially contribute to dust production, for example grain growth in the interstellar medium (ISM).

Aims: Our aim is to determine the contribution to dust production of AGB stars and SNe in nine galaxies at $z \sim 6-8.3$, for which observations of dust have been recently attempted.

Methods: In order to determine the origin of the observed dust we have determined dust yields per AGB star and SN required to explain the total amounts of dust in these galaxies.

Results: We find that AGB stars were not able to produce the amounts of dust observed in the galaxies in our sample. In order to explain these dust masses, SNe would have to have maximum efficiency and not destroy the dust which they formed.

Conclusions: Therefore, the observed amounts of dust in the galaxies in the early Universe were formed either by efficient supernovae or by a non-stellar mechanism, for instance the grain growth in the interstellar medium.

2.1 Introduction

Dust in the Universe can absorb and re-emit up to 30% of starlight in the infrared (Hauser & Dwek 2001). Hence, the formation of dust has become one of the most important topics in galaxy evolution.

It is well known that there are two types of stellar sources that produce dust. Asymptotic giant branch (AGB) stars, which are evolved stars with initial masses of

0.8–8.0 M_{\odot} , create dust in their cooling dense ejecta. This process is associated with an intense phase of mass loss due to stellar winds, up to $10^{-4} M_{\odot} \text{ yr}^{-1}$ (Bowen & Willson 1991). They can dominate dust production as long as a burst of star formation took place at least 400 Myr prior to observations (Dwek et al. 2007; Valiante et al. 2009; Dwek & Cherchneff 2011). One AGB star is able to produce $10^{-5} - 10^{-2} M_{\odot}$ of dust (Morgan & Edmunds 2003; Ferrarotti & Gail 2006; Ventura et al. 2012; Nanni et al. 2013, 2014; Schneider et al. 2014).

Supernovae (SNe) are another stellar source of dust. Dust formation takes place in the expanding ejecta a few hundred or thousand days after the explosion, and stellar progenitors have initial masses of 8–40 M_{\odot} . Observations of SN1987A in the Large Magellanic Cloud have revealed that during such an event, up to 0.7 M_{\odot} of dust could be created (Matsuura et al. 2011). Similarly, a large amount of dust, $\sim 0.5 M_{\odot}$, has been reported for several supernovae (Gall et al. 2014; Owen & Barlow 2015; Bevan et al. 2017; De Looze et al. 2017; Temim et al. 2017; Rho et al. 2018; Chawner et al. 2019). This means that in the early galaxies a large amount of dust can be formed by SNe (e.g. Gall & Hjorth 2018). However, it is possible that SNe destroy most of the dust they form by reverse shock waves (Temim et al. 2015; Bianchi & Schneider 2007; Cherchneff & Dwek 2010; Gall et al. 2011c; Lakićević et al. 2015), but it is debated how much of the new and pre-existing dust is destroyed by a supernova as SN dust grains may be large and distributed in clumps (Gall et al. 2014; Lau et al. 2015; Wesson et al. 2015; Bevan & Barlow 2016; Micelotta et al. 2016; Gall & Hjorth 2018; Matsuura et al. 2019).

Dust grains formed by AGB stars and SNe can act as seeds that grow in the ISM, and this process can lead to a significant increase in the total dust mass (Draine & Salpeter 1979; Dwek & Scalo 1980; Dwek et al. 2007; Draine 2009). However, it is not clear if this process is efficient and quick enough, especially at high redshift. Ferrara et al. (2016) show that it is too slow in the diffuse ISM, and probably prohibited in molecular clouds because of icy mantles forming on the gas grains.

In this work we investigate a sample of galaxies at $6 < z < 8.4$ (900 – 600 Myr after the Big Bang) with the latest observational constraints on dust masses. Our aim is to test whether AGB stars or SNe are able to explain the observed amounts of dust in these galaxies, or whether dust accumulation must have also happened by a different (non-stellar) mechanism, for example grain growth in the ISM. We use a cosmological model with $H_0 = 70 \text{ km s}^{-1} \text{ Mpc}^{-1}$, $\Omega_{\Lambda} = 0.7$, and $\Omega_m = 0.3$.

2.2 Sample

We have selected all galaxies at $z > 6$ for which observations of dust continuum have been attempted, except those for which a similar method has already been applied: quasars J1048+4637, J1148+5251, and J2054-0005 (Michałowski et al. 2010b), and galaxies analysed in Michałowski (2015). We describe below the measurements used to estimate the dust and stellar masses needed for our analysis.

HATLAS J090045.4+004125 (hereafter HATLAS; Zavala et al. 2018) is one of a few submillimetre galaxies above $z = 6$ (together with that reported by Riechers et al.

2013). HATLAS was selected using the *Herschel* Space Observatory within the *Herschel* Astrophysical Terahertz Large Area Survey (Eales et al. 2010; Bourne et al. 2016; Valiante et al. 2016). Emission lines for $^{12}\text{CO}(6-5)$ and $^{12}\text{CO}(5-4)$ and the 1 mm continuum were detected by the Large Millimeter Telescope (Zavala et al. 2018). The mass of molecular gas was determined from the CO lines, whereas the dust mass was calculated in two ways: based on fitting photometric measurements to modified black-body function and via modelling using the MAGPHYS SED code (Table 2.1; Zavala et al. 2018). The dynamical mass was calculated using the isotropic virial estimator (equation 5 in Zavala et al. 2018).

Discovered with the Subaru telescope at redshift $z \sim 5.95$, HIMIKO was at that moment the most luminous $\text{Ly}\alpha$ emitter (Ouchi et al. 2009). Recent observations of this object using ALMA in band 6 revealed the presence of three clumps. From the [CII] detections the size of HIMIKO and the velocity linewidth were measured (Hirashita et al. 2017). The upper limit on the continuum emission of $S_{158\mu\text{m}} < 27 \mu\text{Jy}$ was also reported. This is deeper than the previous ALMA data for this galaxy reported in Ouchi et al. (2013).

Cosmos Redshift 7 (CR7) located at $z = 6.6$ is the most luminous $\text{Ly}\alpha$ emitter, discovered using the Subaru Telescope (Matthee et al. 2015; Sobral et al. 2015). From the ALMA [CII] line detection and dust continuum upper limit, Matthee et al. (2017) estimated the dynamical masses and dust masses found in two regions of this galaxy, Clump A and Clump C-2 (Table 2.1).

SPT-S J031132-5823.4 (SPT0311-58) was discovered using the South Pole Telescope (Mocanu et al. 2013), and confirmed at a redshift of 6.9 (Strandet et al. 2017). With high-resolution ALMA observations, Marrone et al. (2018) detected continuum, [CII] $158 \mu\text{m}$ and [OIII] $88 \mu\text{m}$ lines of two components of SPT0311-58, named East and West, and determined their gas and dust masses. Only for SPT0311-58 East was the stellar mass determined because no stellar emission was detected for the West component.

SXDF-N1006-2 was discovered during a survey for $\text{Ly}\alpha$ Emitters (LAEs) by the Subaru Telescope (Shibuya et al. 2012) and is located at $z = 7.2$. Inoue et al. (2016) used ALMA to detect the [OIII] $88 \mu\text{m}$ emission line and, assuming that the galaxy is a circular disk, determined its dynamical mass (Table 2.1). The upper limit on the continuum flux at band 6 (1.33 mm) of $< 0.042 \text{ mJy}$ was also obtained.

J1342+0928 is a quasar located at $z = 7.54$, first detected by Bañados et al. (2018). The detection of the [CII] $158 \mu\text{m}$ line emission allowed Venemans et al. (2017) to determine the dynamical mass of this galaxy based on the virial theorem, and the assumption that the [CII] emission comes from a rotating disk. From the detection of the 223.5 GHz continuum, the mass of dust in this galaxy was determined (Table 2.1). The limit on the molecular gas mass was derived from the observations of the CO(3-2) line (Table 2.1).

MACS0416_Y1 is one of the brightest Lyman Break Galaxies (LBGs) at $z \sim 8$ (Infante et al. 2015; Laporte et al. 2015). Using the detection of the [OIII] $88 \mu\text{m}$ line and the dust continuum, Tamura et al. (2019) confirmed its redshift as 8.3118, and measured its dust mass (assuming a dust temperature of 40 and 50 K). From the

optical emission the stellar mass was determined (Table 2.1). In our analysis, the lower error bar for the stellar mass was modified disregarding model solutions with ages lower than one million years (Y. Tamura, private communication).

A2744_YD4 at $z = 8.38$ is an LBG lensed by the Pandora Cluster. This object was observed in the Hubble Frontier Fields (HFF) by Zheng et al. (2014). The ALMA detection of the [OIII] $88 \mu\text{m}$ line allowed the confirmation of its redshift (Laporte et al. 2017). Based on the dust continuum detection and the optical emission, Laporte et al. (2017) estimated the mass of dust and stars in this galaxy (Table 2.1).

2.3 Method

We calculated the dynamical masses for galaxies with emission line detections for which this was not reported. This was the case for HIMIKO and SPT0311-58. Based on the detection of the [CII] emission line (Carniani et al. 2018; Marrone et al. 2018), the sizes of these galaxies were measured as $3.9 \pm 1.1 \times 1.7 \pm 1.1$ kpc for HIMIKO, 2.2 kpc for SPT0311-58E, and 7.5×2.0 kpc for SPT0311-58W. The [CII] linewidths were measured as 180 ± 50 kms^{-1} for HIMIKO, 500 kms^{-1} for SPT0311-58E, and 1000 kms^{-1} for SPT0311-58W. In order to calculate the dynamical masses we used eq. 5 in Zavala et al. (2018), based on the isotropic virial estimator. The results of these calculations are flagged in Table 2.1 with dagger symbols (\dagger).

Dust masses were not reported for HIMIKO and SXDF. We used the reported dust continuum upper limits to estimate the upper limits of the dust masses of these galaxies, assuming the dust temperature of 40 K and using eq. (5) in Michałowski et al. (2009), based on Taylor et al. (2005) and Hildebrand (1983). A value of the emissivity index of $\beta = 2$ was assumed. This gives conservatively low dust masses (see Fig. 3 in Michałowski et al. 2010a). In particular, if we adopted $\beta = 1.5$, then we would obtain dust masses 2.7 times higher, which would make the stellar dust producers even less likely. If we used this method for all galaxies, not only for those whose dust masses have not been calculated elsewhere, we would obtain masses a factor of 0.84 ± 0.33 higher. This would not change any of our conclusions. The results of our adopted dust mass calculations are flagged in Table 2.1 with dagger symbols (\dagger).

Using the same methodology as presented by Michałowski et al. (2010c) and Michałowski (2015), we determined the amount of dust that one star would have to produce in order to explain the observed amount of dust in every galaxy. The number of dust-producing stars was estimated from the stellar masses in the studied galaxies. The stellar masses were estimated in three ways: (1) as equal to M_{dyn} to obtain the maximum possible value, (2) as equal to $M_{dyn} - M_{gas}$, and (3) from SED modelling. The number of stars with masses between M_0 and M_1 can be calculated by the integration of the stellar initial mass function (IMF), according to the formula $N(M_0 - M_1) = M_{stellar} \int_{M_0}^{M_1} \xi(M) dM / \int_{M_{min}}^{M_{max}} \xi(M) M dM$, where $\xi(M)$ is an IMF parametrised as $M^{-\alpha}$. We assumed $M_{min} = 0.15$, $M_{max} = 120 M_{\odot}$, and three types of IMFs: the Salpeter (1955) IMF with $\alpha = 2.35$, the Kroupa (2001) IMF with $\alpha = 1.3$ in the mass range $0.15 - 0.5 M_{\odot}$ and $\alpha = 2.3$ in the mass range $0.5 - 120 M_{\odot}$, and a top-heavy IMF with $\alpha = 1.5$. The dust yield per star required to explain dust observed in a galaxy is then

Table 2.1: List of physical properties of the galaxies in our sample.

	z	M_{dgm} ($10^{10} M_{\odot}$)	M_{dust} ($10^7 M_{\odot}$)	M_{gas} ($10^{11} M_{\odot}$)	$M_{stellar}$ ($10^9 M_{\odot}$)	Ref	
HATLAS	6.027	2.6	19±4	42±7	0.16±0.06	—	1
HIMIKO	6.595	1.168 †	<0.16 †	—	—	35 ⁺¹⁵ ₋₂₆	2, 3
CR7	6.604	—	—	—	—	20	4
CR7 Clump A	6.601	3.9±1.7	<0.81	—	—	—	5
CR7 Clump C-2	6.598	2.4±1.9	<0.81	—	—	—	5
SPT0311-58E	6.9	7.7 †	40±20	0.4±0.2	—	35 ±15	6
SPT0311-58W	6.9	54.222 †	250±160	2.7±1.7	—	—	6
SXDF	7.2	5	<0.29 †	—	—	0.347 ^{+0.616} _{-0.166}	7
J1342+0928	7.54	<15	<3.2	24.5±18.5	<0.12	—	8
MACS0416_Y1	8.3118	—	0.36±0.07	0.82±0.16	—	4.8 ^{+6.8} _{-1.8} 5.1 ^{+7.1} _{-4.9}	9
A2744_YD4	8.38	—	—	0.55 ^{+1.96} _{-0.17}	—	1.97 ^{+1.45} _{-0.666}	10

† indicates the value determined in this work. (1) Zavala et al. (2018); (2) Carriani et al. (2018); (3) Ouchi et al. (2009); (4) Sobral et al. (2015); (5) Matthee et al. (2017); (6) Marrone et al. (2018); (7) Inoue et al. (2016); (8) Venemans et al. (2017); (9) Tamura et al. (2019); (10) Laporte et al. (2017).

$$M_{dust}/N(M_0 - M_1).$$

At the redshifts of the studied galaxies the time since the Big Bang was short, such that low-mass stars had not had time to leave the main sequence and start producing dust during the AGB phase. Based on a lifetime on the main sequence of $10^{10} \times [M/M_\odot]^{-2.5}$ (Kippenhahn & Weigert 1990), we assumed that at $z < 7.0$ only stars with masses between 3 to 8 M_\odot would have had time to enter the AGB phase, whereas at $z \geq 7.0$ the range of 3.5–8 M_\odot was assumed. For SNe we assumed that their progenitors had masses in the range of 8–40 M_\odot .

2.4 Results and discussion

Figure 2.1 shows the dust yield per star required to explain the dust mass for a given galaxy, using all possible combinations of dust and stellar masses. Galaxies considered elsewhere (Michałowski et al. 2010b; Michałowski 2015) are shown as grey symbols. The top and bottom panels assume that the dust is produced by SNe and AGB stars, respectively. Some regions have been highlighted. In the top panel are shown the theoretical dust yield per SN without dust destruction ($< 1.3 M_\odot$; Todini & Ferrara 2001; Nozawa et al. 2003) and with $\sim 90\%$ dust destruction ($< 0.1 M_\odot$; Bianchi & Schneider 2007; Cherchneff & Dwek 2010; Gall et al. 2011c; Lakićević et al. 2015). We note that it is difficult to constrain the fraction of newly formed dust destroyed by a reverse shock (Micelotta et al. 2016), so a weaker dust destruction is also possible. In the bottom panel the maximum theoretical dust yield per AGB star is shown ($0.04 M_\odot$; Morgan & Edmunds 2003; Ferrarotti & Gail 2006; Ventura et al. 2012; Nanni et al. 2013, 2014; Schneider et al. 2014).

Depending on the data available, the stellar mass was obtained in various ways: as $M_{dyn}-M_{gas}$, as M_{dyn} , and from SED modelling. Only for one object, SPT0311-58E, was it possible to determine the required dust yield per star with the three different assumptions on stellar mass, and they do not differ from each other by more than their uncertainties. For this galaxy the required dust yield per SN is about $0.1-1 M_\odot$. This is close to the maximum dust yield predicted by simulations and to the highest observed values. Therefore, it is in principle possible that dust in this galaxy was formed by SNe, but that would require weak dust destruction and very efficient production. We cannot accept a similar conclusion for AGB stars. One AGB star would need to create between 0.1 to $1 M_\odot$ of dust to explain the dust mass in SPT0311-58E, which is significantly higher than the allowed values.

The dust yield per SN required to explain dust in the HATLAS galaxy is close to $1 M_\odot$, so if they are responsible for the bulk of the dust production, then they would need to be maximally efficient and not to destroy any dust. AGB stars cannot be responsible for the dust production in this galaxy because the required dust yield per star is more than 10 times higher than the theoretical value.

In the case of galaxies SPT0311-58W, J1342+0928, and A2744_YD4 it is possible that SNe are responsible for the observed dust. Some dust destruction, but not a significant amount, by SNe would be allowed in these cases as the derived dust yields are above $0.1 M_\odot$. This is in line with the result of Gall & Hjorth (2018) that dust

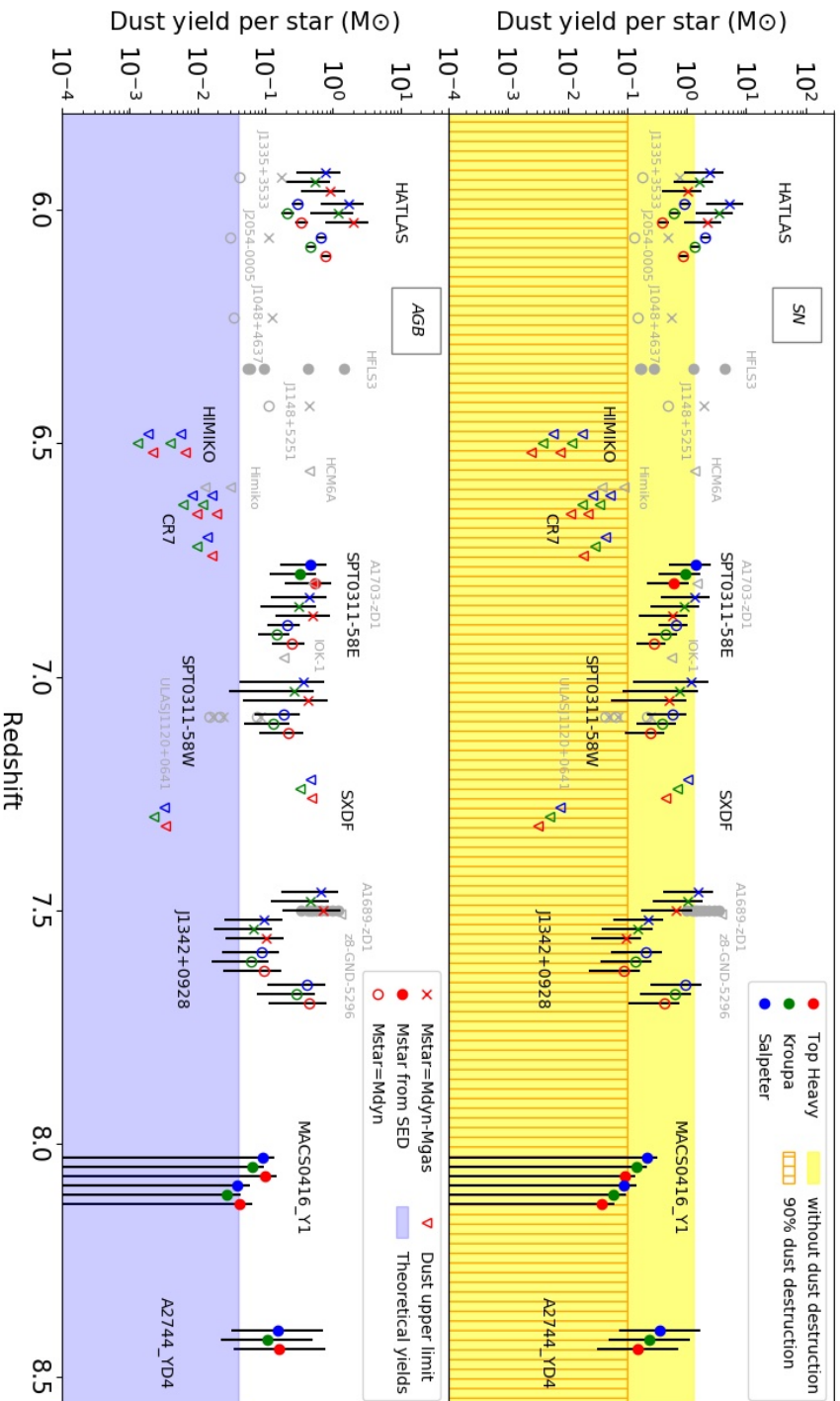


Figure 2.1: Dust yield per SN (top) and AGB star (bottom) required to explain the dust masses in galaxies in our sample. Three forms of the initial mass function are assumed: top-heavy (red), Kroupa (green), and Salpeter (blue). The stellar mass was determined in various ways: M_{dyn} - M_{gas} (cross), M_{dyn} (open circle), and SED modelling (filled circle). In addition, galaxies with upper limits of dust masses are indicated by down-pointing triangles. Multiple points with the same shape and colour for a galaxy are for different dust or stellar mass estimates. Galaxies considered elsewhere (Michalowski et al. 2010b; Michalowski 2015) are shown as grey symbols. For SNe two regions have been defined: below the maximum theoretical dust yield without dust destruction of $1.3M_{\odot}$ (yellow) and below the limit of $0.1M_{\odot}$ including $\sim 90\%$ dust destruction (vertical orange stripes). For AGB stars the theoretically allowed dust yields are indicated (light blue).

in distant galaxies (including A2744_YD4) was formed by SNe, which requires very little dust destruction. Again, the required dust yields per AGB star for these three galaxies are significantly above the theoretical limit, so AGB stars have not contributed substantially to the dust production in these galaxies.

For the remaining four galaxies in our sample the data are of insufficient quality to constrain the dust production mechanism. HIMIKO, CR7, and SXDF only have upper limits for the mass of dust, so we cannot rule out either SNe or AGB stars as dust producers. We can only conclude that one SN in these galaxies could not produce more than $0.01M_{\odot}$ of dust. This indicates that SNe in the early Universe are much less efficient than the maximum theoretical values, and casts doubts on the efficient SN dust production in the remaining galaxies in our sample (see also Hirashita et al. 2014). Our limit is two times deeper than that obtained by Hirashita et al. (2014) because we used stellar masses that are two times higher. For the last galaxy, MACS0416_Y1, we also cannot rule out the dust production mechanism because the large uncertainty on the measurement of its stellar mass results in a derived dust yield consistent with zero.

In summary, AGB stars were not able to form dust in the majority of $z > 6$ galaxies. Our results are conservative (leading to low required dust yields) because we include all stars that in principle could contribute to dust production. Stars with the masses close to our AGB lower limit (3 or $3.5 M_{\odot}$) could have reached the AGB phase, but only if they were all born at the beginning of the galaxy evolution.

Supernovae would need to be maximally efficient and not to destroy the dust they formed (as in Hjorth et al. 2014; Gall & Hjorth 2018). One of the recent observations of SN 1987A indicates that dust can re-form and re-grow in post-shock region after being destroyed by the shock (Matsuura et al. 2019, but see Biscaro & Cherchneff 2014). This is consistent with high dust production efficiency of SNe. Similarly, the detection of SN dust in a 10 000 year old SN remnant (Lau et al. 2015; Chawner et al. 2019) indicates that dust is not efficiently destroyed by SNe.

It is unclear, however, whether all SNe can produce close to $1 M_{\odot}$ of dust. If this is not the case, then some non-stellar mechanism is required, for example grain growth in the ISM. Asano et al. (2013) found that dust mass accumulation is dominated by the grain growth in the ISM if the metallicity is higher than a threshold value of 0.3 solar metallicity (or less if the star formation timescale is longer). This is likely for very dusty galaxies in our sample (HATLAS, SPT0311-58, J1342+0928), but more normal galaxies (MACS0416_Y1, A2744_YD4) may have lower metallicities. However, for A2744_YD4 we derived very high required dust yields per star, so either its metallicity is above this threshold or grain growth is always efficient below it.

We consider AGB stars and SNe separately, but in reality both contribute to dust production at the same time. However, this does not affect our conclusions because for the detected galaxies the required dust yields for AGB stars are approximately ten times higher than the allowed value. This means that AGB stars could produce at most 10% of the dust in these galaxies, and thus considering AGB stars and SNe at the same time would lead to revising down the required dust yield per SN by only 10%.

The question remains of the source of heavy elements building the dust grains in these galaxies. Theoretical work has shown that each SN can produce around $1 M_{\odot}$

of heavy elements (Todini & Ferrara 2001; Nozawa et al. 2003; Bianchi & Schneider 2007; Cherchneff & Dwek 2009). This is close to the required dust yields per SN in our sample, so, as do Michałowski et al. (2010b), we conclude that SNe are efficient enough to produce heavy elements needed to build dust grains in these galaxies, even if they do not directly form most of the dust.

2.5 Conclusions

We determined the dust yield per AGB star and SN required to explain the observed amount of dust in galaxies at redshift $6 < z < 8.4$. We obtained very high required dust yields per AGB stars, so they were not able to produce the majority of the dust in these galaxies. In most cases we accepted the hypothesis about the formation of dust by SNe, but they would need to be maximally efficient and not to destroy much dust. This suggests either that supernovae were efficient in producing dust in these galaxies or that a non-stellar mechanism was responsible for a significant fraction of dust mass accumulation, for example grain growth in the ISM.

2.6 PhD candidate contribution

In this publication, I was responsible for collecting the entire sample, calculating all required parameters for the analysis, performing required calculations, presenting the results in the figure and table, and preparing the text of this publication, after discussions with the supervisor.

Chapter 3

Observational evidence for morphological quenching in early-type galaxies

The following Chapter published as Leńniewska et al. 2023, *The Fate of the Interstellar Medium in Early-type Galaxies. II. Observational Evidence for Morphological Quenching*, ApJ, 953, 27.

Abstract

The mechanism by which galaxies stop forming stars and get rid of their interstellar medium (ISM) remains elusive. Here, we study a sample of more than two thousand elliptical galaxies in which dust emission has been detected. This is the largest sample of such galaxies ever analysed. We infer the timescale for removal of dust in these galaxies and investigate its dependency on physical and environmental properties. We obtain a dust removal timescale in elliptical galaxies of $\tau = 2.26 \pm 0.18$ Gyr, corresponding to a half-life time of 1.57 ± 0.12 Gyr. This timescale does not depend on environment, stellar mass or redshift. We observe a departure of dusty elliptical galaxies from the star formation rate vs. dust mass relation. This is caused by the star-formation rates declining faster than the dust masses and indicates that there exists an internal mechanism, which affects star formation, but leaves the ISM intact. Morphological quenching together with ionisation or outflows caused by older stellar populations (supernova type Ia or planetary nebulae) are consistent with these observations.

3.1 Introduction

Dust influences the evolution of galaxies by acting as catalyst of molecule formation and providing shielding from interstellar radiation. Its emission can also be used as a diagnostic for interstellar medium (ISM) properties (Scoville et al. 2016). There are several processes that can contribute to dust removal from galaxies. Dust can be incorporated in newly formed stars (astration; Gall & Hjorth 2018), or destroyed by active galactic nucleus (AGN) feedback (Fabian 2012). Supernovae (SNe) may destroy newly-formed and pre-existing dust by forward and reverse shock waves (Temim et al.

2015; Bianchi & Schneider 2007; Cherchneff & Dwek 2010; Gall et al. 2011b; Lakićević et al. 2015). Dust can be also destroyed by planetary nebulae. This is due to heating of gas by shocks from colliding planetary nebulae (Conroy et al. 2015). Galactic outflows contribute to dust removal and can be very effective due to radiation pressure-driven dusty flows (Bianchi & Ferrara 2005). Hot gas ($\sim 10^5$ K) present in some regions of ISM can also cause erosion of dust particles. The smallest grains are the most vulnerable to this mechanism (Bocchio et al. 2012).

Over the past decades, many theoretical works have been developed to model the formation, evolution and destruction of dust in galaxies. Among the first research dealing with dust evolution is Dwek & Scalo (1980), who emphasized the importance of SNe. Barlow (1978) studied sputtering of dust grains in HII regions, inter-cloud medium, cloud-cloud collisions shock waves, and SN remnants, concluding that the latter dominates this process. Gall et al. (2011b) developed a numerical model of galactic chemical evolution and studied the effect of galaxy properties on the evolution of dust. Dust destruction was described in the model as being caused by SN shocks. The tested properties of dust evolution depend very strongly on the initial mass function. Slavin et al. (2015) focused on dust destruction by SNe, which resulted in a dust removal timescale of 2–3 Gyr.

Recent studies of high-redshift ($z \sim 1.6$ – 3.3) lensed quiescent galaxies have shown that their dust-to-stellar mass ratios are of order 10^{-4} (Whitaker et al. 2021). Similarly, Blázquez-Sesé et al. (2023) showed that high-redshift galaxies are characterized by an order of magnitude higher gas fractions than what is detected in the local Universe.

In order to separate the processes of dust formation and removal, it is an advantage to study galaxies with little dust formation, but with detectable ISM. Therefore, dusty early-type galaxies (ETG; ellipticals and lenticulars) form a suitable sample for such endeavour. The dust emission of only several dozen of such galaxies has been analysed (Smith et al. 2012; Rowlands et al. 2012; Agius et al. 2013, 2015; di Serego Alighieri et al. 2013; Hjorth et al. 2014; Dariush et al. 2016; Michałowski et al. 2019a; Magdis et al. 2021). Hjorth et al. (2014) showed that dusty early-type galaxies do not follow the relation between the star formation rates (SFRs) and dust masses (da Cunha et al. 2010) and discussed formation or quenching scenarios. (Michałowski et al. 2019a, submitted 2023) revealed an exponential decline of the dust-to-stellar and gas-to-stellar mass ratios with galaxy age and measured the timescale of this process to be 2.5 ± 0.4 Gyr. To date, this is the only measurement of the dust removal timescale in dusty early-type galaxies and is based on a sample of 61 galaxies.

Dusty elliptical galaxies are quite rare. Hence, far-infrared/submillimeter surveys need to cover a large area to detect a high number of galaxies to build a significant sample. The ESA *Herschel Space Observatory* (henceforth *Herschel*, Pilbratt et al. 2010) has provided deep infrared observations of hundreds of square degrees of the sky. Its large field of view, $4' \times 8'$, and sensitivity has led to the detection of dust in millions of galaxies.

One of the major cosmological and galaxy evolution observation projects, Galaxy And Mass Assembly (GAMA; Driver et al. 2011, 2016; Baldry et al. 2018; Smith et al.

2011¹), brings together the latest generation of instruments and surveys, such as the Anglo-Australian Telescope (AAT), Sloan Digital Sky Survey (SDSS), and *Herschel*. These datasets were combined in a database of several hundred thousand galaxies, with a magnitude limit in the r band of 19.8 mag. Such an extensive catalog not only allows the examination of the relationships between individual quantities, but also gives the possibility of additional sampling into bins of various parameters.

In this paper we study a large sample of more than two thousand elliptical galaxies in which dust was detected. The sample size allows us to investigate dust evolution as a function of various galaxy properties. We focus on relationships between their physical and environmental parameters. The objective of this paper is to distinguish the mechanisms contributing to the removal of dust in elliptical galaxies and investigate its dependency on physical and environmental properties.

We use a cosmological model with $H_0 = 70 \text{ km s}^{-1} \text{ Mpc}^{-1}$, $\Omega_\Lambda = 0.7$, and $\Omega_m = 0.3$. We assume the Chabrier (2003b) initial mass function.

3.2 Data and Sample

3.2.1 GAMA Catalog

Herschel covered an area of 161.6 deg² of the GAMA fields and provided information on dust emission at 250, 350, and 500 μm . The GAMA catalog for these fields contains properties of 120,114 galaxies based on modeling of spectral energy distributions with the Multi-wavelength Analysis of Galaxy Physical Properties (MAGPHYS; da Cunha et al. 2008). This includes dust masses, stellar masses, star formation rates, and luminosity-weighted stellar ages. The values of these parameters were obtained by the GAMA project and are presented in their MagPhys catalogue². We also obtained a wide range of parameters related to photometry, a single-Sérsic fit to SDSS 2D surface brightness distribution (Kelvin et al. 2012) and local environment of galaxies such as surface galaxy density (Σ) calculated based on the distance to the fifth nearest neighbour within a velocity difference of $\pm 1000 \text{ km s}^{-1}$ (Brough et al. 2013).

3.2.2 Sample

We used the r -band Sérsic index (Sérsic 1963), n , to select elliptical galaxies by requiring that $n > 4$. This resulted in 22,571 galaxies.

From this set of galaxies we selected dusty ellipticals with a minimum signal-to-noise ratio at the *Herschel* SPIRE (Griffin et al. 2010) 250 μm filter of 3. This step resulted in 2,956 galaxies, so 13% of elliptical galaxies are detected by *Herschel*. This is higher than the detection rate of 5.5% obtained by Rowlands et al. (2012) for similar galaxies, who required a higher significance of 5σ at 250 μm .

¹<http://www.gama-survey.org>

²<http://www.gama-survey.org/dr3/data/cat/MagPhys/>

Rowlands et al. (2012) visually classified galaxies to the early-type category at redshifts $0.01 < z < 0.32$. We selected galaxies in the same redshift range. At higher redshifts the morphological classification is uncertain (de Albernaz Ferreira & Ferrari 2018) and the sample could contain compact high star-forming (not elliptical) galaxies. Our final selection, including the redshift cut, resulted in 2050 galaxies. Our selection roughly corresponds to a flux-limited sample above 20.7 mJy at the SPIRE 250 μm , although adopting that limit would result in 17% of galaxies having a signal-to-noise ratio less than 3. Selection of galaxies based on SPIRE 250 μm flux > 20.7 mJy does not affect our results.

The uncertainties of the physical properties are the following, measured separately for MS and below-MS subsamples: 0.12–0.14 dex for stellar age, 0.1–0.3 dex for SFR, 0.15–0.22 dex for M_{dust} , 0.1 dex for $M_{stellar}$, where the higher values correspond to the galaxies below the main sequence.

Rowlands et al. (2012) estimated that 2% of dusty early-type galaxies in their sample are likely chance projections of a dust-free galaxy and a background dusty galaxy. Our selection criteria are similar: we used the updated GAMA archive (DR3), Sérsic index > 4 instead of visual classification, and the same redshift range, so we expect a similar fraction, which does not affect our analysis. The main difference is the area over which the galaxies were selected, resulting in a much larger sample of 2050 objects as compared to the 44 galaxies studied in Rowlands et al. (2012).

3.3 Results

3.3.1 Main Sequence

We divided the selected galaxies into two groups: galaxies within and below the main sequence (MS) of star forming galaxies. Fig. 3.1 (top) presents a comparison of our galaxies with a redshift-dependent MS as measured by Speagle et al. (2014, eq. 28). We adopted a measured MS width of 0.2 dex (Speagle et al. 2014), independent of redshift. Any galaxy below the MS by more than 0.2 dex is assigned to the ‘below-MS’ group in this paper. Our sample covers the redshift range uniformly with a sensitivity < 100 times below the MS at all redshifts. This resulted in 722 MS dusty elliptical galaxies and 1328 below-MS galaxies.

We tested the validity of the Speagle MS for our data using late-type galaxies from GAMA, which have been selected based on Sérsic index < 2.5 , $0.1 < z < 0.15$, and $S/N > 3$ at S250. We find an agreement between the Speagle MS and the MS estimated using the selected LTGs, in particular in the stellar mass range covered by our ETG sample.

3.3.2 Dust Removal Timescale

Figure 3.1 presents dust-to-stellar mass ratio as a function of luminosity-weighted stellar age (middle panel). There is an evident decline in the mass ratio as galaxies

evolve over time. Fitting an exponential function to this plane, as in Michałowski et al. (2019a), allows us to evaluate the timescale of the dust mass removal for different galaxy properties:

$$\frac{M_{dust}}{M_*} = A \cdot e^{-age/\tau}, \quad (3.1)$$

where A is the normalisation constant and τ is the dust removal timescale. We obtained a dust removal timescale for all elliptical galaxies of $\tau = 2.26 \pm 0.18$ Gyr with the corresponding half-life time of 1.57 ± 0.12 Gyr. The values of the dust removal timescale, half-life time and the normalisation constant are presented in Table 4.1. To our knowledge, this is the first determination of the dust removal timescale for such a large sample and for different galaxy properties.

We also fit the exponential function separately to galaxies on and below the MS. The elliptical galaxies below the MS (red line) follow the fit obtained by (Michałowski et al. 2019a, lime green line), whereas the elliptical galaxies on the MS (blue line) are characterized by a faster dust mass decline. The results of our fitting are given in Table 4.1.

One of the basic parameters which is useful for subdivision into smaller bins is stellar mass, because galaxies of different masses may evolve differently. The three top panels in Fig. 3.2 show the dust-to-stellar mass ratio as a function of age for three stellar mass bins between $10 < \log(M_{\text{stellar}}/M_{\odot}) < 11.5$, with a 0.5 dex width. The fits for these stellar mass bins are consistent with each other within the error bars (Table 4.1). Therefore, we conclude that the dust mass decline with time does not depend on stellar mass in the analysed range.

The most massive group with $11.5 < \log(M_{\text{stellar}}/M_{\odot}) < 12.2$, does not contain MS galaxies, and includes only galaxies with high ages and low dust-to-stellar mass ratios. It is not possible to fit an exponential function to the galaxies in this group because the dynamical range of both properties is too small. However, these galaxies are still consistent with the fitted dust removal function obtained for galaxies at lower masses.

Other galaxies in the close proximity of elliptical galaxies can affect their ISM. Therefore, we studied the role of the galaxy environment. The GAMA catalog provides surface galaxy density, Σ , in the G15 field for galaxies at $z < 0.18$ (Brough et al. 2013). There are 384 of our dusty ETGs satisfying these criteria and for 373 of them (97%) Σ has been measured. The dust decline as a function of age in bins of Σ is presented in Fig. 3.2 (middle row). It is evident that the decline in dust mass is independent of the galaxy environment. We reached the same conclusion when we analysed the effect of environment in narrower ranges of stellar mass.

Our sample spans a redshift range 0.01–0.32, corresponding to 3.6 Gyr of the evolution of the Universe. Fig. 3.2 (bottom) shows that the dust removal does not depend on redshift, as galaxies follow the same dust removal trend at each redshift bin.

3.3.3 Dust Masses vs Star Formation Rates

Figure 3.1 (bottom) presents the SFR- M_{dust} relation for our 2050 dusty elliptical galaxies. It is evident that our MS elliptical galaxies follow the da Cunha et al. (2010)

relation (black line). Hence for MS elliptical galaxies the decrease in SFR is accompanied by a similar decrease in the dust mass, so they stay on the relation. However, as first shown by Hjorth et al. (2014), elliptical galaxies below the MS are found above the da Cunha et al. (2010) relation with higher dust masses than what their SFRs imply.

3.3.4 Central Surface Luminosity

From the GAMA light profile catalog we used the values of the central surface brightness and converted them to central surface luminosities (luminosity per kpc^2). We find that the decrease of dust mass with the age of the elliptical galaxies does not depend on the central surface luminosity.

3.3.5 Quenching

To study the evolution of dusty elliptical galaxies, we divided our sample into eight bins of stellar age. Figure 3.3 (top) presents SFR vs. stellar mass with the addition of the median values in age bins, separately for the MS and below-MS elliptical galaxies. These medians are presented in Table 4.2 in the Appendix. The medians of SFRs and stellar masses of MS elliptical galaxies are (as expected) close to the MS. For elliptical galaxies below the MS, with increasing age the medians move away from the MS toward lower SFRs. The youngest below-MS elliptical galaxies are ~ 0.6 dex below the MS and the oldest have more than 10 times lower SFRs than the youngest.

Figure 3.3 (bottom) presents dust mass vs. SFR with the medians in age bins for the MS and below-MS elliptical galaxies (Table 4.2). The medians for MS ellipticals are located close to each other and to the da Cunha et al. (2010) relation (black line), with no clear evolution. Elliptical galaxies below the MS have higher dust masses for their SFRs than what the da Cunha et al. (2010) relation implies. We fitted a power-law function to the medians of the galaxies below the MS (red line), resulting in $\log(M_{dust}) = (0.55^{+0.10}_{-0.11}) \cdot \log(\text{SFR}) + (7.893^{+0.030}_{-0.031})$. This is shallower than the slope of the da Cunha et al. (2010) relation of 1.1.

From Fig. 3.3 (bottom) it is evident that the elliptical galaxies below the MS move away from the da Cunha et al. (2010) relation as they are getting older. The youngest of the below-MS galaxies have SFRs around $1 M_{\odot} \text{ yr}^{-1}$ and dust masses around $10^{7.9} M_{\odot}$ (0.8 dex above the relation). With increasing age, their SFRs decrease faster than their dust masses. This results in the oldest galaxies having SFR around $0.1 M_{\odot} \text{ yr}^{-1}$ (a factor of 10 decrease) and dust mass of $10^{7.3} M_{\odot}$ (a factor of 4 decrease), placing them 1.3 dex above the relation.

3.3.6 Sample Evaluation

To ensure that our selection is robust, we studied a subsample of galaxies with at least two detections among 5 *Herschel* bands ($\text{S/N} > 3$). This resulted in 1430 galaxies. The exponential curve fitting gives the same results as the original sample within the

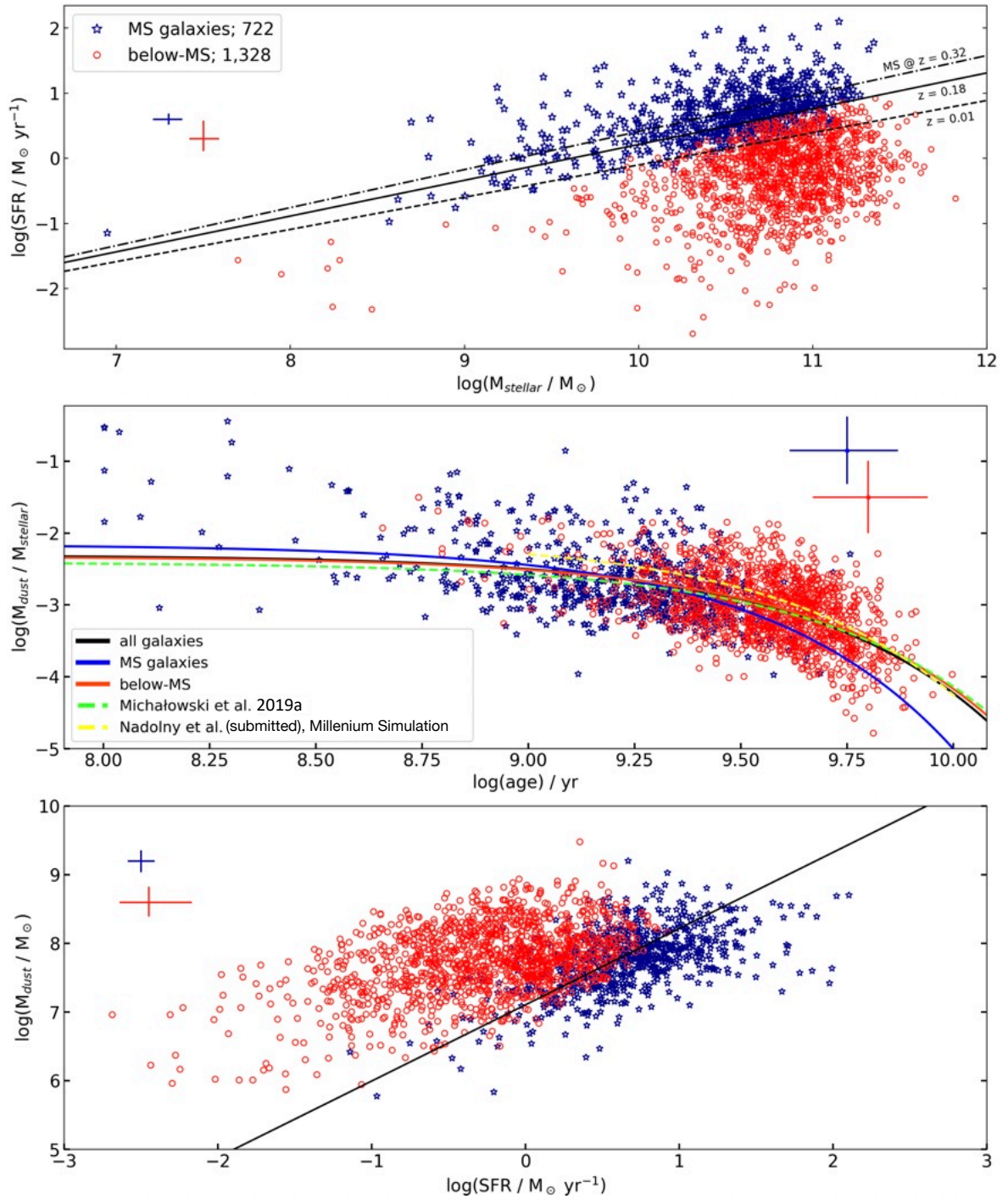


Figure 3.1: (Top) SFR as a function of stellar mass. Color coding distinguishes MS galaxies (blue stars) and galaxies below the MS (red circles). The star formation main sequence at $z = 0.32$, 0.18 , and 0.01 (black lines) based on Speagle et al. (2014) are shown. The numbers of selected MS and below-MS galaxies are presented in the legend. (Middle) Dust-to-stellar mass ratio as a function of stellar age. The exponential fits are for galaxies within the MS (blue line), galaxies below the MS (red line), all galaxies (black line), that obtained by Michałowski et al. (2019a) (lime green dashed line), and by Nadolny et al. (submitted) with the Millenium Simulation (yellow dashed line) within the age range 9.0– 10.1 Gyr. (Bottom) Dust mass as a function of SFR with the da Cunha et al. (2010) relation (black line). Median errorbars for the MS and below-MS galaxies are shown as blue and red crosses, respectively.

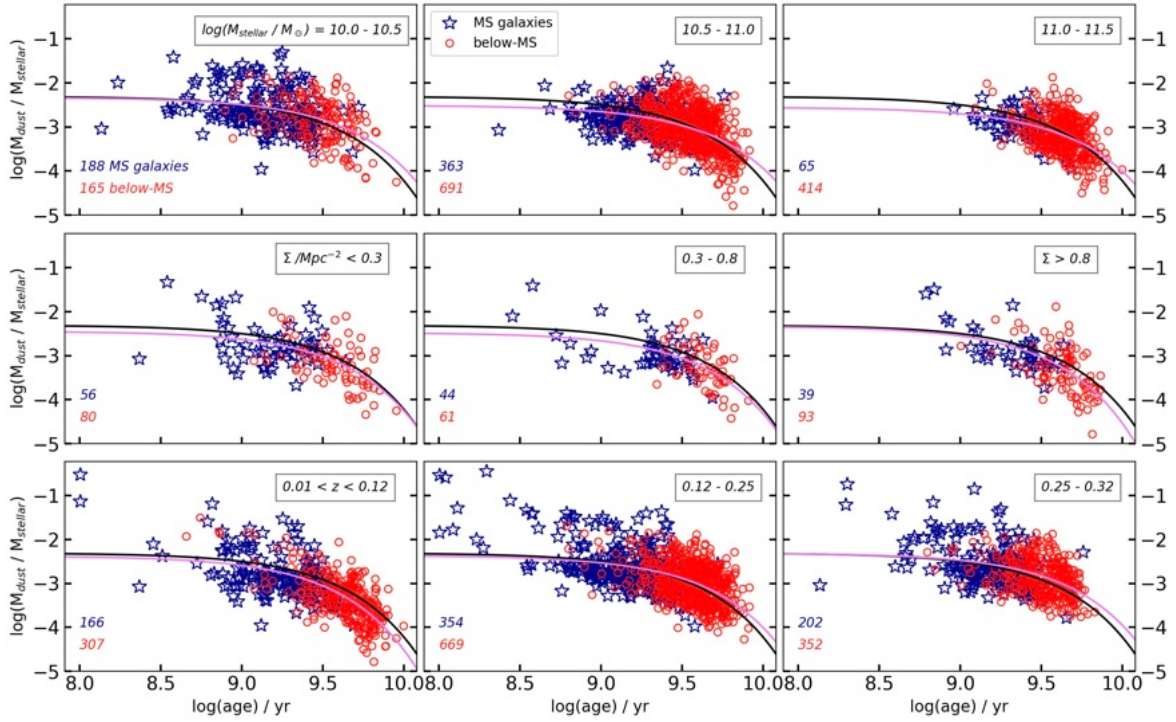


Figure 3.2: Dust-to-stellar mass ratio as a function of stellar age and other galaxy properties. The MS galaxies are marked as blue stars and galaxies below the MS are marked as red open circles. The numbers of selected MS and below-MS galaxies in each panel are shown. The exponential fits are for all 2050 studied galaxies (black line) and for galaxies plotted on individual panel (violet line). The division into three stellar mass bins (top row), galaxy surface density based on the distance to the 5th nearest neighbour (middle row), and redshift (bottom row) are shown.

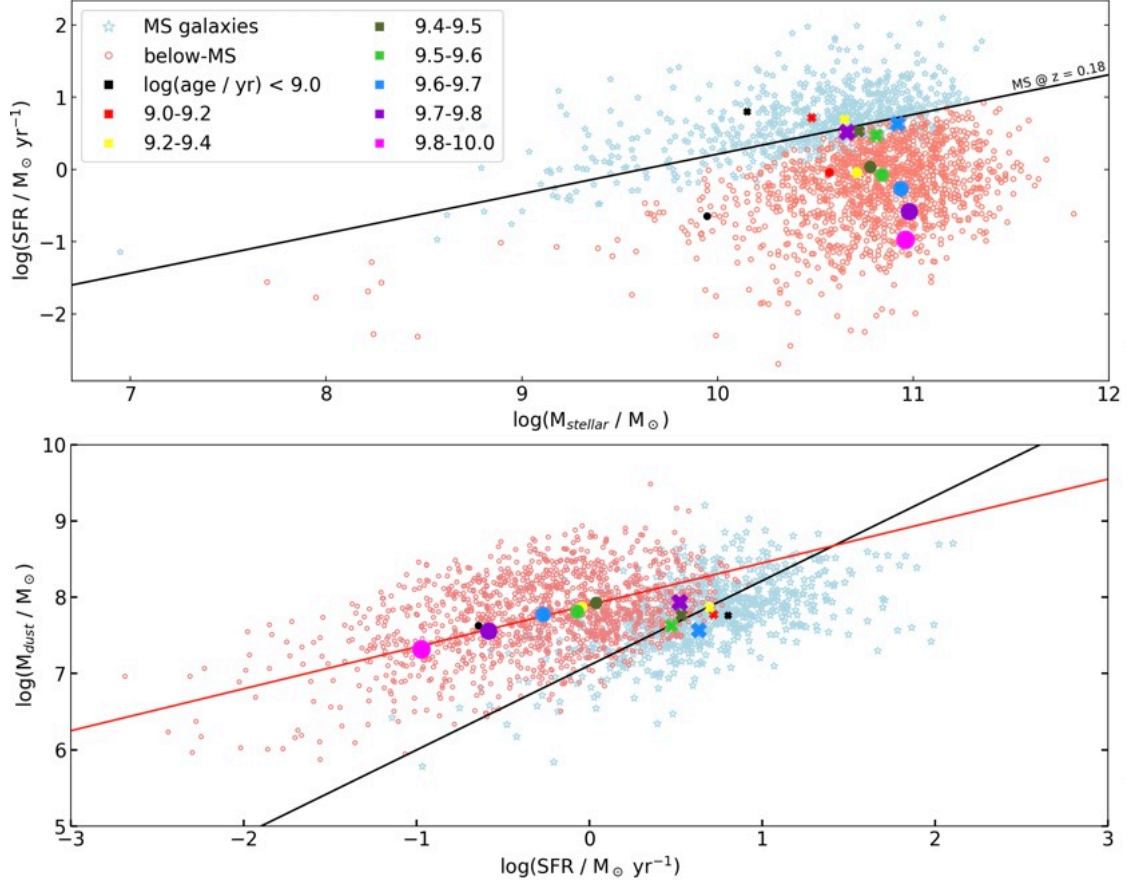


Figure 3.3: SFR as a function of stellar mass (top) and dust mass as a function of SFR (bottom). Color coding distinguishes MS galaxies (blue stars) and galaxies below the MS (red circles). The star formation main sequence at $z = 0.18$ based on Speagle et al. (2014) and the da Cunha et al. (2010) relation are shown (black lines). The median values of SFR, stellar age, and dust mass for eight galaxy age ranges are marked as filled crosses for the MS galaxies, and as filled circles for galaxies below the MS. In addition to the color-coding, the size of the symbol increases with age. The red line shows a power-law fit to the median values of the galaxies below the MS in a form $\log(M_{\text{dust}}) = (0.55^{+0.10}_{-0.11}) \cdot \log(\text{SFR}) + (7.893^{+0.030}_{-0.031})$.

error limits of these parameters. This shows that increasing the number of required band detections does not change our results and conclusions.

In order to check the correctness of the stellar ages calculated by the GAMA project, we analyzed average spectral energy distribution (SED) for eight stellar age bins defined in previous section. There is a clear correlation between the bin age and the relative normalised (in the near-infrared) flux. The oldest bin shows lower flux at the blue part of the SED, while the youngest bin shows the most prominent blue part of the SED that corresponds to the young stellar population of massive and hot OB stars. Normalisation in the near-infrared (equivalent to a stellar mass normalisation, as considered above), gives a clear luminosity decrease in the far-infrared with increasing age, equivalent to the dust-to-stellar decrease.

The GAMA project database also contains information about the D4000 break (Cardiel et al. 1998; Balogh et al. 1999). The strength of this break as a function of luminosity-weighted age for the below-MS galaxies from our sample shows that older galaxies have higher D4000, consistent with the determined age of the galaxies. The Spearman's rank correlation is 0.47 and the probability of the null hypothesis of no correlation is 10^{-70} .

3.4 Discussion

Our key result is the confirmation of the exponential decrease of the dust mass with age using unprecedentedly large sample. We also found that SFRs of dusty ellipticals below the MS decline faster with age than their dust masses and the dust mass decline is independent of stellar mass, environment, redshift and central surface luminosity. As suggested by Hjorth et al. (2014) and Michałowski et al. (2019a, 2024), morphological quenching is a potential mechanism for departing from the da Cunha et al. (2010) relation. This is consistent with our findings. The process may be responsible for the gravitational stability that stops the collapse of gas clouds, resulting in a slower rate of star formation. At the same time, the process does not change the amount of gas, which means that the dust mass observed in these galaxies does not decrease proportionally with the SFR. Other processes must be responsible for the decline of the dust masses, e.g., the destruction of dust by feedback from older stellar populations (see Michałowski et al. (2024)). This includes SNe Type Ia (Li et al. 2020) or planetary nebulae (Conroy et al. 2015).

AGN feedback is also one of the potential mechanism of the ISM removal (Fabian 2012). Recent studies suggest that quenching is connected with integrated AGN feedback over the lifetime of a galaxy, which is correlated with the supermassive black hole mass, not the instantaneous AGN luminosity (Bluck et al. 2020b,a, 2022, 2023; Piotrowska et al. 2022). This mass is correlated with the bulge mass (Magorrian et al. 1998; Häring & Rix 2004), which can be approximated by the galaxy central surface luminosity. We did not detect any dependence on the dust decline on this parameter (Section 3.3.4), which suggests that integrated AGN feedback is not a dominating mechanism of the dust removal. This is because if the integrated feedback was responsible for the dust removal in our galaxies then galaxies with higher central surface

luminosities (more massive black holes and therefore stronger feedback) would exhibit a faster ISM decline. This finding is consistent with our study of the Baldwin, Phillips, & Terlevich (1981, BPT) diagram which shows that only up to 15% of galaxies in our sample host AGNs, which means that they cannot have any significant effect on reducing the dust amount in these galaxies (Ryzhov et al. in prep.).

We did not find any redshift dependency or environmental influence on dust removal, which is inconsistent with external mechanisms of dust removal. The dust removal also does not depend on the stellar mass [in the explored range of $\log(M_{\text{stellar}}/M_{\odot}) = 10\text{--}11.5$], so the process linearly scales with mass (a bigger galaxy has proportionally more dust and proportionally more efficient dust removal).

We note that the lack of the below-MS elliptical galaxies at or even below the SFR- M_{dust} relation is not due to a detection limit at M_{dust} . It is $10^{5.2} M_{\odot}$ at $z = 0.05$ and $10^{6.7} M_{\odot}$ at $z = 0.3$ (Michałowski et al. 2019a), so if such galaxies existed, they would be detected.

3.5 Conclusions

We analysed ISM and stellar properties of 2050 dusty elliptical galaxies which has never been done before on such a large sample. Our findings support the morphological quenching as a mechanism behind their SFR decline, as proposed by Hjorth et al. (2014). This is because the galaxies below the MS do not follow the da Cunha et al. (2010) SFR- M_{dust} relation, having higher dust masses for a given SFR. We also found that they evolve away from this relation as they age, with SFRs decreasing faster than dust masses.

We obtained a dust removal timescale for dusty elliptical galaxies of 2.26 ± 0.18 Gyr, which is consistent with the value of 2.5 ± 0.4 Gyr found by Michałowski et al. (2019a). The dust mass decline does not depend on stellar mass, implying a linear scaling of this effect with galaxy mass. Moreover there is no dependence of the decrease in dust mass on the galaxy environment or redshift, so the dust mass decline is of an internal nature. The independence of the dust decline on the central surface luminosity (a proxy for integrated black hole activity) suggests that AGN feedback is not responsible for the ISM decline.

3.6 PhD candidate contribution

In this publication, I was responsible for collecting and combining several tables from the GAMA database in order to obtain the final sample, selecting galaxies for the final analysis, performing required calculations and fittings, presenting the results in all figures and tables, and preparing the text of this publication, after discussions with other co-authors.

Appendix

A. Numerical values from figures

Table 3.1: Dust removal timescale τ , half life-times, and normalisations from fitting exponential functions to the middle panel of Figure 3.1 and all panels from Figure 3.2.

	τ [Gyr]	$\tau_{1/2}$ [Gyr]	A
MS galaxies	1.53 ± 0.22	1.06 ± 0.15	-2.16 ± 0.04
below-MS	2.36 ± 0.22	1.64 ± 0.15	-2.33 ± 0.03
all galaxies	2.26 ± 0.18	1.57 ± 0.12	-2.31 ± 0.02
$\log(M_{\text{stellar}}/M_{\odot})$			
10.0 – 10.5	2.71 ± 0.72	1.88 ± 0.50	-2.34 ± 0.05
10.5 – 11.0	3.03 ± 0.40	2.10 ± 0.27	-2.51 ± 0.03
11.0 – 11.5	2.98 ± 0.59	2.07 ± 0.41	-2.56 ± 0.05
Σ/Mpc^{-2}			
< 0.3	2.40 ± 0.81	1.66 ± 0.56	-2.45 ± 0.08
0.3 – 0.8	2.36 ± 0.87	1.63 ± 0.60	-2.48 ± 0.10
> 0.8	1.97 ± 0.57	1.36 ± 0.40	-2.33 ± 0.11
z			
0.01 – 0.12	2.02 ± 0.28	1.40 ± 0.19	-2.38 ± 0.05
0.12 – 0.25	2.64 ± 0.33	1.83 ± 0.23	-2.37 ± 0.03
0.25 – 0.32	2.64 ± 0.52	1.83 ± 0.36	-2.31 ± 0.04

Table 3.2: Medians of SFRs, stellar masses, dust masses (standard deviation in brackets) plotted in figure 3.3, and number of galaxies for each age bin.

log(age) [yr]	MS galaxies			below-MS				
	log(SFR) [$M_{\odot} \text{ yr}^{-1}$]	log($M_{stellar}$) [M_{\odot}]	log(M_{dust}) [M_{\odot}]	number of galaxies	log(SFR) [$M_{\odot} \text{ yr}^{-1}$]	log($M_{stellar}$) [M_{\odot}]	log(M_{dust}) [M_{\odot}]	number of galaxies
< 9.0	0.80 (0.56)	10.15 (0.61)	7.76 (0.54)	133	-0.64 (0.91)	9.95 (1.02)	7.63 (0.84)	15
9.0 – 9.2	0.72 (0.44)	10.48 (0.45)	7.78 (0.50)	151	-0.04 (0.43)	10.57 (0.51)	7.88 (0.56)	37
9.2 – 9.4	0.69 (0.39)	10.65 (0.39)	7.87 (0.40)	266	-0.04 (0.48)	10.71 (0.46)	7.87 (0.48)	171
9.4 – 9.5	0.53 (0.30)	10.72 (0.35)	7.77 (0.43)	119	0.04 (0.47)	10.78 (0.34)	7.93 (0.50)	207
9.5 – 9.6	0.47 (0.22)	10.81 (0.20)	7.67 (0.37)	33	-0.07 (0.48)	10.84 (0.33)	7.81 (0.47)	301
9.6 – 9.7	0.63 (0.47)	10.92 (0.31)	7.57 (0.37)	17	-0.27 (0.48)	10.93 (0.29)	7.77 (0.45)	328
9.7 – 9.8	0.52 (0.21)	10.66 (0.11)	7.94 (0.58)	3	-0.58 (0.54)	10.98 (0.31)	7.56 (0.52)	198
9.8 – 10.0	0	-0.97 (0.49)	10.96 (0.28)	7.32 (0.57)	71

Median and standard deviation calculated based on logarithmic values of SFR, $M_{stellar}$, and M_{dust} parameters in each bin.

Chapter 4

A long-duration GRB and its uncommon environment

The following Chapter published as Leńniewska et al. 2022, *The Interstellar Medium in the Environment of the Supernova-less Long-duration GRB 111005A*, ApJS, 259, 67.

Abstract

Long (> 2 s) gamma ray bursts (GRBs) are associated with explosions of massive stars, although in three instances, supernovae (SNe) have not been detected, despite deep observations. With new HI line and archival optical integral field spectroscopy data, we characterize the interstellar medium (ISM) of the host galaxy of one of these events, GRB 111005A, in order to shed light on the unclear nature of these peculiar objects.

We found that the atomic gas, radio continuum, and rotational patterns are in general very smooth throughout the galaxy, which does not indicate a recent gas inflow or outflow. There is also no gas concentration around the GRB position. The ISM in this galaxy differs from that in hosts of other GRBs and SNe, which may suggest that the progenitor of GRB 111005A was not an explosion of a very massive star (e.g. a compact object merger).

However, there are subtle irregularities of the GRB 111005A host (most at a 2σ level), which may point to a weak gas inflow or interaction. Since in the SE part of the host there is 15% more atomic gas and twice less molecular gas than in NW part, the molecular gas fraction is low. In the SE part there is also a region with very high H α equivalent width. There is more continuum 1.4 GHz emission to the SE and an S-shaped warp in the UV. Finally, there is also a low-metallicity region $3.5''$ (1 kpc) from the GRB position. Two galaxies within 300 kpc or a past merger can be responsible for these irregularities.

4.1 Introduction

It is well established that there are two types of gamma-ray bursts (GRBs) and they are divided based on the duration of their prompt emission (Kouveliotou et al. 1993). Those lasting less than 2 seconds are called short GRBs, with the cause of the explosion being the collision of compact objects (two neutron stars or a neutron star and a black hole; Abbott et al. 2017). The second group, longer than 2 seconds (long GRBs) are the result of the core collapse of very massive stars (Hjorth et al. 2003; Stanek et al. 2003) and take place in galaxies with ongoing star-formation (Christensen et al. 2004; Castro Cerón et al. 2006, 2010; Michałowski et al. 2008; Savaglio et al. 2009; Perley et al. 2013, 2015; Hunt et al. 2014).

Almost all long GRBs for which deep spectroscopic observations were carried out are accompanied by the explosion of supernovae type Ic (SN Ic; with no hydrogen, helium, or silicon lines in the spectrum; Hjorth & Bloom 2012). There are three exceptions for which the existence of a SN was ruled out down to deep limits: GRB 060505, 060614 (Fynbo et al. 2006; Della Valle et al. 2006; Gal-Yam et al. 2006), and 111005A (Michałowski et al. 2018c).

The most important question regarding these three objects is what their nature and their progenitors were. Some clues on the nature of unusual explosions can be obtained from the properties of gas in their environment (as was done for the enigmatic transient AT 2018cow; Michałowski et al. 2019b; Roychowdhury et al. 2019; Morokuma-Matsui et al. 2019). In this paper we focus on GRB 111005A. The current gas data for its host have too poor resolution to attempt this. Michałowski et al. (2018b) obtained a detection of the CO(2-1) line in three pointings and noticed that ESO 580-49, the host galaxy of GRB 111005A, is not symmetrically filled with molecular gas. The central and NW regions are molecule-rich for their star formation rates (SFR), but the SE region turned out to be molecule-deficient. The total molecular gas mass turned out to be similar as that of other galaxies with similar redshift, star formation rate (SFR), and stellar mass (Michałowski et al. 2018b; Hatsukade et al. 2020). Michałowski et al. (2015) examined the HI line in five GRB host galaxies at $z < 0.12$, including the GRB 111005A host using archival HI line from the Nançay radio telescope (Theureau et al. 1998; Springob et al. 2005). Due to poor spatial resolution, only the total atomic gas mass $M_{\text{HI,tot,single-dish}}$ was measured, and it turned out to be typical for the SFR and stellar mass of this galaxy.

The objective of this paper is to establish the properties of the interstellar medium (ISM) in the host of GRB 111005A, in order to help shed light on the nature of the progenitor. We use new HI and archival integral spectroscopy data to investigate both the atomic and the ionised gas.

We use a cosmological model with $H_0 = 70 \text{ km s}^{-1} \text{ Mpc}^{-1}$, $\Omega_\Lambda = 0.7$, and $\Omega_m = 0.3$. At the redshift of GRB 111005A of 0.01326 this corresponds to a scale of 0.27 kpc per 1".

4.2 GRB 111005A and its host

On October 5th 2011 GRB 111005A was detected by the Burst Alert Telescope (BAT, Barthelmy et al. 2005), onboard the *Swift* satellite. With a burst duration of 26 ± 7 sec (Barthelmy et al. 2011), it was classified as a long GRB. Machine-learning classification that successfully distinguishes between long and short GRBs, shows that GRB 111005A is in the long GRB part of the diagram, in common with other supernova-less long GRBs as well (Jespersen et al. 2020). In this analysis, GRB 111005A lies far from the short-duration group in a densely populated area, making it unlikely that it could belong to the short-duration group. This is consistent with its duration, putting it in the long category.

Michałowski et al. (2018c) carried out an analysis of the GRB afterglow and explosion environment based on new and archival radio, optical and mid-infrared data. With Very Long Baseline Array (VLBA) data the position of the radio afterglow was determined to be $\alpha = 14:53:07.8078276$, $\delta = -19:44:11.995387$ (J2000), with a 1σ error of 0.2 mas. The GRB was found to be associated with the galaxy ESO 580-49 at a redshift of $z = 0.01326$, exploding $\sim 1''$ from its centre, as defined on the 3.6 μm image (Michałowski et al. 2018c). The radio afterglow lightcurve turned out to be atypical. The afterglow exhibited a plateau phase lasting a month with a very rapid subsequent decay. These properties have never been observed before in a GRB. The host galaxy has been classified as Sbc in HyperLeda¹ with an edge-on inclination of 90° (Makarov et al. 2014). Based on full spectral energy distribution (SED) modelling including far-infrared data, Michałowski et al. (2018c) determined a star formation rate (SFR) of $0.42^{+0.06}_{-0.05} M_\odot \text{yr}^{-1}$ and stellar mass of $\log(M_*/M_\odot) = 9.68^{+0.13}_{-0.09}$ which is within the range of both long and short GRBs hosts (Savaglio et al. 2009; Castro Cerón et al. 2010; Perley et al. 2016; Fong et al. 2013; Berger 2014; Klose et al. 2019). Michałowski et al. (2018c) and Tanga et al. (2018) rejected the characterisation of the host galaxy as an active galactic nucleus (AGN) based on the Baldwin-Phillips-Terlevich (BPT) diagram (Baldwin et al. 1981).

Another rare feature of GRB 111005A was that no supernova was detected in the optical, near- and mid-infrared, down to an absolute magnitude of -12 mag at $3.6 \mu\text{m}$, ~ 20 times fainter than SNe associated with long GRBs. This cannot be explained by dust extinction, because in the mid-infrared its influence would be minor. This is similar to GRBs 060505 and 060614 (Fynbo et al. 2006; Della Valle et al. 2006; Gal-Yam et al. 2006).

Moreover, Michałowski et al. (2018c) showed that the explosion occurred in an environment with about solar metallicity. A very similar conclusion was reached by Tanga et al. (2018) based on integral field spectroscopy. They found that the host galaxy is metal-rich (near solar metallicity) and that there is little star formation at the GRB position. There are about twenty known GRBs that have exploded in environments with high (solar or super-solar) metallicity, (measured from absorption spectroscopy) (Prochaska et al. 2009; Krühler et al. 2012, 2015; Savaglio et al. 2012; Elliott et al. 2013; Schulze et al. 2014; Hashimoto et al. 2015; Schady et al. 2015;

¹leda.univ-lyon1.fr

Stanway et al. 2015). Metallicity is dependent on the galaxy stellar mass, so massive GRB hosts without metallicity measurements may also have high metallicity. Perley et al. (2016) presented an analysis of 119 galaxies up to redshift 6, of which about 10% are massive galaxies (stellar masses larger than $10^{10.5}$), which imply solar metallicity. However, all of them are at $z > 1$, whereas the GRB 111005A host is at a low redshift. GRB 130925A was also similar to GRB 111005A with respect to its proximity to the host centre (0.12" or 600 pc in projection; Schady et al. 2015). The lack of a SN, an atypical lightcurve, and the high (around solar) metallicity were used to claim that the explosion mechanism of GRB 111005A was different from that of the majority of GRBs (Michałowski et al. 2018c; Tanga et al. 2018).

4.3 Data

4.3.1 GMRT observations

In May and June 2016 the field of GRB 111005A was observed for 2×3 hrs with the Giant Metrewave Radio Telescope (GMRT)². For calibration of the flux and the bandpass 3C286 was observed for 15 min at the start and the end of the runs. For the phase calibration 1522-275 was observed every 30 min on one day and 1448-163 the other day with the same temporal spacing. The correlator was setup with 16 Mhz bandwidth and 512 channels centred around 1400 MHz.

The data were reduced with a range of data reduction packages. We downloaded the fits files with the raw data from the GMRT archive. These fits files were then loaded into CASA (McMullin et al. 2007) with the IMPORTGMRT task without applying the online flags. Further data reduction was done with the CARACAL³ pipeline which is being developed for HI data reduction of MeerKAT data. The pipeline is setup in a modular fashion using the platform-independent radio interferometry scripting framework STIMELA⁴. In practice this means that the calibrator data are initially flagged with AOFLAGGER (Offringa 2010) and calibrated and transferred to the target with CASA. After this the target is split out of the measurement set, further flagged with AOFLAGGER, imaged with WSCLEAN (Offringa et al. 2014) in Stokes I, using WSCLEAN's auto and fits masking feature after which this clean model is used in CUBICAL⁵ (Kenyon et al. 2018) for the self-calibration. This step is repeated until a phase-only self-calibration no longer improves the image and then subsequently an amplitude and phase self-calibration is performed where the solution interval for the amplitude and phase can differ.

After calibration the data for the two separate days were mapped onto the same channel grid with the CASA task MSTRANSFORM and the continuum was subtracted with UVCNTSUB. At this stage the data were also Doppler corrected and projected onto a barycentric velocity frame. As the data for the two separate days had opposite

²Project no. 30_035, PI: M. Michałowski

³<https://github.com/caracal-pipeline/caracal>

⁴<https://github.com/SpheMakh/Stimela/wiki>

⁵<https://github.com/ratt-ru/CubiCal>

sign frequency increment, the pipeline’s more advanced WSCLEAN tasks could not be used to invert the visibilities into an HI data cube. For this reason we did this final step manually in CASA. TCLEAN was used to transform the visibilities of the 60 channels covering the HI emission into a data cube. The visibilities were weighted according to a Briggs weighting scheme with the “robust” parameter set to 0 and a uvtaper of 7, 17, and 40 $k\lambda$ resulting in data cubes of different resolution. The dirty cubes were cleaned with TCLEAN’s multiscale clean algorithm, at scales of 1, 2 and 5 beams. The cleaning was performed in an iterative process in which we first cleaned the cube to a threshold of 10σ in the first iteration. From this first “cleaned” cube a mask was constructed with SOFIA (Serra et al. 2015) and then the emission in this mask was cleaned down to 0.5σ and a new mask was created. This last step was repeated until successive iterations showed no changes in the mask and all the visible emission was captured in the mask.

The final cubes had resolutions of $\text{FWHM} = 16.8'' \times 12.9''$, $7.4'' \times 5.7''$, and $4.0'' \times 2.8''$ and a channel width of 32.5 kHz (7 km s^{-1} at the HI frequency). The rms is 1.0, 0.7, and $0.6 \text{ mJy beam}^{-1}$ per channel. The frequency axis was converted into a velocity axis using the relativistic definition which results in a channel width of 6.96 km s^{-1} with an error of $\sim 0.005 \text{ km s}^{-1}$ on the outermost channels of the cube.

We also imaged the line-free channels to construct continuum images at the frequency of 1.4 GHz. We applied a uvtaper of 40, 17 and $5k\lambda$ resulting in a resolution of $4.7'' \times 3.2''$, $8.4'' \times 6.5''$ and $29.7'' \times 22.5''$ and an rms of 40, 66 and $178 \mu\text{Jy beam}^{-1}$, respectively. For the flux scale we note that the usual 10% calibration error applies for GMRT data.

4.3.2 MUSE data

We also used optical data obtained by Tanga et al. (2018). The galaxy in which GRB 111005A occurred was observed on the 23 August 2014 by the ESO Very Large Telescope equipped with the panoramic integral-field spectrograph working in the visible range, the Multi-Unit Spectroscopic Explorer (MUSE; Bacon et al. 2010).

The MUSE optical data obtained by Tanga et al. (2018) has previously been used in order to study the dust reddening $E(B - V)$, velocity map based on the $\text{H}\alpha$ line, equivalent width of the $\text{H}\alpha$ line, star formation rate surface density, and metallicity based on the Pettini & Pagel (2004, O3N2) and Dopita et al. (2016, D16) calibrations.

4.4 Tilted ring modelling

Due to the projection effects that are caused by the almost edge-on ($i > 85^\circ$) orientation of ESO 580-49 the rotation curve cannot be extracted from the velocity field. Therefore, in order to get a better understanding of the distribution and dynamics of the HI in ESO 580-49 we fit a tilted ring model (Rogstad et al. 1974) to the GMRT observations. The Fully Automated TiRiFiC (FAT, Kamphuis et al. 2015) fits the tilted ring model directly to the data cube and thus can also accurately model the

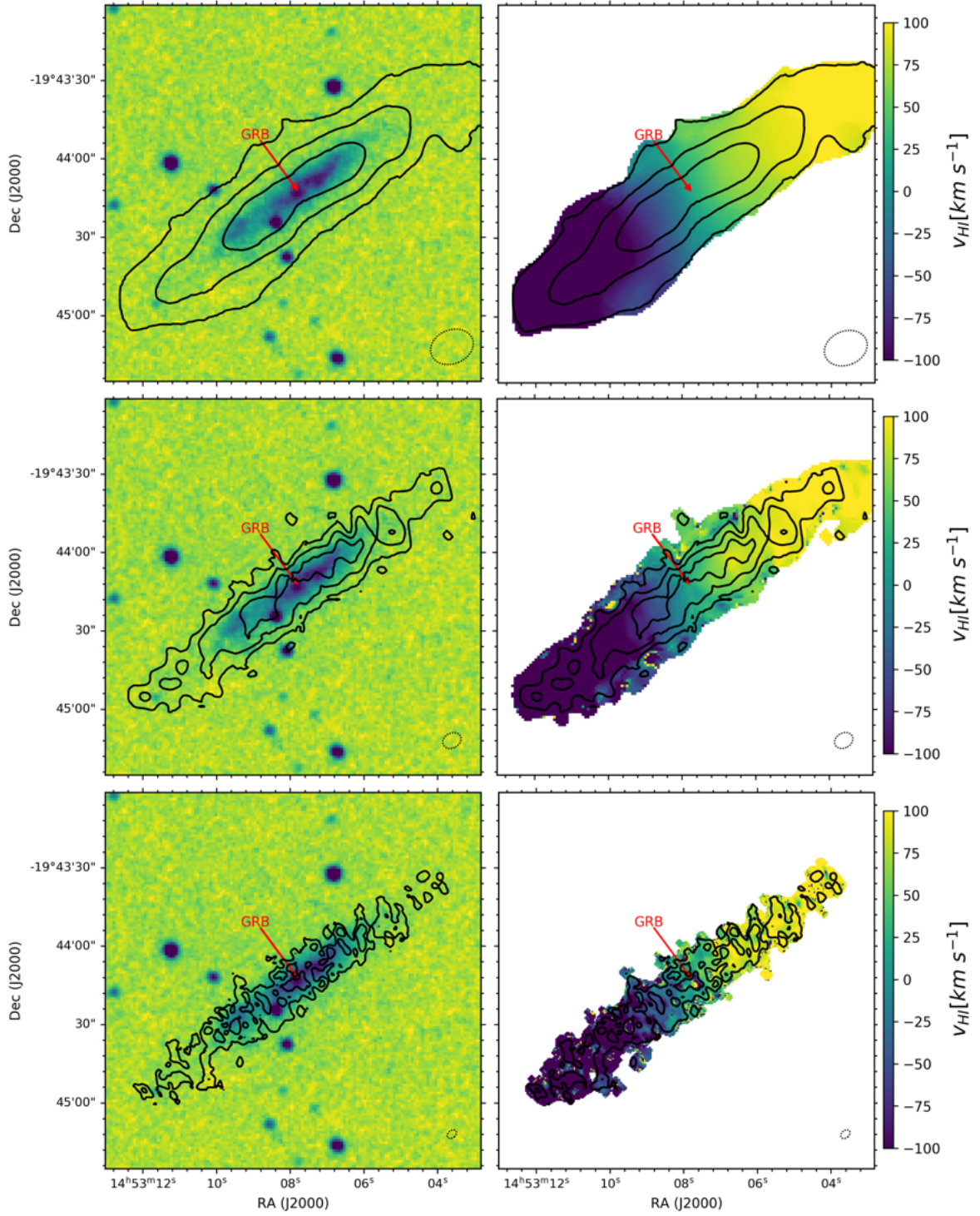


Figure 4.1: (Left) H I line emission of the GRB 111005A host (black contours) detected by GMRT with three different resolutions from top to bottom: $16.8'' \times 12.9''$, $7.4'' \times 5.7''$, and $4.0'' \times 2.8''$ (the beams are shown as grey dotted ellipses). The contours start at 0.7, 0.04, and 0.03 $\text{Jy beam}^{-1} \text{ km s}^{-1}$ from top to bottom. The lowest contours correspond to column densities of 3.7 , 1.1 , and $3.0 \times 10^{21} \text{ cm}^2$. The background is the UV image from Michałowski et al. (2018c). (Right) H I 1^{st} moment maps, with respect to the redshift $z = 0.01326$. The position of GRB 111005A is marked by the red arrow. The image size is $2.5' \times 2.5'$ corresponding to $40.5 \text{ kpc} \times 40.5 \text{ kpc}$.

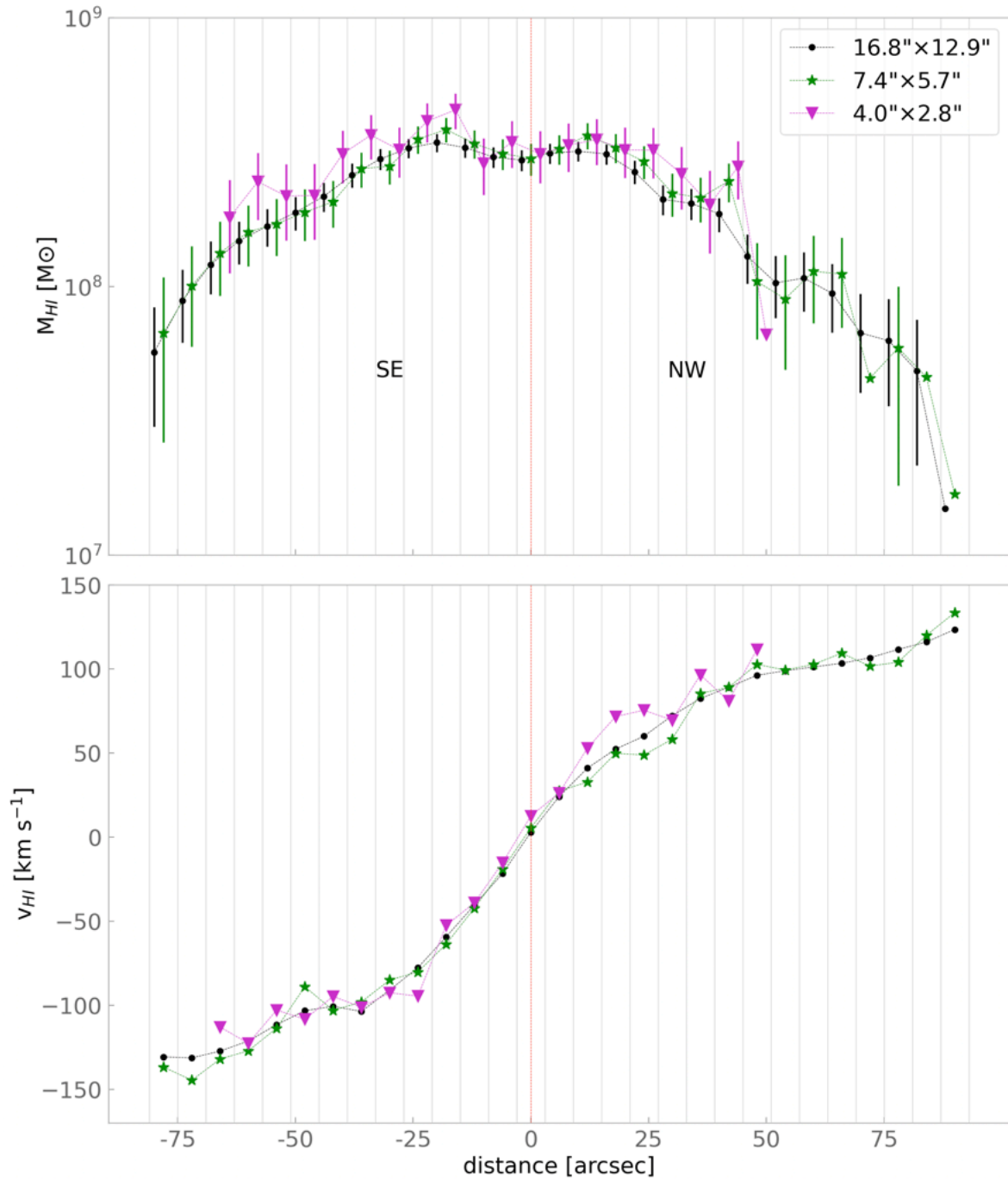


Figure 4.2: Profiles of the atomic gas mass derived from the HI maps shown on Fig. 4.1, as a function of distance from the galaxy centre (top) and the rotation curve from the velocity field of HI (bottom). For both panels the galaxy centre is marked as the red dashed line. The points on the top panel for which uncertainties are not shown represent upper limits.

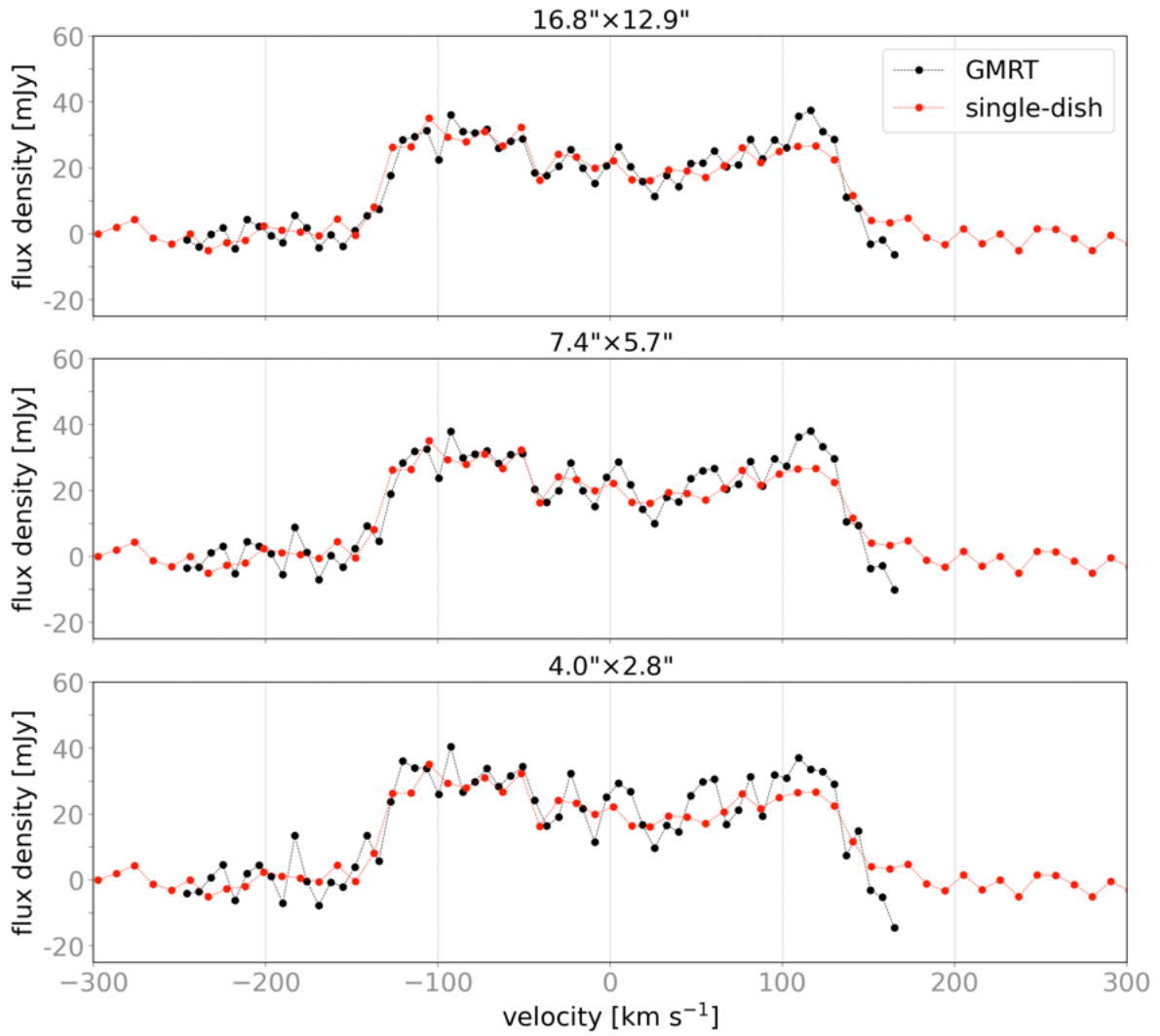


Figure 4.3: GMRT interferometric spectrum (black dots) at three different resolutions and the single-dish spectrum (red dots; Theureau et al. 1998). The velocity axis is with respect to the redshift $z = 0.01326$.

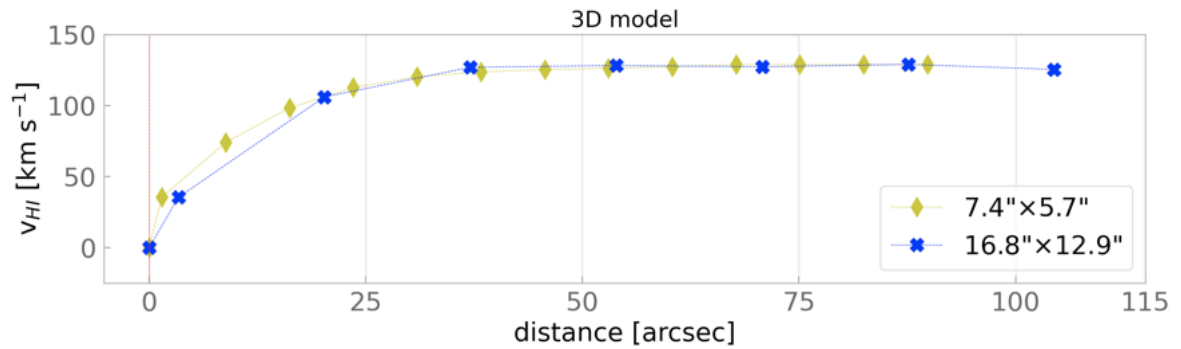


Figure 4.4: Rotation curves from the tilted ring modeling at two different resolutions as a function of distance from the galaxy centre.

Table 4.1: Properties of regions in the GRB 111005A host (Center, NW, and SE; see Fig. 4.10) and of the entire galaxy.

Reg.	RA/Dec	M_{HI} ($10^9 M_{\odot}$)			$M_{\text{HI}}/M_{\text{HI,tot}}$ (%)			molecular gas fraction (%)			Z		SFR ($M_{\odot} \text{ yr}^{-1}$)
		14.85"	6.55"	3.4"	14.85"	6.55"	3.4"	14.85"	6.55"	3.4"	12 + log(O/H) D16	O3N2	
Center	14:53:7.8	0.90	1.08	1.17	16.0	18.8	19.4	38.2	34.3	32.5	8.39	8.55	0.12
	-19:44:10.97	± 0.02	0.03	0.03	0.7	0.8	0.8	1.8	1.6	1.6			
NW	14:53:6.2	0.80	0.95	1.03	14.1	16.5	17.1	20.4	17.7	16.5	8.23	8.49	0.03
	-19:43:56.03	± 0.02	0.02	0.03	0.6	0.7	0.8	1.6	1.8	2.0			
SE	14:53:9.2	0.96	1.16	1.25	17.0	20.3	20.8	10.0	8.4	7.9	8.38	8.45	0.04
	-19:44:29.04	± 0.03	0.03	0.03	0.7	0.9	0.9	1.7	2.4	2.2			
Total		5.66	5.73	6.01	94.4 [†]	95.6 [†]	100.3 [†]	24.7	21.5	20.2	8.37	8.51	0.19
		± 0.19	0.20	0.22	4.4	4.6	4.9	1.5	1.5	1.5			

Atomic gas masses (M_{HI}), percentages of M_{HI} relative to the total mass of M_{HI} in the host galaxy (from the 'Total' row), percentages of molecular gas fractions ($M_{\text{H}_2}/M_{\text{gas}}$) based on the H_2 masses obtained by Michalowski et al. (2018b), metallicities determined from the Dopita et al. (2016, D16) and Pettini & Pagel (2004, O3N2) methods, and $\text{H}\alpha$ based star formation rates. The HI properties are given in three columns corresponding to three different resolutions, indicated in arcsec.

[†] indicates the ratio between the total amount of atomic gas from the GMRT data and the total amount of atomic gas measured by Michalowski et al. (2015) based on single-dish data.

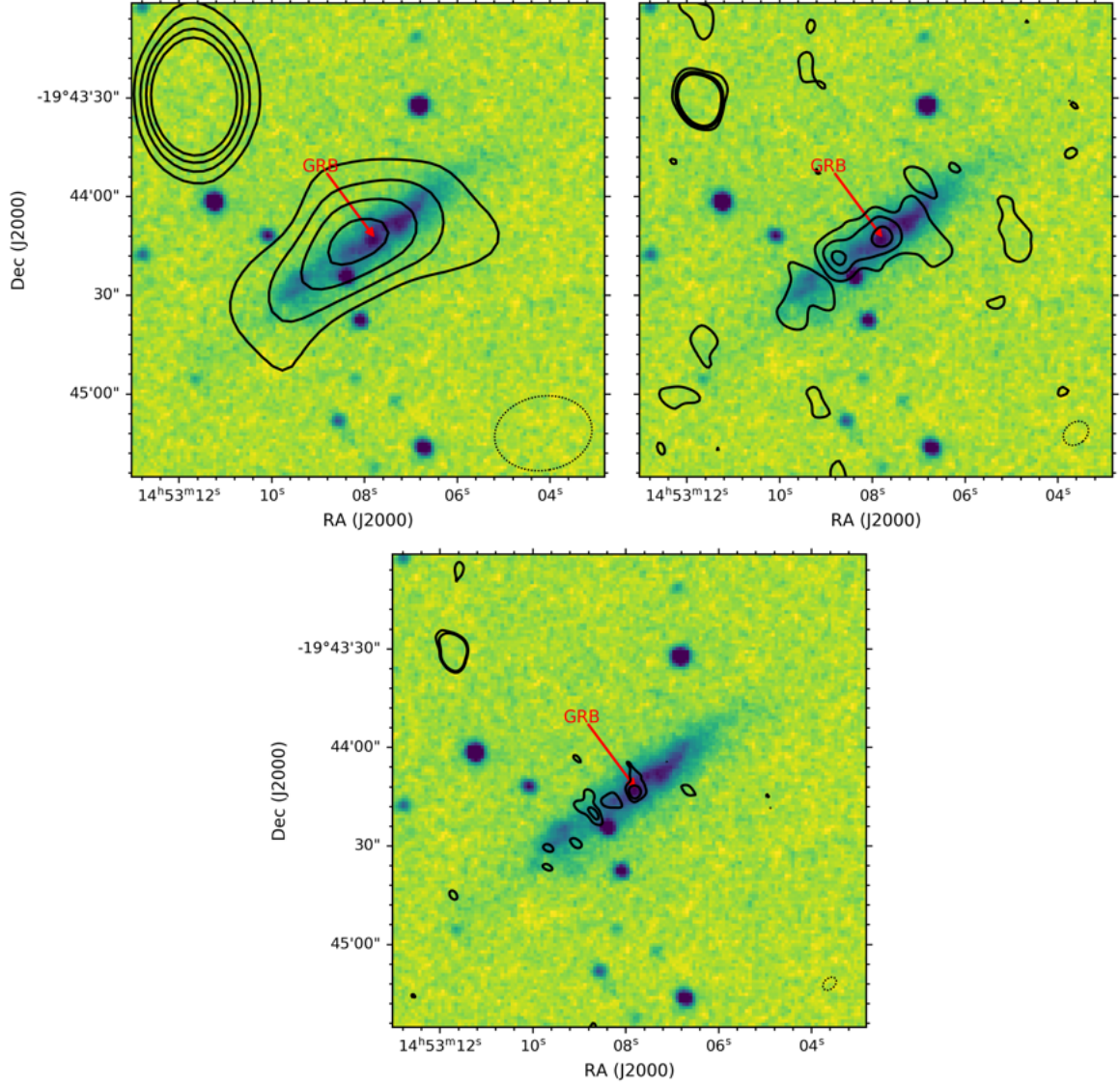


Figure 4.5: 1.4 GHz continuum emission of the GRB 111005A host (black contours) at three different resolutions: $29.7'' \times 22.5''$ (top left), $8.4'' \times 6.5''$ (top right), and $4.7'' \times 3.2''$ (bottom; the beams are shown as grey dotted ellipses). The contours are 3 , 5 , 7 , and 9σ , where $\sigma = 176$, 66 , and $40 \mu\text{Jy beam}^{-1}$ for low-, medium-, and high-resolution images, respectively. The background is the UV image from Michałowski et al. (2018c). The position of GRB 111005A is marked by the arrow. The image size is $2.5' \times 2.5'$ corresponding to $40.5 \text{ kpc} \times 40.5 \text{ kpc}$.

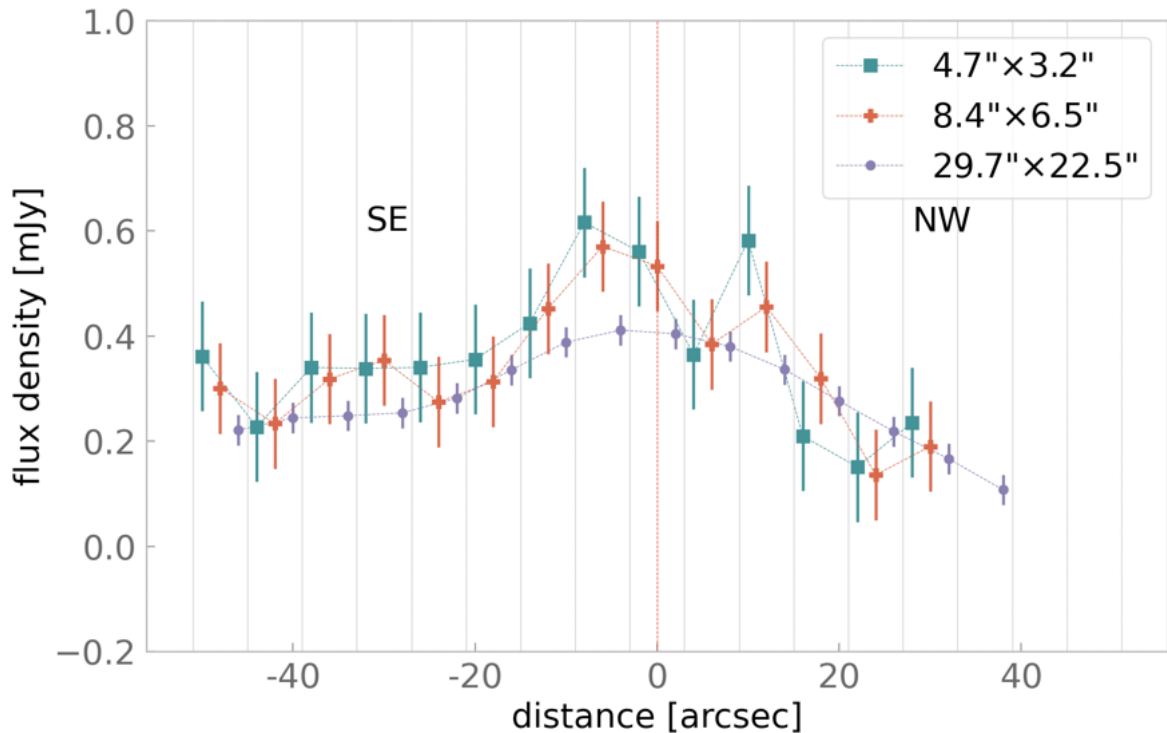


Figure 4.6: 1.4 GHz continuum emission profiles of the GRB 111005A host, using the maps with a resolution of $29.7'' \times 22.5''$, $8.4'' \times 6.5''$, and $4.7'' \times 3.2''$.

observed HI of discs with high inclination (Józsa et al. 2007).

FAT fits all the parameters relating to the orientation and position of the disc. As such it determines the central coordinates and scale height of the disc as a whole for the model and allows for radial variations in the position angle (PA), inclination, rotational velocity, dispersion and surface brightness profile. We run FAT on the different resolution data cubes independently.

For the highest resolution data ($\text{FWHM} = 4.0'' \times 2.8''$) FAT was unable to find enough flux in the data cube to reliably initiate the fitting process and hence no model was created. The lower resolutions were successfully fitted and all parameters are consistent between the two models at medium and low resolutions. No radial variations are found in the dispersion, inclination, and PA.

4.5 Results

Our GMRT HI data, the measurements made by MUSE (Tanga et al. 2018) and the ultraviolet (UV) image (Michałowski et al. 2018c) of the host galaxy of GRB 111005A are presented in Figures 4.1–4.8. We show the intensity maps as well as profiles along the galaxy. The profiles were constructed for all maps by measuring the signal in rectangular apertures perpendicular to the galaxy disk with a width of $6''$ and height of $17''$, encompassing together the entire detectable emission. Fig. 4.9 in the appendix show the color-scale images of the moment 0 and continuum maps.

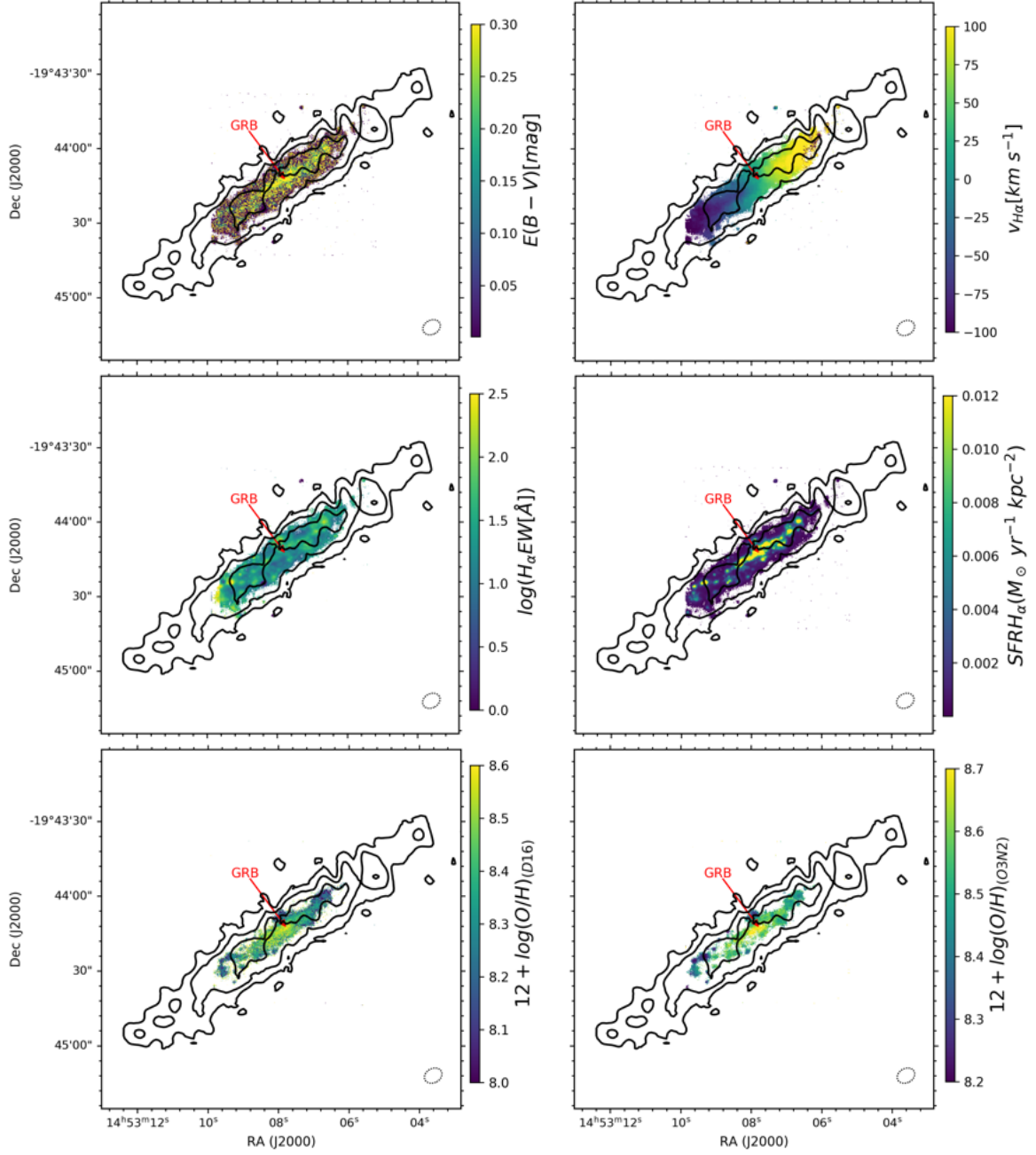


Figure 4.7: Atomic gas emission of the GRB 111005A host from GMRT with a resolution of $7.4'' \times 5.7''$ (black contours) overlaid on maps of physical properties derived from MUSE observations by Tanga et al. (2018). (Top left) Dust reddening $E(B-V)$. (Top right) Velocity map (1st moment) based on the $H\alpha$ line, with respect to the redshift $z = 0.01326$. (Middle left) Equivalent width of $H\alpha$. (Middle right) Star formation rate surface density derived from the $H\alpha$ emission. (Bottom left) Metallicity using the diagnostic of Dopita et al. (2016). (Bottom right) Metallicity based on the O3N2 method (Pettini & Pagel 2004). The position of GRB 111005A is marked by the red arrow. The beam of HI observations is shown as a grey dotted ellipse. The image size is $2.5' \times 2.5'$ corresponding to $40.5 \text{ kpc} \times 40.5 \text{ kpc}$.

The host has a clear S-shaped (‘integral sign’) warp in the UV image, which was not discussed in Michałowski et al. (2018c).

4.5.1 Residual scaling correction

The HI and radio continuum fluxes in a given region appears to increase with increasing resolution of the cube. This is counter-intuitive, because usually better resolution leads to more flux being missed. First, we stress that for the most of the apertures the increase is less significant than 1σ and the maximum significance is only 2σ . We however investigated the reason of this behaviour. In order to confirm that the masking does not introduce biases we performed cleaning at all resolution with a fixed masked defined by the emission from a low-resolution cube tapered at $5\text{ k}\lambda$ and by just drawing a rectangle around the visible emission. In both cases we obtained similar results to our original analysis. We also repeated the analysis without the TCLEAN’s multiscale clean algorithm, again obtaining similar results.

We conclude that the flux increase with resolution is due to a higher fraction of uncleaned flux and stronger sidelobes in the dirty beam at higher resolutions. This makes the conversions from Jy beam^{-1} to Jy pixel^{-1} increasingly uncertain, because the uncleaned emission is not distributed according to a clean Gaussian beam with which the conversion is defined. We verified that this is the case by noting that the flux increase towards the highest resolution is proportional to the difference between the areas of the dirty and cleaned beams.

Hence, all HI and radio continuum flux measurements were corrected for this effect using the method presented in Novak et al. (2019, 2020), which is based on scaling the residual map by the ratio of areas of the clean and dirty beams. For a given map and aperture size, this ratio can be found as $\epsilon = C/(D - R)$, where C , D , and R are the measurements in this aperture with the clean component map, the dirty image and the residual image. Then the true flux is $C + \epsilon R$. In this way the residuals are scaled so that their unit matches that of the clean component map.

As expected, in this way the difference between fluxes at different resolutions decreased to a level less than 1σ for all the measurements except of the difference between the HI measurements at the coarsest and middle resolutions for the circular apertures (Table 4.1). The difference is less than 0.5σ for the same cubes for larger apertures encompassing the entire galaxy (the last row of Table 4.1) or halves of the galaxy (Table 4.2), so it is likely because the small circular apertures (matching the CO apertures) are too small and comparable with the beam size at the coarsest resolution, so the residual correction method works less efficiently for them. Hence, the HI flux measurements in small circular apertures for the low-resolution cube are less reliable.

4.5.2 Atomic and molecular gas

The left panels of Fig. 4.1 show the contours of the HI line (moment 0 maps) at three different resolutions overlaid on the UV image. Atomic gas is smoothly distributed in the disk without any significant off-centre concentrations, plumes, or extra-planar gas,

which could have suggested a recent inflow/outflow of gas or environmental interactions. Specifically, there is no concentration of atomic gas at the GRB position. There is however $\sim 15\%$ more atomic gas in the SE part of the galaxy, which is visible at all resolutions. The ratios of the atomic gas mass in the SE and NW halves are 1.16 ± 0.04 (14.85"), 1.15 ± 0.04 (6.55"), and 1.14 ± 0.05 (3.4"). The difference in the extent of the UV emission and atomic gas is clearly visible, with the atomic disk extending beyond the UV disk, which is common for spiral galaxies (e.g. Wang et al. 2013).

The right panels of Fig. 4.1 show the intensity weighted mean velocity maps. The velocity pattern is regular, as expected for a non-disturbed rotating disk.

Fig. 4.2 presents the profiles of the HI emission along the galaxy. The top panel shows the HI mass distribution, which is relatively symmetric, but in the NW part the HI profile falls off faster. The lower panel presents the rotation curves derived from the mean velocity (moment 1) maps. We explored this to search for any irregularities in the moment 1 maps, which we did not find. We note that the rotation curves derived from the tilted ring modelling (see below) are more accurate. The full velocity width is around 250 km s^{-1} .

Michałowski et al. (2018b) analysed the CO distribution in three regions in the host galaxy (see their Fig. 1) and we performed analysis of atomic gas and properties derived from MUSE data at the same locations. The total signal from each region was measured using the Starlink package (Currie et al. 2014) with an aperture radius of 13.6", matching the beam size of the CO observations. From the total HI fluxes we measured the HI masses (M_{HI}) based on eq. 2 in Devereux & Young (1990). The positions of the apertures on our HI map is shown on Fig. 4.10 in the appendix. We also used an elliptical aperture encompassing the entire galaxy to calculate the total atomic gas mass ($M_{HI,tot}$). Table 4.1 lists the results of these aperture photometry measurements.

The distribution of atomic gas is slightly asymmetric: there is around $15 \pm 5\%$ more gas in the SE region than in the the NW region. This was suggested by Michałowski et al. (2018c) based on the asymmetry of the HI line shape. We also calculated the molecular gas fraction using the molecular masses obtained by Michałowski et al. (2018b). The SE region has twice lower molecular gas mass and higher atomic gas mass than the NW region, so the molecular gas fraction is low [$M_{H2}/M_{gas} \sim (8.5 \pm 2)\%$, or $M_{H2}/M_{HI} \sim 0.1$, see Table 4.1]. This region encompasses one third of the host, but such low ratios are only found at the very outskirts of other galaxies (Leroy et al. 2008, their Fig. 17).

For the entire galaxy the atomic hydrogen mass was calculated using an elliptical aperture encompassing all the detected emission. The value measured here is consistent ($M_{HI,tot}/M_{HI,tot,single-dish} \sim (97 \pm 4)\%$) with the measurement reported in Michałowski et al. (2015) based on the single-dish spectrum from Theureau et al. (1998), especially taking into account the 10% flux calibration uncertainty. Fig. 4.3 shows the comparison of this single-dish HI spectrum and our GMRT observations at three spatial resolutions. The spectra are consistent with each other indicating that GMRT did not miss any extended emission.

4.5.3 Kinematic modelling

Table 4.3 presents the properties of the GRB 111005A host based on the tilted ring modelling (Sect. 4.4) of low- and medium-resolution HI cubes. Inclination values confirm that the model is consistent with a nearly edge-on orientation. The position of the galaxy centre determined in the modelling is consistent with the position of GRB 111005A within $1-2\sigma$. The GRB position is $0.1''$ and $2.1''$ away from the centre in the low-resolution cube in right ascension and declination, respectively, whereas the errors of the centre position are $0.2''$ and $2.5''$. For the medium-resolution cube the distance is $0.2''$ and $2.8''$ and the errors are $0.1''$ and $1.1''$.

The rotation curves derived from the tilted ring modelling are shown in Fig. 4.4 for data with resolutions of $16.8'' \times 12.9''$ and $7.4'' \times 5.7''$. They present a flattening at large radii, typical for spiral galaxies (e.g. Rubin et al. 1980), which signals a dominant dark matter contribution. Based on the maximum rotational velocity we calculated a total dynamical mass of the galaxy of $10.8 \times 10^{10} M_{\odot}$ (the $14.85''$ data) and $9.7 \times 10^{10} M_{\odot}$ (the $6.55''$ data). Subtracting the total HI mass from Table 4.1, H_2 mass from Michałowski et al. (2018b), and stellar mass from Michałowski et al. (2018c), we estimated a dark matter mass of $9.7 \times 10^{10} M_{\odot}$ ($14.85''$) and $8.6 \times 10^{10} M_{\odot}$ ($6.55''$). This corresponds to a dark matter fraction around 90%, so this galaxy is dark-matter dominated.

The ratios of the HI masses included in these models and the HI masses measured directly from the GMRT data show that the model is able to explain $(83 \pm 3)\%$ and $(70 \pm 3)\%$ of the emission in low- and mid-resolution cubes, respectively. We also compared the GRB 111005A host with the very tight relation between M_{HI} and D_{HI} of Wang et al. (2016, their eq. 2). With a diameter of $178.9''$ and $158.8''$ (after deconvolving the beam, at a surface density of $1 M_{\odot} \text{ pc}^{-2}$), this relation predicts the HI mass of $6.9 \times 10^9 M_{\odot}$ and $5.4 \times 10^9 M_{\odot}$, respectively, factor of 1.33 ± 0.04 and 1.03 ± 0.03 above the measured value. Hence, the host galaxy is 0.13 or 0.02 dex below this relation. The scatter of the relation is 0.06 dex, so the GRB 111005A host galaxy is located at most 2 sigma away from it.

4.5.4 Radio continuum

Radio continuum emission at 1.4 GHz presented in Fig. 4.5 reflects the star formation rate in the host galaxy and has a similar extent to the UV emission. To first order, the maps at the three different resolutions show a symmetrical structure. However, they all show slightly more emission to the SE of the galaxy, with $(64 \pm 54)\%$ more in the SE part at the lowest resolution.

Radio 1.4 GHz continuum profiles are shown in Fig. 4.6. The data show a hint of asymmetry at all resolutions, with the peak brightness shifted to the SE from the optical galaxy centre and the emission extending further in the SE direction. However, the sizes of error bars and the beam sizes prevent drawing a definite conclusion on this.

4.5.5 Stars, ionised gas and dust

The H α SFR is corrected for dust extinction assuming the Calzetti et al. (1994) attenuation law with $R_V=4.05$. It is based on the H α flux to SFR conversion described in Kennicutt (1998) but assuming a Chabrier IMF (Chabrier 2003b), which reduces the SFR by a factor of ~ 1.7 compared to a Salpeter IMF.

Regardless of the differences in gas content, the H α -based SFRs in the NW and SE regions are very similar (Table 4.1). Using a hybrid calibration combining H α with IR luminosities (Kennicutt & Evans 2012), we obtained an SFR of $0.43 M_\odot \text{ yr}^{-1}$, which is consistent with that presented by Michałowski et al. (2018c) based on infrared luminosity. The total SFR determined from the H α alone is $0.19 M_\odot \text{ yr}^{-1}$, two times smaller than the IR-based SFR determined by Michałowski et al. (2018c). Similarly, the total radio continuum flux (Table 4.2) implies an SFR of $0.15 M_\odot \text{ yr}^{-1}$ (with the calibration of Bell 2003). The factor of two difference between these estimates and the IR SFR is within the typical calibration uncertainty, but indicates a contribution of evolved stars to dust heating, making the IR estimate too large. However, we cannot rule out the possibility that the H α estimate is underestimated due to dust extinction and the radio estimate is underestimated due to age effects.

Fig. 4.7 shows physical quantities derived from MUSE data (Tanga et al. 2018) superimposed on the HI moment zero map. We show the full $1'$ extent of the data, whereas Tanga et al. (2018) showed the central $20''$. We present the SFR and the O3N2 metallicity maps for the first time. We infer the following results from these data. Similarly to the HI observations, the H α velocity map shows a regular rotational pattern, also noted by Tanga et al. (2018). Dust reddening $E(B-V)$ is highest along the middle of the disk, as expected given the prominent dust lanes (Fig. 15 of Michałowski et al. 2018c). These central regions are also much more active than regions further from the disk plane, given the SFR surface density map based on the H α emission. The H α equivalent width is a proxy of the age of a stellar population in young (~ 10 Myr) starbursts (Stasińska & Leitherer 1996; Fernandes et al. 2003). There are several regions with higher equivalent widths (~ 200 and resulting lower ages), mostly at both ends of the disk and $3.5''$ (1 kpc) north-east of the centre (the latter was discussed by Tanga et al. 2018). Two methods were used by Tanga et al. (2018) to measure metallicity in the host galaxy. Both diagnostics show a typical radial behaviour with metallicity declining towards the outskirts. The region north-east of the galaxy centre does not fit into this pattern because it has as low metallicity as the regions at a similar height above the disk, but located much further from the centre ($12 + \log(O/H) = 8.1-8.2$). The diagnostic of Dopita et al. (2016) resulted in the NW region being the most metal-poor, but this is not reflected in the O3N2 method (Pettini & Pagel 2004). Consistently with each other, both methods result in low metallicity for the SE part.

Fig. 4.8 shows the profiles of six parameters calculated based on the MUSE data. Such analysis was not done by Tanga et al. 2018. Dust reddening, $E(B-V)$, shows the largest value in the centre of the host galaxy decreasing with distance. The NW region is more reddened, with $E(B-V)$ decreasing less than in the SE half. The H α velocity profile is very symmetrical. The H α equivalent width is relatively flat, but the outermost region towards the SE reaches 150 \AA and clearly stands out from the other

locations. The highest value of the star formation density is found in the centre of the galaxy, near the GRB 111005A position, generally declining outwards. For metallicities derived with both the D16 and O3N2 methods, the highest value occurs in the second aperture, 6" from the centre towards SE. This behaviour seems similar to the case of the 1.4 GHz profiles presented in Fig.4.6. This is because of the low-metallicity region north-east of the galaxy centre, lowering the average metallicity in the central aperture. An asymmetry is also evident in both metallicity profiles. The D16 metallicity in the SE half is higher than in the NW half, while we see the opposite for the O3N2 method.

We made similar measurements as in Table 4.1 to investigate the differences between the two halves (SE and NW) of the galaxy. In Table 4.2 we show the results of the aperture photometry on GMRT and MUSE maps with two apertures together encompassing the entire galaxy. There is more atomic gas in the SE half and this is true for each resolution, but the difference is significant only at a $\sim 2\sigma$ level. A similar difference is apparent for the radio continuum flux. The average dust reddening for both halves is similar, unlike what the profile suggests (Fig. 4.8). This is because the average value is dominated by a large number of pixels with low $E(B - V)$. Due to regions with high H α equivalent widths in the SE end of the galaxy, the corresponding half has a high average value of this parameter. The total H α SFRs of the galaxy halves are comparable. In the case of metallicity, we again see differences in results depending on the method used. For D16 the average metallicity of the SE half is higher, whereas the O3N2 method results in similar values for both halves.

4.5.6 Large-scale environment

We also analysed the large-scale environment around the GRB 111005A host using the NASA/IPAC Extragalactic Database (NED). The closest galaxies are WISEA J145239.17-192125.8 and ESO 580-G052, 24' and 30' (321 kpc and 301 kpc) away, respectively. Within 1 Mpc in projection and $\Delta v = \pm 1500 \text{ km s}^{-1}$ there are 6 galaxies. Moreover, 1.37 Mpc (1.4 deg) away from the GRB 111005A host there is a galaxy group with NGC 5791 as the brightest member (Crook et al. 2007; Díaz-Giménez et al. 2012). The GRB 111005A host appears to lie in the outskirts of this group.

We note that the SN-less GRB 060505 was found 4 Mpc from a galaxy cluster (Thöne et al. 2008), whereas the relativistic SN 2009bb was found 600 kpc from a galaxy group (Michałowski et al. 2018a). The small number of such studies prevents drawing firm conclusions.

4.6 Discussion

The host of GRB 111005A displays many regular features: largely symmetrical atomic gas (Fig. 4.1 and 4.2, Table 4.2) and radio continuum (Fig. 4.5 and 4.6, Table 4.2) distributions, and rotational patterns derived from both HI and H α lines (Fig. 4.7 and 4.8). There are only small deviations from this regularity, which will be discussed below.

Hence, there is no evidence of strong and recent gas inflow/outflow or environmental interactions. This is different from the irregular ISM distributions in the hosts of GRBs, broad-lined type Ic (Ic-BL) SNe, and fast radio bursts (FRBs). Four such explosions were found near the most significant concentration of atomic gas: GRB 980425 (Arabsalmani et al. 2015, 2019; Michałowski et al. 2015), GRB 060505 (Michałowski et al. 2015), SN 2009bb (Michałowski et al. 2018a), and SN 2002ap (Michałowski et al. 2020a). Moreover, GRB 980425 (Michałowski et al. 2014, 2016), GRB 060505 (Thöne et al. 2008, 2014), GRB 100316D (Izzo et al. 2017), and SN 2009bb (Michałowski et al. 2018a) exploded close to the region that is the brightest in the infrared, radio, H α , and [OI]. Similarly, the HI line profiles of two FRB hosts for which such measurement is possible were found to be extremely asymmetric, compared to those of the general population of galaxies (Michałowski 2021). On the other hand the ISM was found to be more regular for the host of SNe type Ib (Michałowski et al. 2020b) and the transient AT 2018cow (Michałowski et al. 2019b). However, Roychowdhury et al. (2019) reported AT 2018cow in a distorted dense HI ring-like structure.

Most long nearby GRBs for which deep spectral observations are possible are associated with SNe type Ic-BL (Hjorth & Bloom 2012), exhibit sub-solar metallicities in their environments (Leloudas et al. 2011; Modjaz et al. 2011; Japelj et al. 2016), and exploded in galaxies with irregular ISM distributions (see above). On the other hand, GRB 111005A was not associated with an SN, exploded in a region with solar metallicity, and its host has a regular ISM distribution. These properties may suggest that the progenitor of GRB 111005A is different from that of most long GRBs. This could be a compact object merger (Wang et al. 2017; Michałowski et al. 2018c; Tanga et al. 2018; Yue et al. 2018; Dado & Dar 2018). Indeed, the host galaxy of the neutron star merger GW 170817 has a regular ISM distribution with only minor irregularities (Levan et al. 2017). Low numbers of GRB hosts with characterised ISM properties precludes drawing conclusions from the ISM distribution alone.

There are a few more subtle irregularities of the GRB 111005A host, which may point to a weak gas inflow or interaction. We note that these irregularities are weak and the significance of most of them is around 2σ , so deeper observations are needed to investigate this topic. However, these irregularities were found in independent datasets, so their combined significance is higher. We also note that these features can in principle be explained by different mechanisms.

The S-shape of the galaxy, clear on the UV image (Fig. 4.5), 2σ asymmetry in the 1.4 GHz continuum image (Figs. 4.5 and 4.6, Table 4.2), and the asymmetric HI profile (Fig. 4.3) suggests an interaction. S-shaped warps in stellar (Reshetnikov & Combes 1999; Reshetnikov et al. 2016; Ann & Park 2006) and HI (Sancisi et al. 2008) distributions are common and were claimed to be indications of tidal interaction or gas accretion. Similarly, S-shapes in simulations have been induced by interactions, or by gas accretion, and can be sustained several Gyr after such events (Kim et al. 2014; Gómez et al. 2016, 2017; Semczuk et al. 2020). Such a long timescale makes the GRB event unlikely to be connected with a potential interaction. Ram pressure stripping can also induce S-shaped warps (Haan & Braun 2014), but this probably does not apply to the GRB 111005A host because it is more than 1 Mpc away from a galaxy group, so the intragroup medium density is unlikely to be high at its position and any infall

velocity must be low.

Asymmetric HI spectrum (Michałowski et al. 2018c; Fig. 4.3) resulting from more atomic gas in the SE part of the galaxy (Table 4.2) also indicates external influence, e.g. tidal interaction or gas inflow. Indeed, Watts et al. (2020) found that galaxies with asymmetric HI line profiles generally contain 29% less HI than their symmetric counterparts, and this is due to gas removal during the interaction with galaxy environment (see also Reynolds et al. 2020; Hu et al. 2021). Indeed, the host of GRB 111005A contains $(35 \pm 4)\%$ less atomic gas than predicted from the relation between the atomic gas and size (see Sect. 4.5.3).

We quantified the HI line asymmetry of the GRB 111005A host using the diagnostics defined by Reynolds et al. (2020). The GRB 111005A host has a difference between the flux-weighted velocity and the midpoint velocity at 50% of the peak flux of $\Delta V_{\text{sys}} = 2.6 \text{ km s}^{-1}$ (eq. 4 in Reynolds et al. 2020); the integrated flux ratio between the left and right halves of the spectrum of $A_{\text{flux}} = 1.24$ (eq. 6); the flux ratio between the left and right peaks of the spectrum of $A_{\text{peak}} = 1.31$ (eq. 7); and the residual from the subtraction of the spectrum flipped around the flux-weighted velocity from the original spectrum of $A_{\text{spec}} = 0.26$ (eq. 8). We compared these values with measurements for galaxies with stellar masses of $9 < \log(M_{\text{star}}/M_{\odot}) < 10$ from the Local Volume HI Survey (LVHIS; Koribalski et al. 2018) and the VLA Imaging of Virgo in Atomic Gas (VIVA; Chung et al. 2009), with low and high environmental density respectively (see Fig. 8 and Table 3 of Reynolds et al. 2020). All asymmetry diagnostics for the GRB 111005A host, except A_{spec} , are 1–2 standard deviations higher than the mean for the low-density LVHIS galaxies and consistent with the mean for the high-density VIVA galaxies. Hence, the HI spectrum of the GRB 111005A host is at the highest end of asymmetry for galaxies in the low-density environments and is similarly asymmetric as spectra of galaxies in a cluster. This supports the hypothesis that this asymmetry is related to the interaction with the environment (gas inflow, merger, etc.).

The SE part of the galaxy also shows some features, which may suggest gas accretion. There is twice less molecular gas (Michałowski et al. 2018b) and more atomic gas than in the NW part, so the molecular gas fraction is approximately a factor of two lower, but this is significant only at a 2σ level (Tables 4.1 and 4.2). The radio continuum emission is also stronger in the SE than in the NW (Figs. 4.5, 4.6 and Table 4.2), again significant at a 2σ level. If these differences are confirmed with deeper data, then they can be explained by either interaction or gas inflow. Both processes can lead to higher atomic gas density in a part of a galaxy (either directly during inflow or by rearranging gas distribution during interaction). This can also enhance the SFR at that position due to a higher gas density, explaining stronger radio emission. If this process was recent, then the HI to H₂ conversion has not taken place yet. The metallicity effect could in principle explain low CO emission (Bolatto et al. 2013), but we measured a similar metallicity in the CO-rich north-western part (Fig. 4.7, 4.8 and Table 4.1), so this is not the case for the SE region.

Similarly, the region just outside of the galaxy centre, 3.5" (1 kpc) to the north-east has unusual properties (see Figs. 5–7 of Tanga et al. 2018 for a zoom-in view of the MUSE data). It has untypically low metallicity (8.15 for the D16 calibration and 8.25 for the O3N2 calibration), compared to other regions at similar galactocentric

distances, and exhibits high $H\alpha$ equivalent width (~ 200), suggesting a very young stellar population (Fig. 4.7). These properties are consistent with gas flowing from the intergalactic medium and enhancing star formation (see also Sánchez Almeida et al. 2013, 2014b,a, 2015). However, only the detection of a stream of gas extending outside the galaxy would provide strong evidence supporting this conclusion. If this is correct, then the birth of the progenitor of GRB 111005A may be related to this process.

On the other hand, we did not find any definitive signature of outflows. The MUSE spectrum at the GRB 111005A position does not show any deviation from a single Gaussian profile. Conversely, Thöne et al. (2021) found that all long GRB hosts experience strong outflows, based on the existence of broad mostly blueshifted $H\alpha$ components, kinematically decoupled from narrow components. However, in our case, even if such an outflow is present, we would not be able to detect it in the spectra, because it would likely be directed perpendicular to the line-of-sight for this edge-on galaxy.

With our radio continuum image (Fig. 4.5) we can also test for the presence of a radio-loud AGN. We did not detect a strong point source in the centre, so we rule out this possibility.

The reason for the discrepancy between the metallicity measurements using the D16 and O3O2 methods (Fig. 4.8 and Table 4.1) is likely the same as described in Krühler et al. (2012). Namely the O3N2 method misinterprets highly ionised regions for having low metallicity. The D16 method takes ionisation into account and therefore is more accurate.

Interaction with two nearby galaxies 300 kpc away (in projection) may be responsible for the S-shape of the GRB 111005A host, if in the past they were closer. The distortion may also be due to a past minor merger. On the other hand the projected distance to the NGC 5791 galaxy group of 1.37 Mpc makes it unlikely that interaction with the group can significantly modify the distribution of gas or stars the GRB 111005A host. However, the proximity to the group implies the presence of a supply of intergalactic gas to be accreted by the GRB 111005A host. A similar situation was found for the SN 2009bb host (Michałowski et al. 2018a). The projected virial radius of the NGC 5791 group is 0.24 Mpc (Crook et al. 2007, based on the separations of the group members). Hot, X-ray emitting gas has been detected out to more than 0.5 Mpc from group centres (Rasmussen & Ponman 2007; Mernier et al. 2017). Hence, the GRB 111005A host is not a member of this group, but at its position, i.e. at the distance of 3–4 times the group radius, one can expect some gas from the group.

4.7 Conclusions

Based on new GMRT and archival MUSE observations of the host galaxy of the unusual long GRB 111005A, we have characterized the interstellar medium properties of the host across the galaxy and in the vicinity of the GRB explosion. Deep observations of SN-less GRB hosts are scarce and hence this study contributes significantly to the understanding of ISM properties in such galaxies.

The host galaxy of GRB 111005A is characterized by regular largely symmetrical

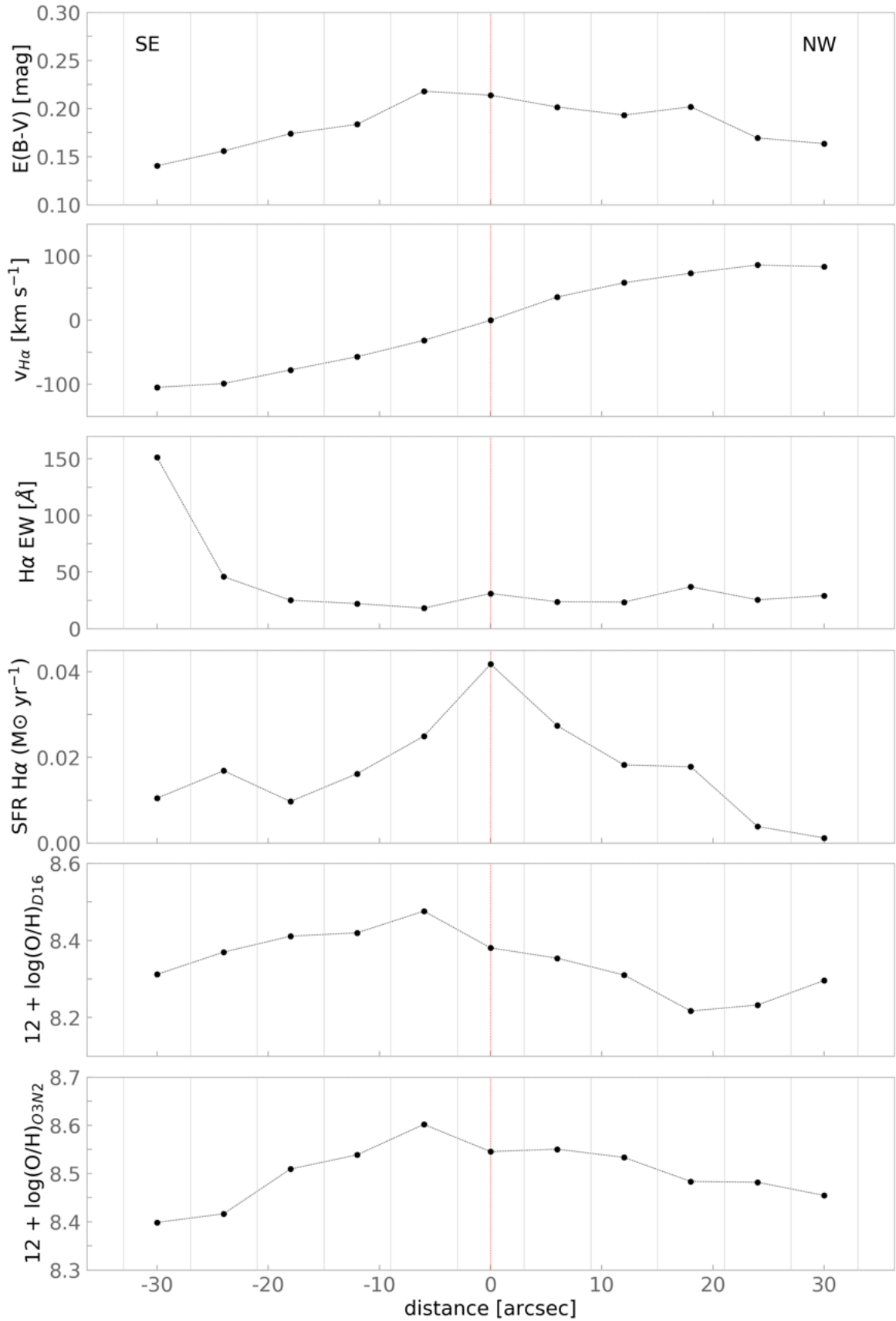


Figure 4.8: Profiles of properties derived using the MUSE data (Fig. 4.7) as a function of the distance from the galaxy centre (red dashed line).

Table 4.2: Properties of two parts in the GRB 111005A host (NW half and SE half).

Reg.	M_{HI} ($10^9 M_{\odot}$)		1.4 GHz (mJy)		$E(B-V)$ (mag)	H α EW (\AA)	Z	SFR ($M_{\odot} \text{ yr}^{-1}$)		
	14.85"	6.55"	3.4"	26.5"	7.45"	3.95"	D16 O3N2			
NW half	2.58	2.66	2.83	1.37	1.78	1.90	29	8.31	8.52	0.09
\pm	0.09	0.09	0.12	0.36	0.45	0.33				
SE half	2.98	3.06	3.23	2.49	2.93	2.97	70	8.41	8.51	0.10
\pm	0.06	0.07	0.09	0.36	0.45	0.33				

Atomic gas masses (M_{HI}), 1.4 GHz continuum emission, dust reddening $E(B-V)$, equivalent width of H α , metallicities determined from the Dopita et al. (2016, D16) and Pettini & Pagel (2004, O3N2) methods, and H α based star formation rates. The H α properties and 1.4 GHz continuum emission are given in three columns, corresponding to different resolutions, indicated in arcsec.

Table 4.3: Properties of the host galaxy of GRB111005A determined from HI cubes at two resolutions, 14.85" and 6.55", using tilted ring modelling.

Res.	RA (hh:mm:ss)	Dec (dd:mm:ss)	incl. ($^{\circ}$)	$V_{\text{rot,max}}$ (km s $^{-1}$)	D_{HI} (arcsec)	D_{HI} (kpc)	flux $_{\text{tot}}$ (Jy km s $^{-1}$)	$M_{\text{HI,mod}}$ ($10^9 M_{\odot}$)	$M_{\text{HI,mod}} / M_{\text{HI}}$
14.85"	14:53:07.92	-19:44:14.08	85	125	179	48.4	6.36	4.7	0.83 \pm 0.03
6.55"	14:53:07.98	-19:44:14.75	83	129	159	43.0	5.48	4.0	0.70 \pm 0.03

The coordinates of the galaxy centre (RA, Dec), inclination of the galaxy with respect to the line-of-sight (incl.), maximum rotational velocity ($V_{\text{rot,max}}$), diameter of the HI disc at a surface density of 1 M_{\odot} pc $^{-2}$ (D_{HI}), total HI line flux density (flux $_{\text{tot}}$), atomic gas mass in the model ($M_{\text{HI,mod}}$), and ratio between $M_{\text{HI,mod}}$ and the HI mass derived directly from the GMRT data (M_{HI} , see Table 4.1).

atomic gas, radio continuum distribution, and rotational patterns with only small deviations from this regularity. This is different from the irregular ISM distributions seen in the hosts of long GRBs and type Ic SN, which may suggest that the progenitor of GRB 111005A is different from the explosion of a very massive star, consistent with the fact that no SN was found to be associated with the GRB.

Subtle irregularities include a warped S-shape in the UV image, asymmetry in the HI and radio continuum distribution, a low-metallicity region close to the GRB position, and a region with very high $H\alpha$ EW. This suggests weak interaction with inflowing gas or tidal forces with another galaxy. We note that these irregularities are weak and the significance of most of them is around 2σ , so deeper observations are needed to investigate this topic. However, these irregularities were found in independent datasets, so their combined significance is higher.

Two other galaxies are present within 300 kpc and they can be responsible for the S-shape of the GRB 111005A host. Additionally there is a group of galaxies 1.37 Mpc away, whose intergalactic medium may fuel frequent gas inflows into the GRB host.

4.8 PhD candidate contribution

In this publication, I was responsible for calculating all required parameters for the analysis, performing atomic and molecular gas calculations, radio continuum and physical properties calculations, large-scale environment calculations, calculations required to plot results in fig. 4.2, 4.3, 4.6, 4.8 and all tables, and preparing the text of this publication, after discussions with other co-authors.

Appendix

A. Color-scale maps

Below we present color-scale images of the moment 0 and continuum maps.

B. Positions of regions

Below we show the positions of regions analysed in CO in Michałowski et al. (2018b).

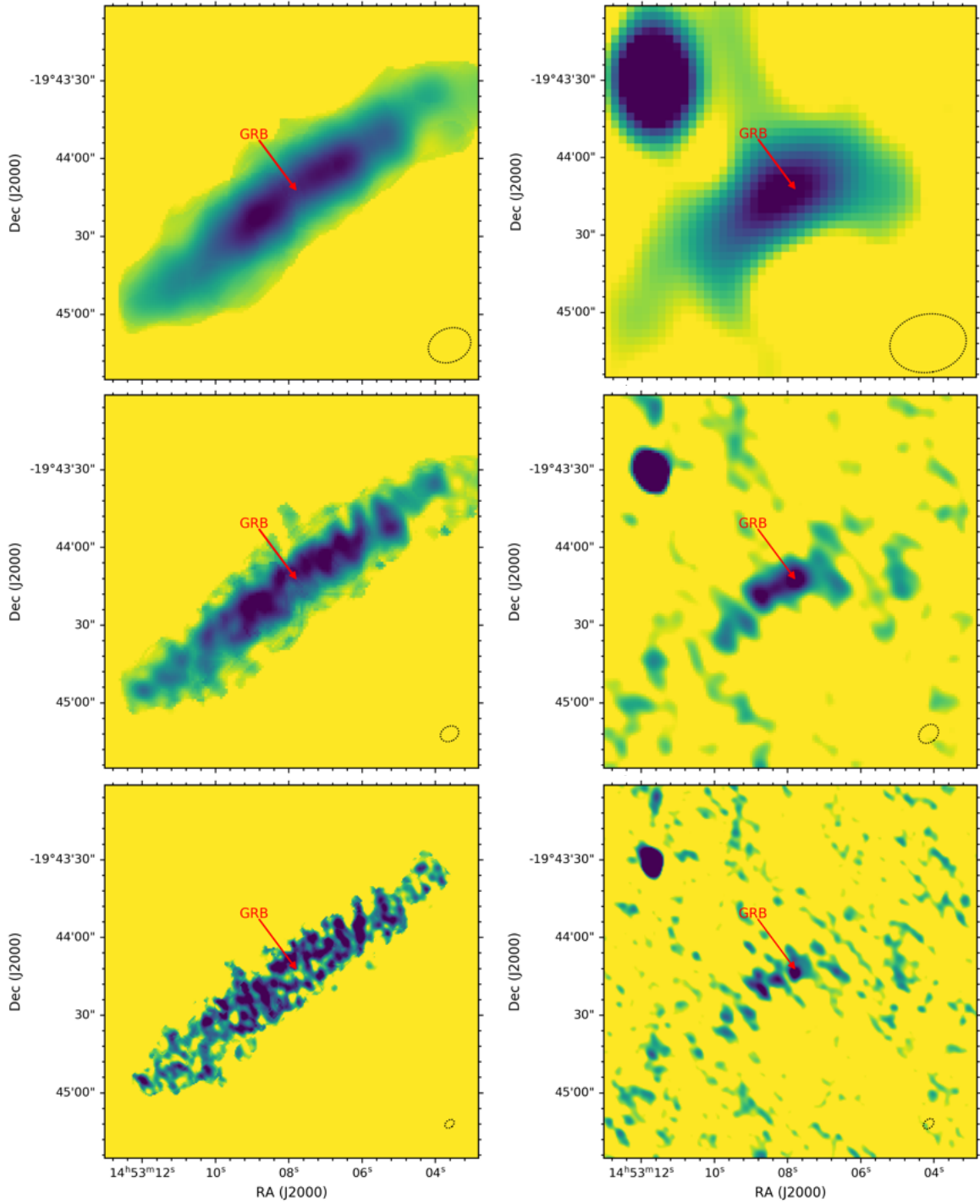


Figure 4.9: (Left) Color-scale images of moment 0 maps of the GRB 111005A host detected by GMRT with three different resolutions from top to bottom: $16.8'' \times 12.9''$, $7.4'' \times 5.7''$, and $4.0'' \times 2.8''$ (the beams are shown as grey dotted ellipses). (Right) Color-scale images of 1.4 GHz continuum emission of the GRB 111005A host at three different resolutions: $29.7'' \times 22.5''$ (top), $8.4'' \times 6.5''$ (middle), and $4.7'' \times 3.2''$ (bottom; the beams are shown as grey dotted ellipses).

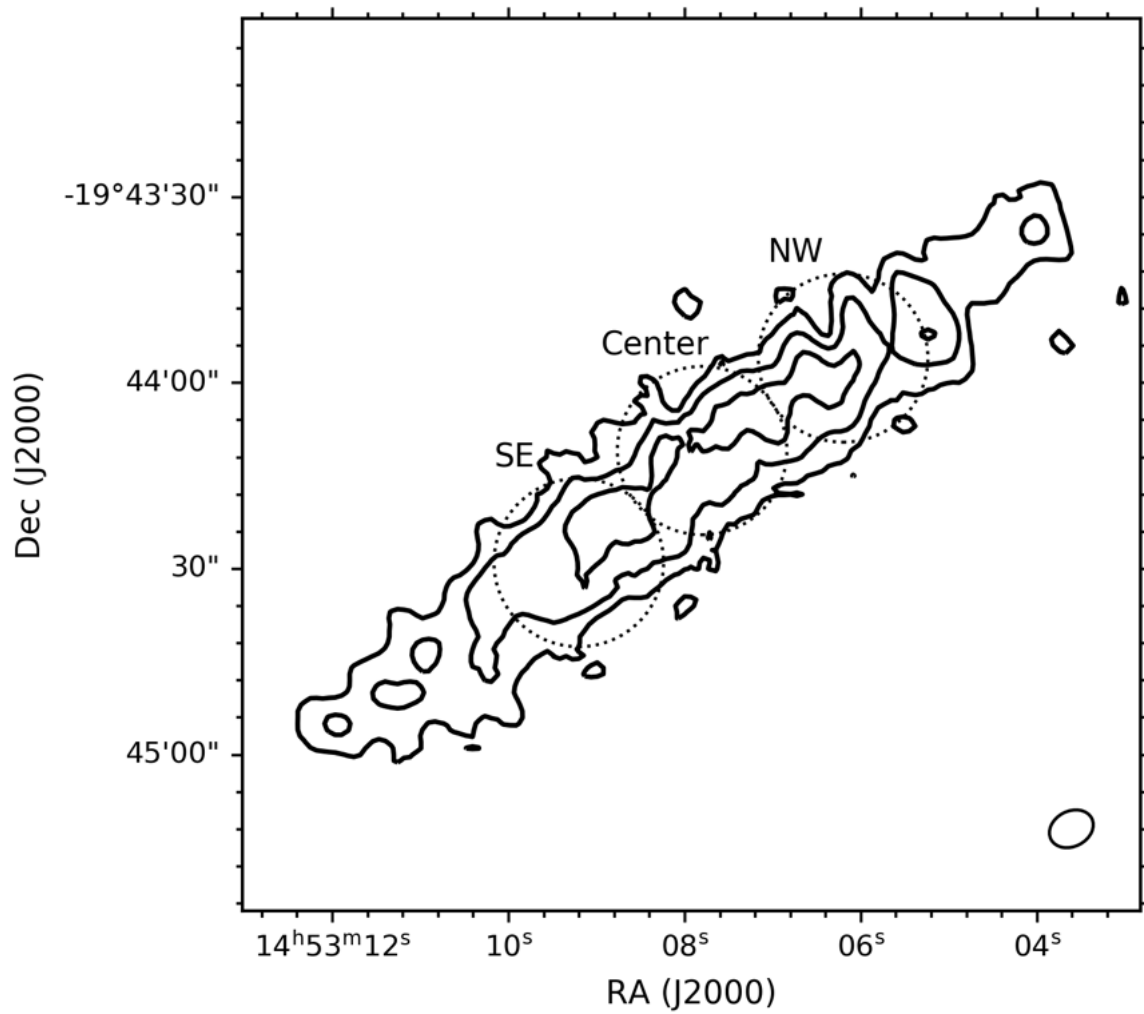


Figure 4.10: Positions of regions analysed in CO in Michałowski et al. (2018b, dotted circles) on our HI contours with a resolution of $7.4'' \times 5.7''$. The radii are $13.6''$, corresponding to the beam size of the CO observations. These apertures were used to calculate the properties shown in Table 4.1.

Chapter 5

Summary and conclusion

5.1 Dust production scenarios in galaxies at $z \sim 6-8.3$

An analysis of dust production scenarios in nine galaxies in the early Universe at redshift $\sim 6-8.3$ has been presented in Chapter 2. This redshift range corresponds to 900–600 Myr after the Big Bang. This work aimed at describing the mechanism responsible for the observed dust amount in these galaxies.

The analysis was performed on the latest dust mass constraints obtained by ALMA; HATLAS (Zavala et al. 2018), HIMIKO (Carniani et al. 2018; Ouchi et al. 2009), CR7 Clump A (Matthee et al. 2017), CR7 Clump C-2 (Matthee et al. 2017), SPT0311-58E (Marrone et al. 2018), SPT0311-58W (Marrone et al. 2018), SXDF (Inoue et al. 2016), J1342+0928 (Venemans et al. 2017), MACS0416_Y1 (Tamura et al. 2019), and A2733_YD4 (Laporte et al. 2017). A similar methodology was used to determine the dust yield as in Michałowski et al. (2010c); Michałowski (2015) and consisted of calculating the number of stars capable of producing dust based on their observed stellar mass. Due to the lack of all the necessary parameters, we performed our own dust mass and dynamical mass calculations for several galaxies. Based on the above-mentioned parameters, the dust yield was calculated as observed dust mass divided by the number of dust-producing stars in the galaxy.

The dust yield for AGB stars and SNe in nine early Universe galaxies has been obtained. Based on these calculations it is possible to conclude that AGB stars would require effectiveness exceeding theoretical predictions. Consequently, these stars were not responsible for producing the observed amount of dust. We might consider SNe as dust producers, but their production efficiency would have to approach maximum levels. This indicates either that in the early Universe, SNe must have been very efficient in producing dust or that some non-stellar mechanism took place, e.g. grain growth in the ISM.

In their multi-object spectroscopic studies with the *JWST* NIRSpec, Witstok et al. (2023) reported the presence of carbonaceous grains, based on 2175 absorption feature, in a galaxy at $z = 6.71$. This grain presence indicates some rapid formation of dust grains, as the Universe was only a billion years old at that point, and the authors

indicated evolved stars (Wolf–Rayet stars or SNe) as dust producers. The advent of observations carried out with *JWST* marked the establishment of a new observational frontier of faint galaxies up to $z < 16$ (e.g. Austin et al. 2023; Bouwens et al. 2023). Analyses of several recent observations have unveiled galaxy candidates at redshifts exceeding 10. These candidates exhibit minimal dust content, with remarkably low levels of dust attenuation (e.g. Castellano et al. 2022; Finkelstein et al. 2022). Studying the dust present in these galaxies, as well as investigating the potential stellar or non-stellar origins of the grains, will enhance our understanding of the evolution of this ISM component.

5.2 The fate of the interstellar medium in early-type galaxies. II. Observational evidence for morphological quenching

Chapter 3 presents studies on 2050 dusty elliptical galaxies. These galaxies were observed by the ESA *Herschel Space Observatory*, (Pilbratt et al. 2010)) as a part of one of the major cosmological and galaxy evolution observation projects, Galaxy And Mass Assembly (GAMA; Driver et al. 2011, 2016; Baldry et al. 2018; Smith et al. 2011¹).

Dusty early-type galaxies were selected from among 120,000 galaxies archived by the GAMA project. The final sample of 2050 galaxies has been divided into two groups based on their SFR and redshift applying the Speagle et al. (2014) redshift-dependent Main Sequence. Any galaxy with SFR 0.2dex below the MS at a given redshift is assigned to be called a below-MS galaxy. The implementation of this distinction resulted in 722 MS ETGs and 1,328 below-MS galaxies.

One of the main results is the dust removal timescale estimation of 2.26 ± 0.18 Gyr obtained by fitting an exponential function, as in Michałowski et al. (2019a), to the dust-to-stellar mass ration vs. luminosity-weighted stellar age plane. We can state that dust decline visible in the GAMA data must have an internal nature due to no dependencies on the galaxy environment. Dust removal is not dependent on the stellar mass of a galaxy, because the rate is the same for less and more massive galaxies. Also, the redshift at which the studied galaxies are located does not affect the previously mentioned quantity, because the rate remains the same with increasing redshift. Moreover, the departure of below-MS dusty ETGs from the da Cunha et al. (2010) relation was observed for the first time. In their work, Martig et al. (2009) presented morphological quenching, a mechanism that would be responsible for ceasing star formation processes. This process results in ETGs becoming red, even in the absence of cold gas removal. The transition from a rotating stellar disk to a pressure-dominated spheroid assures the stability of the gas against star formation.

Michałowski et al. (2024) studied 13 *Herschel*-detected ETGs with new CO and HI data. ISM components (dust and gas) decreased at similar rates. The timescale

¹<http://www.gama-survey.org>

of gas removal from these galaxies is slower than the decline in star formation rates. This shows that the efficiency of the new star formation process is not sufficient. It implies that the quenching of these galaxies is not solely due to gas depletion, but rather indicates a stabilization mechanism preventing the formation of new stars, for example, morphological quenching, turbulence, or magnetic fields. Many mechanisms were dismissed as primary ISM removers (such as outflows, astration, a reduction in the number of AGBs, environmental influence, mergers, and more). Ionisation from evolved low-mass stars, ionisation/outflows caused by SNIa, or AGNs might impact the ISM removal.

5.3 The interstellar medium in the environment of the supernova-less long-duration GRB 111005A

An environmental study of long GRB 111005A host galaxy with new HI line and archival MUSE data has been presented in Chapter 4. Detected by Barthelmy et al. (2011) with a burst duration of 26 ± 7 s, GRB 111005A was assigned as a long GRB. Based on previous studies on the GRB afterglow by Michałowski et al. (2018c) we know that this object has an atypical radio lightcurve with a month-lasting plateau phase and a very rapid decay after and no SN was found to be associated with the GRB. It was the first time when such a nature was observed. Hence further research on this object seemed promising.

To analyse the ISM in the host galaxy we used HI line data obtained by the Giant Metrewave Radio Telescope (GMRT)² and already published optical data obtained by the ESO Very Large Telescope (Tanga et al. 2018), equipped with the Multi-Unit Spectroscopic Explorer (MUSE; Bacon et al. 2010). The host galaxy of GRB 111005A is characterised by many regular features: symmetrical atomic gas and radio continuum distribution on a galactic scale, and both HI H α lines have symmetrical rotational patterns. Based on this symmetry we can conclude that there is no evidence of recent and strong gas inflow or outflow or any other environmental interactions. This observational fact alone distinguishes our object from other GRBs, whose hosts have irregular distributions of their ISM. Smaller regions showing weak irregularities in the distribution of matter are distinguishable and may suggest some weak interaction or inflow: an asymmetry in the HI spectrum profile with more atomic gas in the SE part of the host galaxy, 2σ asymmetry in the 1.4 GHz continuum, and a region close to the GRB position with low-metallicity. Another interesting feature is the previously undescribed S-shape clear on the UV image.

Based on the above descriptions of the ISM in the host galaxy we state that the studied long GRB must have a different progenitor than the explosion of a massive star, e.g. compact object merger.

In 2021, a long GRB has been observed and persisted for about 51 seconds. The investigation of GRB 211211A by Rastinejad et al. (2022) involved multi-wavelength analysis. Spectroscopic observations carried out with the Nordic Optical Telescope

²Project no. 30_035, PI: M. Michałowski

revealed no evidence of a SN emission to deep limits (a SN would be expected to be roughly 200 times brighter than limits). Consequently, the conventional model positing the explosion of a massive star as the progenitor of this GRB has been ruled out. The K -band luminosity 4.1 days after the burst and light curve fading closely resembled that of AT2017gfo, a well-known prominent kilonova linked with the gravitational wave event GW170817 (Abbott et al. 2017). Another instance demonstrating the association between a long GRB and a compact object merger is GRB 230307A which characteristics resemble GRB 211211A. Levan et al. (2024) examined spectroscopic data obtained from the *JWST* and dismissed the possibility of a SN. These events confirm our earlier conjectures regarding the correlation between compact mergers and long GRBs lacking supernovae signatures.

Bibliography

- Abbott, B. P., Abbott, R., Abbott, T. D., et al. 2017, *ApJL*, 848, L12
- Abdo, A. A., Ackermann, M., Ajello, M., et al. 2010, *ApJ*, 710, 133
- Agius, N. K., di Serego Alighieri, S., Viaene, S., et al. 2015, *MNRAS*, 451, 3815
- Agius, N. K., Sansom, A. E., Popescu, C. C., et al. 2013, *MNRAS*, 431, 1929
- Allamandola, L. J., Hudgins, D. M., & Sandford, S. A. 1999, *ApJL*, 511, L115
- Allamandola, L. J., Tielens, A. G. G. M., & Barker, J. R. 1985, *ApJL*, 290, L25
- Ann, H. B. & Park, J.-C. 2006, *New Astronomy*, 11, 293
- Aoyama, S., Hou, K.-C., Hirashita, H., Nagamine, K., & Shimizu, I. 2018, *MNRAS*, 478, 4905
- Arabsalmani, M., Roychowdhury, S., Starckenburg, T. K., et al. 2019, *MNRAS*, 485, 5411
- Arabsalmani, M., Roychowdhury, S., Zwaan, M. A., Kanekar, N., & Michałowski, M. J. 2015, *MNRAS*, 454, L51
- Asano, R. S., Takeuchi, T. T., Hirashita, H., & Inoue, A. K. 2013, *Earth, Planets, and Space*, 65, 213
- Austin, D., Adams, N., Conselice, C. J., et al. 2023, *ApJL*, 952, L7
- Bañados, E., Venemans, B. P., Mazzucchelli, C., et al. 2018, *Nature*, 553, 473
- Bacon, R., Accardo, M., Adjali, L., et al. 2010, in *Society of Photo-Optical Instrumentation Engineers (SPIE) Conference Series*, Vol. 7735, *Ground-based and Airborne Instrumentation for Astronomy III*, 773508
- Baldry, I. K., Liske, J., Brown, M. J. I., et al. 2018, *MNRAS*, 474, 3875
- Baldwin, J. A., Phillips, M. M., & Terlevich, R. 1981, *Publications of the Astronomical Society of the Pacific*, 93, 5
- Balogh, M. L., Morris, S. L., Yee, H. K. C., Carlberg, R. G., & Ellingson, E. 1999, *ApJ*, 527, 54
- Barlow, M. J. 1978, *MNRAS*, 183, 367

- Barthelmy, S. D., Barbier, L. M., Cummings, J. R., et al. 2005, *Space Sci. Rev.*, 120, 143
- Barthelmy, S. D., Baumgartner, W. H., Cummings, J. R., et al. 2011, *GRB Coordinates Network*, 12415, 1
- Baugh, C. M., Lacey, C. G., Frenk, C. S., et al. 2005, *MNRAS*, 356, 1191
- Bell, E. F. 2003, *ApJ*, 586, 794
- Berger, E. 2014, *Annual Review of Astronomy and Astrophysics*, 52, 43
- Bevan, A. & Barlow, M. J. 2016, *MNRAS*, 456, 1269
- Bevan, A., Barlow, M. J., & Milisavljevic, D. 2017, *MNRAS*, 465, 4044
- Bianchi, S. & Ferrara, A. 2005, *MNRAS*, 358, 379
- Bianchi, S. & Schneider, R. 2007, *MNRAS*, 378, 973
- Biscaro, C. & Cherchneff, I. 2014, *A&A*, 564, A25
- Blain, A. W., Smail, I., Ivison, R. J., Kneib, J. P., & Frayer, D. T. 2002, *Physics Reports*, 369, 111
- Blanchard, P. K., Berger, E., & Fong, W.-f. 2016, *ApJ*, 817, 144
- Blázquez-Sesé, D., Gómez-Guijarro, C., Magdis, G. E., et al. 2023, *A&A*, 674, A166
- Blanton, M. R. & Roweis, S. 2007, *AJ*, 133, 734
- Bluck, A. F. L., Maiolino, R., Brownson, S., et al. 2022, *A&A*, 659, A160
- Bluck, A. F. L., Maiolino, R., Piotrowska, J. M., et al. 2020a, *MNRAS*, 499, 230
- Bluck, A. F. L., Maiolino, R., Sánchez, S. F., et al. 2020b, *MNRAS*, 492, 96
- Bluck, A. F. L., Piotrowska, J. M., & Maiolino, R. 2023, *ApJ*, 944, 108
- Bocchio, M., Jones, A. P., & Slavin, J. D. 2014, *A&A*, 570, A32
- Bocchio, M., Micelotta, E. R., Gautier, A. L., & Jones, A. P. 2012, *A&A*, 545, A124
- Bolatto, A. D., Wolfire, M., & Leroy, A. K. 2013, *Annual Review of Astronomy and Astrophysics*, 51, 207
- Boogert, A. C. A., Gerakines, P. A., & Whittet, D. C. B. 2015, *Annual Review of Astronomy and Astrophysics*, 53, 541
- Bourne, N., Dunne, L., Maddox, S. J., et al. 2016, *MNRAS*, 462, 1714
- Bouwens, R. J., Stefanon, M., Brammer, G., et al. 2023, *MNRAS*, 523, 1036
- Bowen, G. H. & Willson, L. A. 1991, *ApJL*, 375, L53

- Brough, S., Croom, S., Sharp, R., et al. 2013, MNRAS, 435, 2903
- Calzetti, D., Kinney, A. L., & Storchi-Bergmann, T. 1994, ApJ, 429, 582
- Cardiel, N., Gorgas, J., Cenarro, J., & Gonzalez, J. J. 1998, A&AS, 127, 597
- Carilli, C. L. & Walter, F. 2013, Annual Review of Astronomy and Astrophysics, 51, 105
- Carniani, S., Maiolino, R., Smit, R., & Amorín, R. 2018, ApJL, 854, L7
- Caselli, P. & Ceccarelli, C. 2012, A&A Rev., 20, 56
- Castellano, M., Fontana, A., Treu, T., et al. 2022, ApJL, 938, L15
- Castro Cerón, J. M., Michałowski, M. J., Hjorth, J., et al. 2010, ApJ, 721, 1919
- Castro Cerón, J. M., Michałowski, M. J., Hjorth, J., et al. 2006, ApJL, 653, L85
- Cazaux, S. & Tielens, A. G. G. M. 2002, ApJL, 575, L29
- Chabrier, G. 2003a, Publications of the Astronomical Society of the Pacific, 115, 763
- Chabrier, G. 2003b, ApJL, 586, L133
- Chawner, H., Marsh, K., Matsuura, M., et al. 2019, MNRAS, 483, 70
- Chen, T. W., Brennan, S. J., Wesson, R., et al. 2021, arXiv e-prints, arXiv:2109.07942
- Cherchneff, I. 2010, in Astronomical Society of the Pacific Conference Series, Vol. 425, Hot and Cool: Bridging Gaps in Massive Star Evolution, ed. C. Leitherer, P. D. Bennett, P. W. Morris, & J. T. Van Loon, 237
- Cherchneff, I. 2011, in EAS Publications Series, Vol. 46, EAS Publications Series, ed. C. Joblin & A. G. G. M. Tielens, 177–189
- Cherchneff, I., Barker, J. R., & Tielens, A. G. G. M. 1991, ApJ, 377, 541
- Cherchneff, I. & Dwek, E. 2009, ApJ, 703, 642
- Cherchneff, I. & Dwek, E. 2010, ApJ, 713, 1
- Christensen, L., Hjorth, J., & Gorosabel, J. 2004, A&A, 425, 913
- Chung, A., van Gorkom, J. H., Kenney, J. D. P., Crowl, H., & Vollmer, B. 2009, AJ, 138, 1741
- Condon, J. J. 1992, Annual Review of Astronomy and Astrophysics, 30, 575
- Conroy, C., van Dokkum, P. G., & Kravtsov, A. 2015, ApJ, 803, 77
- Crook, A. C., Huchra, J. P., Martimbeau, N., et al. 2007, ApJ, 655, 790
- Croton, D. J., Stevens, A. R. H., Tonini, C., et al. 2016, ApJS, 222, 22

- Currie, M. J., Berry, D. S., Jenness, T., et al. 2014, in *Astronomical Society of the Pacific Conference Series*, Vol. 485, *Astronomical Data Analysis Software and Systems XXIII*, ed. N. Manset & P. Forshay, 391
- da Cunha, E., Charlot, S., & Elbaz, D. 2008, *MNRAS*, 388, 1595
- da Cunha, E., Eminian, C., Charlot, S., & Blaizot, J. 2010, *MNRAS*, 403, 1894
- Dado, S. & Dar, A. 2018, *ApJ*, 855, 88
- Dariusz, A., Dib, S., Hony, S., et al. 2016, *MNRAS*, 456, 2221
- Dartois, E., Muñoz Caro, G. M., Deboffle, D., & d'Hendecourt, L. 2004, *A&A*, 423, L33
- de Albernaz Ferreira, L. & Ferrari, F. 2018, *MNRAS*, 473, 2701
- De Looze, I., Barlow, M. J., Swinyard, B. M., et al. 2017, *MNRAS*, 465, 3309
- de Vaucouleurs, G. 1959, *Handbuch der Physik*, 53, 275
- De Vis, P., Jones, A., Viaene, S., et al. 2019, *A&A*, 623, A5
- Della Valle, M., Chincarini, G., Panagia, N., et al. 2006, *Nature*, 444, 1050
- Dell'Agli, F., Tosi, S., Kamath, D., et al. 2023, *MNRAS*, 526, 5386
- Devereux, N. A. & Young, J. S. 1990, *ApJ*, 359, 42
- Dezalay, J. P., Barat, C., Talon, R., et al. 1992, in *American Institute of Physics Conference Series*, Vol. 265, *American Institute of Physics Conference Series*, ed. W. S. Paciesas & G. J. Fishman, 304
- di Serego Alighieri, S., Bianchi, S., Pappalardo, C., et al. 2013, *A&A*, 552, A8
- Díaz-Giménez, E., Mamon, G. A., Pacheco, M., Mendes de Oliveira, C., & Alonso, M. V. 2012, *MNRAS*, 426, 296
- Dopita, M. A., Kewley, L. J., Sutherland, R. S., & Nicholls, D. C. 2016, *Ap&SS*, 361, 61
- Draine, B. T. 2009, in *Astronomical Society of the Pacific Conference Series*, Vol. 414, *Cosmic Dust - Near and Far*, ed. T. Henning, E. Grün, & J. Steinacker, 453
- Draine, B. T. 2011, *Physics of the Interstellar and Intergalactic Medium*
- Draine, B. T. & Anderson, N. 1985, *ApJ*, 292, 494
- Draine, B. T. & Lee, H. M. 1984, *ApJ*, 285, 89
- Draine, B. T. & Salpeter, E. E. 1979, *ApJ*, 231, 438
- Driver, S. P., Hill, D. T., Kelvin, L. S., et al. 2011, *MNRAS*, 413, 971

- Driver, S. P., Wright, A. H., Andrews, S. K., et al. 2016, MNRAS, 455, 3911
- Duley, W. W. & Williams, D. A. 1981, MNRAS, 196, 269
- Dwek, E. 1998, ApJ, 501, 643
- Dwek, E. & Cherchneff, I. 2011, ApJ, 727, 63
- Dwek, E., Galliano, F., & Jones, A. P. 2007, ApJ, 662, 927
- Dwek, E. & Scalo, J. M. 1980, ApJ, 239, 193
- Eales, S., Dunne, L., Clements, D., et al. 2010, Publications of the Astronomical Society of the Pacific, 122, 499
- Elliott, J., Krühler, T., Greiner, J., et al. 2013, A&A, 556, A23
- Elvis, M., Marengo, M., & Karovska, M. 2002, ApJL, 567, L107
- Fabian, A. C. 2012, Annual Review of Astronomy and Astrophysics, 50, 455
- Fernandes, R. C., Leão, J. R. S., & Lacerda, R. R. 2003, MNRAS, 340, 29
- Ferrara, A. & Peroux, C. 2021, MNRAS, 503, 4537
- Ferrara, A., Viti, S., & Ceccarelli, C. 2016, MNRAS, 463, L112
- Ferrarotti, A. S. & Gail, H.-P. 2006, A&A, 447, 553
- Finkelstein, S. L., Bagley, M. B., Arrabal Haro, P., et al. 2022, ApJL, 940, L55
- Fixsen, D. J. 2009, ApJ, 707, 916
- Fong, W. & Berger, E. 2013, ApJ, 776, 18
- Fong, W., Berger, E., Chornock, R., et al. 2013, ApJ, 769, 56
- Franco, J. & Cox, D. P. 1986, Publications of the Astronomical Society of the Pacific, 98, 1076
- Fruchter, A. S., Levan, A. J., Strolger, L., et al. 2006, Nature, 441, 463
- Fumagalli, M., Krumholz, M. R., Prochaska, J. X., Gavazzi, G., & Boselli, A. 2009, ApJ, 697, 1811
- Fynbo, J. P. U., Watson, D., Thone, C. C., et al. 2006, Nature, 444, 1047
- Fynbo, J. U., Jensen, B. L., Gorosabel, J., et al. 2001, A&A, 369, 373
- Gail, H. P. 2010, in Lecture Notes in Physics, Berlin Springer Verlag, ed. T. Henning, Vol. 815, 61–141
- Gal-Yam, A. 2019, Annual Review of Astronomy and Astrophysics, 57, 305
- Gal-Yam, A., Fox, D. B., Price, P. A., et al. 2006, Nature, 444, 1053

- Galama, T. J., Vreeswijk, P. M., van Paradijs, J., et al. 1998, *Nature*, 395, 670
- Gall, C., Andersen, A. C., & Hjorth, J. 2011a, *A&A*, 528, A13
- Gall, C., Andersen, A. C., & Hjorth, J. 2011b, *A&A*, 528, A14
- Gall, C. & Hjorth, J. 2018, *ApJ*, 868, 62
- Gall, C., Hjorth, J., & Andersen, A. C. 2011c, *A&A Rev.*, 19, 43
- Gall, C., Hjorth, J., Watson, D., et al. 2014, *Nature*, 511, 326
- Genzel, R., Tacconi, L. J., Combes, F., et al. 2012, *ApJ*, 746, 69
- Glover, S. C. O. & Clark, P. C. 2012, *MNRAS*, 426, 377
- Goldstein, A., Veres, P., Burns, E., et al. 2017, *ApJL*, 848, L14
- Gómez, F. A., White, S. D. M., Grand, R. J. J., et al. 2017, *MNRAS*, 465, 3446
- Gómez, F. A., White, S. D. M., Marinacci, F., et al. 2016, *MNRAS*, 456, 2779
- Gorosabel, J., Klose, S., Christensen, L., et al. 2003, *A&A*, 409, 123
- Gould, R. J. & Salpeter, E. E. 1963, *ApJ*, 138, 393
- Graham, A. W. & Driver, S. P. 2005, *Publications of the Astronomical Society of Australia*, 22, 118
- Griffin, M. J., Abergel, A., Abreu, A., et al. 2010, *A&A*, 518, L3
- Haan, S. & Braun, R. 2014, *MNRAS*, 440, L21
- Hall, J. S. 1949, *Science*, 109, 166
- Håring, N. & Rix, H.-W. 2004, *ApJL*, 604, L89
- Hashimoto, T., Perley, D. A., Ohta, K., et al. 2015, *ApJ*, 806, 250
- Hatsukade, B., Ohta, K., Hashimoto, T., et al. 2020, *ApJ*, 892, 42
- Hauser, M. G. & Dwek, E. 2001, *Annual Review of Astronomy and Astrophysics*, 39, 249
- Haydon, D. T., Kruijssen, J. M. D., Chevance, M., et al. 2020, *MNRAS*, 498, 235
- Heintz, K. E., Watson, D., Oesch, P. A., Narayanan, D., & Madden, S. C. 2021, *ApJ*, 922, 147
- Hildebrand, R. H. 1983, *Quarterly Journal of the Royal Astronomical Society*, 24, 267
- Hiltner, W. A. 1949a, *ApJ*, 109, 471
- Hiltner, W. A. 1949b, *Nature*, 163, 283

Hirashita, H. 1999, *ApJL*, 510, L99

Hirashita, H. 2000, *Publications of the Astronomical Society of Japan*, 52, 585

Hirashita, H. 2013, in *Proceedings of The Life Cycle of Dust in the Universe: Observations*, 27

Hirashita, H. 2015, *MNRAS*, 447, 2937

Hirashita, H., Burgarella, D., & Bouwens, R. J. 2017, *MNRAS*, 472, 4587

Hirashita, H., Ferrara, A., Dayal, P., & Ouchi, M. 2014, *MNRAS*, 443, 1704

Hirashita, H. & Inoue, A. K. 2019, *MNRAS*, 487, 961

Hirschi, R., Meynet, G., & Maeder, A. 2005, *A&A*, 443, 581

Hjorth, J. & Bloom, J. S. 2012, Cambridge University Press, 169

Hjorth, J., Gall, C., & Michałowski, M. J. 2014, *ApJL*, 782, L23

Hjorth, J., Møller, P., Gorosabel, J., et al. 2003, *ApJ*, 597, 699

Hjorth, J., Watson, D., Fynbo, J. P. U., et al. 2005, *Nature*, 437, 859

Hodge, J. A. & da Cunha, E. 2020, *Royal Society Open Science*, 7, 200556

Hogg, D. W., Baldry, I. K., Blanton, M. R., & Eisenstein, D. J. 2002, arXiv e-prints, astro

Hollenbach, D. & McKee, C. F. 1979, *ApJS*, 41, 555

Hoyle, F. & Wickramasinghe, N. C. 1970, *Nature*, 226, 62

Hu, W., Cortese, L., Staveley-Smith, L., et al. 2021, *MNRAS*, 507, 5580

Hubble, E. P. 1926, *ApJ*, 64, 321

Hubble, E. P. 1936, *Realm of the Nebulae*

Humason, M. L. 1936, *ApJ*, 83, 10

Humason, M. L., Mayall, N. U., & Sandage, A. R. 1956, *AJ*, 61, 97

Hunt, L. K., Palazzi, E., Michałowski, M. J., et al. 2014, *A&A*, 565, A112

Ichikawa, K., Ricci, C., Ueda, Y., et al. 2019, *ApJ*, 870, 31

Ichikawa, K., Ricci, C., Ueda, Y., et al. 2017, *ApJ*, 835, 74

Infante, L., Zheng, W., Laporte, N., et al. 2015, *ApJ*, 815, 18

Inoue, A. K. 2003, *Publications of the Astronomical Society of Japan*, 55, 901

Inoue, A. K., Tamura, Y., Matsuo, H., et al. 2016, *Science*, 352, 1559

Inoue, S., Yoshida, N., & Yajima, H. 2020, MNRAS, 498, 5960

Inserra, C. 2019, Nature Astronomy, 3, 697

Izzo, L., Thöne, C. C., Schulze, S., et al. 2017, MNRAS, 472, 4480

Jäger, C., Huisken, F., Mutschke, H., Jansa, I. L., & Henning, T. 2009, ApJ, 696, 706

Jäger, C., Mutschke, H., & Henning, T. 1998, A&A, 332, 291

Jakobsson, P., Hjorth, J., Fynbo, J. P. U., et al. 2004, ApJL, 617, L21

Japelj, J., Vergani, S. D., Salvaterra, R., et al. 2016, A&A, 590, A129

Jespersen, C. K., Severin, J. B., Steinhardt, C. L., et al. 2020, ApJL, 896, L20

Jiao, Q., Zhao, Y., Zhu, M., et al. 2017, ApJL, 840, L18

Jones, A. P. & Nuth, J. A. 2011, A&A, 530, A44

Józsa, G. I. G., Kenn, F., Klein, U., & Oosterloo, T. A. 2007, A&A, 468, 731

Kamphuis, P., Józsa, G. I. G., Oh, S. . H., et al. 2015, MNRAS, 452, 3139

Kelvin, L. S., Driver, S. P., Robotham, A. S. G., et al. 2012, MNRAS, 421, 1007

Kennicutt, Robert C., J., Edgar, B. K., & Hodge, P. W. 1989, ApJ, 337, 761

Kennicutt, R. C. & Evans, N. J. 2012, Annual Review of Astronomy and Astrophysics, 50, 531

Kenyon, J. S., Smirnov, O. M., Grobler, T. L., & Perkins, S. J. 2018, MNRAS, 478, 2399

Kewley, L. J., Brown, W. R., Geller, M. J., Kenyon, S. J., & Kurtz, M. J. 2007, AJ, 133, 882

Kim, J. H., Peirani, S., Kim, S., et al. 2014, ApJ, 789, 90

King, A. & Pounds, K. 2015, Annual Review of Astronomy and Astrophysics, 53, 115

Kippenhahn, R. & Weigert, A. 1990, Stellar Structure and Evolution, 192

Kirchschlager, F., Schmidt, F. D., Barlow, M. J., et al. 2019, MNRAS, 489, 4465

Klebesadel, R. W., Strong, I. B., & Olson, R. A. 1973, ApJL, 182, L85

Klose, S., Nicuesa Guelbenzu, A. M., Michałowski, M. J., et al. 2019, ApJ, 887, 206

Koike, C., Hasegawa, H., Asada, N., & Hattori, T. 1981, Ap&SS, 79, 77

Koike, C., Kaito, C., Yamamoto, T., et al. 1995, Icarus, 114, 203

Koike, C., Shibai, H., & Tuchiya, A. 1993, MNRAS, 264, 654

Koike, C., Tsuchiyama, A., Shibai, H., et al. 2000, *A&A*, 363, 1115

Koribalski, B. S., Wang, J., Kamphuis, P., et al. 2018, *MNRAS*, 478, 1611

Kouveliotou, C., Meegan, C. A., Fishman, G. J., et al. 1993, *ApJL*, 413, L101

Kroupa, P. 2001, *MNRAS*, 322, 231

Kroupa, P. 2002, *Science*, 295, 82

Krühler, T., Fynbo, J. P. U., Geier, S., et al. 2012, *A&A*, 546, A8

Krühler, T., Malesani, D., Fynbo, J. P. U., et al. 2015, *A&A*, 581, A125

Lakićević, M., van Loon, J. T., Meixner, M., et al. 2015, *ApJ*, 799, 50

Lange, R., Driver, S. P., Robotham, A. S. G., et al. 2015, *MNRAS*, 447, 2603

Laporte, N., Ellis, R. S., Boone, F., et al. 2017, *ApJL*, 837, L21

Laporte, N., Streblyanska, A., Kim, S., et al. 2015, *A&A*, 575, A92

Lau, R. M., Herter, T. L., Morris, M. R., Li, Z., & Adams, J. D. 2015, *Science*, 348, 413

Lawton, B., Gordon, K. D., Babler, B., et al. 2010, *ApJ*, 716, 453

Le Flocc'h, E., Duc, P. A., Mirabel, I. F., et al. 2003, *A&A*, 400, 499

Leger, A. & Puget, J. L. 1984a, *A&A*, 137, L5

Leger, A. & Puget, J. L. 1984b, *A&A*, 137, L5

Leloudas, G., Gallazzi, A., Sollerman, J., et al. 2011, *A&A*, 530, A95

Leroy, A. K., Walter, F., Brinks, E., et al. 2008, *AJ*, 136, 2782

Levan, A., Crowther, P., de Grijs, R., et al. 2016, *Space Sci. Rev.*, 202, 33

Levan, A. J., Gompertz, B. P., Salafia, O. S., et al. 2024, *Nature*, 626, 737

Levan, A. J., Lyman, J. D., Tanvir, N. R., et al. 2017, *ApJL*, 848, L28

Levesque, E. M. 2014, *Publications of the Astronomical Society of the Pacific*, 126, 1

Li, M., Li, Y., Bryan, G. L., Ostriker, E. C., & Quataert, E. 2020, *ApJ*, 898, 23

Lintott, C. J., Schawinski, K., Slosar, A., et al. 2008, *MNRAS*, 389, 1179

Lisenfeld, U. & Ferrara, A. 1998, *ApJ*, 496, 145

Lodders, K. & Fegley, B., J. 1995, *Meteoritics*, 30, 661

- Lucy, L. B., Danziger, I. J., Gouiffes, C., & Bouchet, P. 1989, in IAU Colloq. 120: Structure and Dynamics of the Interstellar Medium, ed. G. Tenorio-Tagle, M. Moles, & J. Melnick, Vol. 350, 164
- Lyman, J. D., Levan, A. J., Tanvir, N. R., et al. 2017, MNRAS, 467, 1795
- Madden, S. C., Cormier, D., Hony, S., et al. 2020, A&A, 643, A141
- Magdis, G. E., Daddi, E., Sargent, M., et al. 2012, ApJL, 758, L9
- Magdis, G. E., Gobat, R., Valentino, F., et al. 2021, A&A, 647, A33
- Magorrian, J., Tremaine, S., Richstone, D., et al. 1998, AJ, 115, 2285
- Maiolino, R., Schneider, R., Oliva, E., et al. 2004, Nature, 431, 533
- Makarov, D., Prugniel, P., Terekhova, N., Courtois, H., & Vauglin, I. 2014, A&A, 570, A13
- Marini, E., Dell’Agli, F., Kamath, D., et al. 2023, A&A, 670, A97
- Marrone, D. P., Spilker, J. S., Hayward, C. C., et al. 2018, Nature, 553, 51
- Martig, M., Bournaud, F., Teyssier, R., & Dekel, A. 2009, ApJ, 707, 250
- Mathis, J. S., Rumpl, W., & Nordsieck, K. H. 1977, ApJ, 217, 425
- Matsuura, M., De Buizer, J. M., Arendt, R. G., et al. 2019, MNRAS, 482, 1715
- Matsuura, M., Dwek, E., Meixner, M., et al. 2011, Science, 333, 1258
- Matthee, J., Sobral, D., Boone, F., et al. 2017, ApJ, 851, 145
- Matthee, J., Sobral, D., Santos, S., et al. 2015, MNRAS, 451, 400
- McKinnon, R., Torrey, P., Vogelsberger, M., Hayward, C. C., & Marinacci, F. 2017, MNRAS, 468, 1505
- McMullin, J. P., Waters, B., Schiebel, D., Young, W., & Golap, K. 2007, in Astronomical Society of the Pacific Conference Series, Vol. 376, Astronomical Data Analysis Software and Systems XVI, ed. R. A. Shaw, F. Hill, & D. J. Bell, 127
- Meegan, C. A., Fishman, G. J., Wilson, R. B., et al. 1992, Nature, 355, 143
- Mernier, F., de Plaa, J., Kaastra, J. S., et al. 2017, A&A, 603, A80
- Micelotta, E. R., Dwek, E., & Slavin, J. D. 2016, A&A, 590, A65
- Micelotta, E. R., Jones, A. P., & Tielens, A. G. G. M. 2010, A&A, 510, A37
- Micelotta, E. R., Matsuura, M., & Sarangi, A. 2018, Space Sci. Rev., 214, 53
- Michałowski, M. J. 2015, A&A, 577, A80

Michałowski, M. J. 2021, ApJL, 920, L21

Michałowski, M. J., Castro Cerón, J. M., Wardlow, J. L., et al. 2016, A&A, 595, A72

Michałowski, M. J., Gall, C., Hjorth, J., et al. 2024, ApJ, 964, 129

Michałowski, M. J., Gentile, G., Hjorth, J., et al. 2015, A&A, 582, A78

Michałowski, M. J., Gentile, G., Krühler, T., et al. 2018a, A&A, 618, A104

Michałowski, M. J., Gotkiewicz, N., Hjorth, J., & Kamphuis, P. 2020a, A&A, 638, A47

Michałowski, M. J., Hjorth, J., Castro Cerón, J. M., & Watson, D. 2008, ApJ, 672, 817

Michałowski, M. J., Hjorth, J., Gall, C., et al. 2019a, A&A, 632, A43

Michałowski, M. J., Hjorth, J., Malesani, D., et al. 2009, ApJ, 693, 347

Michałowski, M. J., Hjorth, J., & Watson, D. 2010a, A&A, 514, A67

Michałowski, M. J., Hunt, L. K., Palazzi, E., et al. 2014, A&A, 562, A70

Michałowski, M. J., Kamble, A., Hjorth, J., et al. 2012, ApJ, 755, 85

Michałowski, M. J., Kamphuis, P., Hjorth, J., et al. 2019b, A&A, 627, A106

Michałowski, M. J., Karska, A., Rizzo, J. R., et al. 2018b, A&A, 617, A143

Michałowski, M. J., Murphy, E. J., Hjorth, J., et al. 2010b, A&A, 522, A15

Michałowski, M. J., Thöne, C., de Ugarte Postigo, A., et al. 2020b, A&A, 642, A84

Michałowski, M. J., Watson, D., & Hjorth, J. 2010c, ApJ, 712, 942

Michałowski, M. J., Xu, D., Stevens, J., et al. 2018c, A&A, 616, A169

Mocanu, L. M., Crawford, T. M., Vieira, J. D., et al. 2013, ApJ, 779, 61

Modjaz, M., Kewley, L., Bloom, J. S., et al. 2011, ApJL, 731, L4

Morgan, H. L. & Edmunds, M. G. 2003, MNRAS, 343, 427

Morokuma-Matsui, K., Morokuma, T., Tominaga, N., et al. 2019, ApJL, 879, L13

Mutschke, H., Andersen, A. C., Clément, D., Henning, T., & Peiter, G. 1999, A&A, 345, 187

Nadolny, J., Bongiovanni, Á., Cepa, J., et al. 2021, A&A, 647, A89

Nadolny, J., Michałowski, M. J., Parente, M., et al. submitted

Nadolny, J., Michałowski, M. J., Rizzo, J. R., et al. 2023, ApJ, 952, 125

Nanni, A., Bressan, A., Marigo, P., & Girardi, L. 2013, MNRAS, 434, 2390

- Nanni, A., Bressan, A., Marigo, P., & Girardi, L. 2014, *MNRAS*, 438, 2328
- Novak, M., Bañados, E., Decarli, R., et al. 2019, *ApJ*, 881, 63
- Novak, M., Venemans, B. P., Walter, F., et al. 2020, *ApJ*, 904, 131
- Nozawa, T., Kozasa, T., Umeda, H., Maeda, K., & Nomoto, K. 2003, *ApJ*, 598, 785
- Nozawa, T., Maeda, K., Kozasa, T., et al. 2011, *ApJ*, 736, 45
- Offner, S. S. R., Clark, P. C., Hennebelle, P., et al. 2014, in *Protostars and Planets VI*, ed. H. Beuther, R. S. Klessen, C. P. Dullemond, & T. Henning, 53–75
- Offringa, A. R. 2010, *AOFlagger: RFI Software*
- Offringa, A. R., McKinley, B., Hurley-Walker, N., et al. 2014, *MNRAS*, 444, 606
- Oke, J. B. & Sandage, A. 1968, *ApJ*, 154, 21
- Omukai, K., Tsuribe, T., Schneider, R., & Ferrara, A. 2005, *ApJ*, 626, 627
- Ouchi, M., Ellis, R., Ono, Y., et al. 2013, *ApJ*, 778, 102
- Ouchi, M., Ono, Y., Egami, E., et al. 2009, *ApJ*, 696, 1164
- Owen, P. J. & Barlow, M. J. 2015, *ApJ*, 801, 141
- Paciesas, W. S., Meegan, C. A., Pendleton, G. N., et al. 1999, *ApJS*, 122, 465
- Palmerio, J. T., Vergani, S. D., Salvaterra, R., et al. 2019, *A&A*, 623, A26
- Papadopoulos, P. P., Thi, W. F., & Viti, S. 2002, *ApJ*, 579, 270
- Papadopoulos, P. P., Thi, W. F., & Viti, S. 2004, *MNRAS*, 351, 147
- Parente, M., Ragone-Figueroa, C., Granato, G. L., et al. 2022, *MNRAS*, 515, 2053
- Parente, M., Ragone-Figueroa, C., Granato, G. L., & Lapi, A. 2023, *MNRAS*, 521, 6105
- Pascoli, G. & Polleux, A. 2000, *A&A*, 359, 799
- Peeters, E., Spoon, H. W. W., & Tielens, A. G. G. M. 2004, *ApJ*, 613, 986
- Perley, D. A., Krühler, T., Schulze, S., et al. 2016, *ApJ*, 817, 7
- Perley, D. A., Levan, A. J., Tanvir, N. R., et al. 2013, *ApJ*, 778, 128
- Perley, D. A., Perley, R. A., Hjorth, J., et al. 2015, *ApJ*, 801, 102
- Pettini, M. & Pagel, B. E. J. 2004, *MNRAS*, 348, L59
- Phillips, T. G. & Huggins, P. J. 1981, *ApJ*, 251, 533
- Pian, E., Mazzali, P. A., Masetti, N., et al. 2006, *Nature*, 442, 1011

Pilbratt, G. L., Riedinger, J. R., Passvogel, T., et al. 2010, *A&A*, 518, L1

Piotrowska, J. M., Bluck, A. F. L., Maiolino, R., & Peng, Y. 2022, *MNRAS*, 512, 1052

Piron, F. 2016, *Comptes Rendus Physique*, 17, 617

Popping, G. & Péroux, C. 2022, *MNRAS*, 513, 1531

Posch, T., Baier, A., Mutschke, H., & Henning, T. 2007, *ApJ*, 668, 993

Prochaska, J. X., Bloom, J. S., Chen, H. W., et al. 2006, *ApJ*, 642, 989

Prochaska, J. X., Sheffer, Y., Perley, D. A., et al. 2009, *ApJL*, 691, L27

Quimby, R. M., Kulkarni, S. R., Kasliwal, M. M., et al. 2011, *Nature*, 474, 487

Rafelski, M., Gardner, J. P., Fumagalli, M., et al. 2016, *ApJ*, 825, 87

Rasmussen, J. & Ponman, T. J. 2007, *MNRAS*, 380, 1554

Rastinejad, J. C., Gompertz, B. P., Levan, A. J., et al. 2022, *Nature*, 612, 223

Reichart, D. E. & Price, P. A. 2002, *ApJ*, 565, 174

Rémy-Ruyer, A., Madden, S. C., Galliano, F., et al. 2014, *A&A*, 563, A31

Reshetnikov, V. & Combes, F. 1999, *A&AS*, 138, 101

Reshetnikov, V. P., Mosenkov, A. V., Moiseev, A. V., Kotov, S. S., & Savchenko, S. S. 2016, *MNRAS*, 461, 4233

Reynolds, T. N., Westmeier, T., Staveley-Smith, L., Chauhan, G., & Lagos, C. D. P. 2020, *MNRAS*, 493, 5089

Rho, J., Gomez, H. L., Boogert, A., et al. 2018, *MNRAS*, 479, 5101

Riechers, D. A., Bradford, C. M., Clements, D. L., et al. 2013, *Nature*, 496, 329

Rogstad, D. H., Lockhart, I. A., & Wright, M. C. H. 1974, *ApJ*, 193, 309

Röllig, M., Ossenkopf, V., Jeyakumar, S., Stutzki, J., & Sternberg, A. 2006, *A&A*, 451, 917

Rowlands, K., Dunne, L., Maddox, S., et al. 2012, *MNRAS*, 419, 2545

Roychowdhury, S., Arabsalmani, M., & Kanekar, N. 2019, *MNRAS*, 485, L93

Rubin, V. C., Ford, W. K., J., & Thonnard, N. 1980, *ApJ*, 238, 471

Ruiz-Velasco, A. E., Swan, H., Troja, E., et al. 2007, *ApJ*, 669, 1

Ryzhov, O., Michałowski, M. J., Leśniewska, A., & Nadolny, J. in prep.

Sakamoto, T., Barthelmy, S. D., Baumgartner, W. H., et al. 2011, *ApJS*, 195, 2

- Salpeter, E. E. 1955, *ApJ*, 121, 161
- Salvaterra, R., Della Valle, M., Campana, S., et al. 2009, *Nature*, 461, 1258
- Sánchez Almeida, J., Elmegreen, B. G., Muñoz-Tuñón, C., & Elmegreen, D. M. 2014a, *A&A Rev.*, 22, 71
- Sánchez Almeida, J., Elmegreen, B. G., Muñoz-Tuñón, C., et al. 2015, *ApJL*, 810, L15
- Sánchez Almeida, J., Morales-Luis, A. B., Muñoz-Tuñón, C., et al. 2014b, *ApJ*, 783, 45
- Sánchez Almeida, J., Muñoz-Tuñón, C., Elmegreen, D. M., Elmegreen, B. G., & Méndez-Abreu, J. 2013, *ApJ*, 767, 74
- Sancisi, R., Fraternali, F., Oosterloo, T., & van der Hulst, T. 2008, *A&A Rev.*, 15, 189
- Sandstrom, K. M., Leroy, A. K., Walter, F., et al. 2013, *ApJ*, 777, 5
- Sarangi, A. & Cherkneff, I. 2013, *ApJ*, 776, 107
- Sarangi, A., Dwek, E., & Arendt, R. G. 2018, *ApJ*, 859, 66
- Sarangi, A., Dwek, E., & Kazanas, D. 2019, *ApJ*, 885, 126
- Savaglio, S., Glazebrook, K., & LeBorgne, D. 2009, *ApJ*, 691, 182
- Savaglio, S., Rau, A., Greiner, J., et al. 2012, *MNRAS*, 420, 627
- Schady, P., Krühler, T., Greiner, J., et al. 2015, *A&A*, 579, A126
- Schlegel, D. J., Finkbeiner, D. P., & Davis, M. 1998, *ApJ*, 500, 525
- Schneider, B., Le Floc'h, E., Arabsalmani, M., Vergani, S. D., & Palmerio, J. T. 2022, *A&A*, 666, A14
- Schneider, R. & Maiolino, R. 2023, arXiv e-prints, arXiv:2310.00053
- Schneider, R., Valiante, R., Ventura, P., et al. 2014, *MNRAS*, 442, 1440
- Schöier, F. L. & Olofsson, H. 2001, *A&A*, 368, 969
- Schulze, S., Malesani, D., Cucchiara, A., et al. 2014, *A&A*, 566, A102
- Schulze, S., Yaron, O., Sollerman, J., et al. 2021, *ApJS*, 255, 29
- Scoville, N., Sheth, K., Aussel, H., et al. 2016, *ApJ*, 820, 83
- Semczuk, M., Łokas, E. L., D'Onghia, E., et al. 2020, *MNRAS*, 498, 3535
- Serra, P., Westmeier, T., Giese, N., et al. 2015, *MNRAS*, 448, 1922
- Sérsic, J. L. 1963, *Boletín de la Asociación Argentina de Astronomía La Plata Argentina*, 6, 41

- Sérsic, J. L. 1968, Atlas de Galaxias Australes
- Shahbandeh, M., Sarangi, A., Temim, T., et al. 2023, MNRAS, 523, 6048
- Sharp, C. M. & Wasserburg, G. J. 1995, Geochimica et Cosmochimica Acta, 59, 1633
- Shibuya, T., Kashikawa, N., Ota, K., et al. 2012, ApJ, 752, 114
- Slavin, J. D., Dwek, E., & Jones, A. P. 2015, ApJ, 803, 7
- Smith, D. J. B., Dunne, L., Maddox, S. J., et al. 2011, MNRAS, 416, 857
- Smith, M. W. L., Gomez, H. L., Eales, S. A., et al. 2012, ApJ, 748, 123
- Sobral, D., Matthee, J., Darvish, B., et al. 2015, ApJ, 808, 139
- Solomon, P. M., Rivolo, A. R., Barrett, J., & Yahil, A. 1987, ApJ, 319, 730
- Somerville, R. S., Gilmore, R. C., Primack, J. R., & Domínguez, A. 2012, MNRAS, 423, 1992
- Speagle, J. S., Steinhardt, C. L., Capak, P. L., & Silverman, J. D. 2014, ApJS, 214, 15
- Springob, C. M., Haynes, M. P., Giovanelli, R., & Kent, B. R. 2005, ApJS, 160, 149
- Stanek, K. Z., Dai, X., Prieto, J. L., et al. 2007, ApJL, 654, L21
- Stanek, K. Z., Matheson, T., Garnavich, P. M., et al. 2003, ApJL, 591, L17
- Stanway, E. R., Levan, A. J., Tanvir, N., et al. 2015, MNRAS, 446, 3911
- Starling, R. L. C., Wiersema, K., Levan, A. J., et al. 2011, MNRAS, 411, 2792
- Stasińska, G. & Leitherer, C. 1996, ApJS, 107, 661
- Strandet, M. L., Weiss, A., De Breuck, C., et al. 2017, ApJL, 842, L15
- Strateva, I., Ivezić, Ž., Knapp, G. R., et al. 2001, AJ, 122, 1861
- Strong, A. W. & Mattox, J. R. 1996, A&A, 308, L21
- Tacconi, L. J., Genzel, R., & Sternberg, A. 2020, Annual Review of Astronomy and Astrophysics, 58, 157
- Tamura, Y., Mawatari, K., Hashimoto, T., et al. 2019, ApJ, 874, 27
- Tanga, M., Krühler, T., Schady, P., et al. 2018, A&A, 615, A136
- Tanvir, N. R., Fox, D. B., Levan, A. J., et al. 2009, Nature, 461, 1254
- Taylor, E. L., Mann, R. G., Efstathiou, A. N., et al. 2005, MNRAS, 361, 1352
- Tazaki, R. & Ichikawa, K. 2020, ApJ, 892, 149
- Temim, T., Dwek, E., Arendt, R. G., et al. 2017, ApJ, 836, 129

Temim, T., Dwek, E., Tchernyshyov, K., et al. 2015, *ApJ*, 799, 158

Theureau, G., Bottinelli, L., Coudreau-Durand, N., et al. 1998, *A&AS*, 130, 333

Thöne, C. C., Christensen, L., Prochaska, J. X., et al. 2014, *MNRAS*, 441, 2034

Thöne, C. C., Fynbo, J. P. U., Östlin, G., et al. 2008, *ApJ*, 676, 1151

Thöne, C. C., Izzo, L., Flores, H., et al. 2021, *A&A*, 656, A136

Todini, P. & Ferrara, A. 2001, *MNRAS*, 325, 726

Togi, A. & Smith, J. D. T. 2016, *ApJ*, 830, 18

Triani, D. P., Sinha, M., Croton, D. J., Pacifici, C., & Dwek, E. 2020, *MNRAS*, 493, 2490

Trujillo, I., Graham, A. W., & Caon, N. 2001, *MNRAS*, 326, 869

Valentino, F., Magdis, G. E., Daddi, E., et al. 2018, *ApJ*, 869, 27

Valiante, E., Smith, M. W. L., Eales, S., et al. 2016, *MNRAS*, 462, 3146

Valiante, R., Schneider, R., Bianchi, S., & Andersen, A. C. 2009, *MNRAS*, 397, 1661

Venemans, B. P., Walter, F., Decarli, R., et al. 2017, *ApJL*, 851, L8

Ventura, P., di Criscienzo, M., Schneider, R., et al. 2012, *MNRAS*, 424, 2345

Villasenor, J. S., Lamb, D. Q., Ricker, G. R., et al. 2005, *Nature*, 437, 855

Vink, J. S. & de Koter, A. 2005, *A&A*, 442, 587

Vulcani, B., Bamford, S. P., Häußler, B., et al. 2014, *MNRAS*, 441, 1340

Wakelam, V., Bron, E., Cazaux, S., et al. 2017, *Molecular Astrophysics*, 9, 1

Walter, F., Weiss, A., & Scoville, N. 2002, *ApJL*, 580, L21

Wang, J., Kauffmann, G., Józsa, G. I. G., et al. 2013, *MNRAS*, 433, 270

Wang, J., Koribalski, B. S., Serra, P., et al. 2016, *MNRAS*, 460, 2143

Wang, Y.-Z., Huang, Y.-J., Liang, Y.-F., et al. 2017, *ApJL*, 851, L20

Watts, A. B., Catinella, B., Cortese, L., & Power, C. 2020, *MNRAS*, 492, 3672

Wesson, R., Barlow, M. J., Matsuura, M., & Ercolano, B. 2015, *MNRAS*, 446, 2089

Whitaker, K. E., Williams, C. C., Mowla, L., et al. 2021, *Nature*, 597, 485

Whittet, D. C. B. 2003, *Dust in the galactic environment*

Witstok, J., Shivaiei, I., Smit, R., et al. 2023, *Nature*, 621, 267

- Wolfire, M. G., Hollenbach, D., & McKee, C. F. 2010, *ApJ*, 716, 1191
- Woosley, S. E. & Heger, A. 2006, *ApJ*, 637, 914
- Yamamoto, T. & Hasegawa, H. 1977, *Progress of Theoretical Physics*, 58, 816
- Yue, C., Hu, Q., Zhang, F.-W., et al. 2018, *ApJL*, 853, L10
- Zanella, A., Daddi, E., Magdis, G., et al. 2018, *MNRAS*, 481, 1976
- Zavala, J. A., Montaña, A., Hughes, D. H., et al. 2018, *Nature Astronomy*, 2, 56
- Zeidler, S., Posch, T., Mutschke, H., Richter, H., & Wehrhan, O. 2011, *A&A*, 526, A68
- Zheng, W., Shu, X., Moustakas, J., et al. 2014, *ApJ*, 795, 93
- Zhukovska, S., Gail, H. P., & Tieloff, M. 2008, *A&A*, 479, 453

Co-author statements



Edinburgh, 21.03.2024

Co-author statement

I declare my contribution to the following publications

- Leśniewska & Michałowski, 2019, *Astronomy & Astrophysics*, 624, 13

"Dust production scenarios in galaxies at $z \sim 6-8.3$ "

I conceived the idea for the research and discussed the text with Aleksandra Leśniewska.

- Leśniewska et al., 2023, *Astrophysical Journal*, 953, 27

"The Fate of the Interstellar Medium in Early-type Galaxies. II. Observational Evidence for Morphological Quenching"

I conceived the idea for the research and discussed the text with Aleksandra Leśniewska.

- Leśniewska et al., 2022, *The Astrophysical Journal Supplement Series*, 259, 67

"The Interstellar Medium in the Environment of the Supernova-less Long-duration GRB 111005A"

I conceived the idea for the research, was the principal investigator of the Giant Metrewave Radio Telescope proposal, and discussed the text with Aleksandra Leśniewska.

Best regards,

Dr. hab. Michał Michałowski

ul. Słoneczna 36, 60-286 Poznań
NIP 777 00 06 350, REGON 000001293
tel. +48 61 829 27 70, fax. +48 61 829 27 72
obserwatorium.astro@amu.edu.pl

www.astro.amu.edu.pl

UNIVERSITY OF COPENHAGEN
NIELS BOHR INSTITUTE

Adam Mickiewicz University, Poznań
ul. Wieniawskiego 1
61-712 Poznań, Poland



Co-author statement

1 FEBRUARY 2024

I declare that I'm a co-author of the following publication: Aleksandra Leśniewska, Michał Jerzy Michałowski, Christa Gall, Jens Hjorth, Jakub Nadolny, Oleh Ryzhov, Martin Solar, "The Fate of the Interstellar Medium in Early-type Galaxies. II. Observational Evidence for Morphological Quenching", 2023, *ApJ*, 953, 27. My contribution in the above paper consisted of participating in the scientific discussion, reading, and reviewing of the manuscript.

DARK

JAGTVEJ 155A
2200 KØBENHAVN N.

DIR 45 35325920

meagan.kelsey@nbi.ku.dk
<https://dark.nbi.ku.dk/>

Yours sincerely,

Jens Hjorth
Professor
jens@nbi.ku.dk

UNIVERSITY OF COPENHAGEN
NIELS BOHR INSTITUTE

Adam Mickiewicz University, Poznań
ul. Wieniawskiego 1
61-712 Poznań, Poland



Co-author statement

1 FEBRUARY 2024

I declare that I'm a co-author of the following publication:

Aleksandra Leśniewska, Michał Jerzy Michałowski, Christa Gall, Jens Hjorth, Jakub Nadolny, Olek Ryzhov, Martin Solar, "*The Fate of the Interstellar Medium in Early-type Galaxies. II. Observational Evidence for Morphological Quenching*", 2023, *ApJ*, 953, 27.

My contribution in the above paper consisted of participating in the scientific discussion, reading, and reviewing of the manuscript.

Yours sincerely,

Christa Gall
Associate Professor
christa.gall@nbi.ku.dk

DARK

JAGTVEJ 155A
2200 KØBENHAVN N.

DIR 45 35325920

meagan.kelsey@nbi.ku.dk
<https://dark.nbi.ku.dk/>

Peter Kamphuis
e-mail: peterkamphuisastronomy@gmail.com

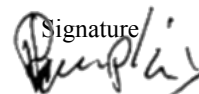
DATE
12-02-2024

Co-author statement

I declare that I'm a co-author of the following publication:

Aleksandra Leśniewska , M. J. Michałowski , P. Kamphuis, K. Dziadura, M. Baes , J. M. Castro Cerón, G. Gentile, J. Hjorth, L. K. Hunt , C. K. Jespersen, M. P. Koprowski, E. Le Floc'h, H. Miraghaei, A. Nicuesa Guelbenzu, D. Oszkiewicz, E. Palazzi, M. Polińska, J. Rasmussen, P. Schady, and D. Watson, "*The Interstellar Medium in the Environment of the Supernova-less Long-duration GRB 111005A*", 2022, The Astrophysical Journal Supplement Series, Volume 259, Issue 2, id.67, 17 pp.

My contribution in the above paper consisted of participating in the scientific discussion, reading, and reviewing of the manuscript, GMRT data reduction and describing it in the publication, writing paragraph titled: "Tilted-ring Modeling" and performing the required calculations, plotting data in Fig. 9.

Signature




ADAM MICKIEWICZ UNIVERSITY IN POZNAŃ

Faculty of Physics
Institute Astronomical Observatory

Poznań, 14 January 2024

DECLARATION

I communicate my agreement for the use of the papers listed below for the PhD thesis of Aleksandra Leśniewska. My own contribution to these articles was as follows:

Paper 1:

Leśniewska, A., Michałowski, M. J., Kamphuis, P., Dziadura, K., Baes, M., Cerón, J. C., ... & Watson, D. (2022). The Interstellar Medium in the Environment of the Supernova-less Long-duration GRB 111005A. *The Astrophysical Journal Supplement Series*, 259(2), 67.

I contributed to the execution of the research, as well as data analysis and chart creation (Fig. 1, 5, 7, 9, 10) with the use of Python. Furthermore, I have reviewed the final draft of the article.

ul. Słoneczna 36, 60-286 Poznań, Poland
NIP 777 00 06 350, REGON 000001293
tel. +48 61 829 27 70, fax. +48 61 829 27 72
obserwatorium.astro@amu.edu.pl

www.astro.amu.edu.pl

Maarten Baes
e-mail: maarten.baes@ugent.be

27 March 2024

Co-author statement

I declare that I'm a co-author of the following publication:

Aleksandra Leśniewska , M. J. Michałowski , P. Kamphuis, K. Dziadura, M. Baes , J. M. Castro Cerón, G. Gentile, J. Hjorth, L. K. Hunt, C. K. Jespersen, M. P. Koprowski, E. Le Floch, H. Miraghaei, A. Nicuesa Guelbenzu, D. Oszkiewicz, E. Palazzi, M. Polińska, J. Rasmussen, P. Schady, and D. Watson, “*The Interstellar Medium in the Environment of the Supernova-less Long-duration GRB 111005A*”, 2022, The Astrophysical Journal Supplement Series, Volume 259, Issue 2, id.67, 17 pp.

My contribution in the above paper consisted of:

- participating in writing Giant Metrewave Radio Telescope proposal,
- the scientific discussion, reading, and reviewing of the manuscript.

Signature

A handwritten signature in blue ink, consisting of several loops and a long horizontal stroke extending to the right.



Poznań, 02/04/2024

Jakub Nadolny
e-mail: jakub.nadolny@amu.edu.pl

Co-author statement

I declare that I'm a co-author of the following publication:

Aleksandra Leśniewska, Michał Jerzy Michałowski, Christa Gall, Jens Hjorth, Jakub Nadolny, Oleh Ryzhov, Martin Solar, *"The Fate of the Interstellar Medium in Early-type Galaxies. II. Observational Evidence for Morphological Quenching"*, 2023, ApJ, 953, 27.

My contribution in the above paper consisted of participating in the scientific discussion, reading, reviewing and editing of the manuscript. I was also responsible for providing the results regarding dust removal timescale using simulated early-type galaxies from Millennium Simulations (Fig. 1 middle panel).



.....
Jakub Nadolny